Targeted Nanoparticle Delivery of Therapeutics across the Blood-Brain and Blood-Tumor Barriers to Breast Cancer Brain Metastases

Thesis by

Emily Ann Wyatt

In Partial Fulfillment of the Requirements
for the Degree of
Doctor of Philosophy

CALIFORNIA INSTITUTE OF TECHNOLOGY
Pasadena, California

2018
Defended May 18, 2018

Emily Ann Wyatt
ORCID: 0000-0002-7534-0582

ACKNOWLEDGEMENTS

First, I would like to thank Dr. Mark Davis for giving me the opportunity to train in his lab. It has been a privilege to work with and learn from such a talented scientist. Beyond this, Mark has been an incredible mentor and his advising style challenged me in ways I had not been before. From him I learned how and when to stand my ground, gained confidence in my abilities as an independent researcher, and most of all developed an understanding of how to truly listen to criticism and use it to better myself. I especially appreciate the personal relationship we developed in addition to our professional one as we faced unexpected challenges in supporting our loved ones bravely battling cancer.

Several students in the Davis group have had a tremendous impact on my experience as well. Andrew Clark, a former MD/PhD graduate, laid the groundwork for this project and deserves recognition. He was an absolute pleasure to work with, an awesome officemate, and we had many insightful discussions during our time together. Dorothy Pan, another MD/PhD graduate, was also an outstanding coworker and helped me get my feet underneath me with synthesis. I'd also like to thank Viktor Cybulskis and Kramer Brand, a postdoc and former graduate student on the catalysis side of the lab, for their friendship, laughs and support over our many, many lunches together.

I would also like to thank the members of my PhD committee – Professors Mikhail Shapiro, Sarkis Mazmanian and Dave Tirrell – who served as wonderful advisors and challenged me to grow as a scientist and critical thinker.

I'd also like to acknowledge Professor Jim Swartz at Stanford University who first got me interested in research and gave me the tools to succeed both at Genentech and Caltech. Additionally, I'd like to thank my many mentors at Genentech, particularly Shelly

Pizarro, who encouraged me to return to Caltech and chase my dreams after two wonderful years working with them.

Many collaborators and members of the Caltech community have been a great help during my time training. Mona Shahgholi assisted with mass spectrometry measurements and Dave Vandervelde helped me learn several nuclear magnetic resonance techniques. Xiaowei Zhang helped establish the magnetic resonance imaging parameters while also teaching me how to interpret the brain scans. Audrey Lee-Gosselin performed the intracranial injections for my comparison of murine models, which would have been impossible to complete without her assistance. I'd also like to acknowledge Saul Priceman at City of Hope who taught me the intracardiac injection technique. Martha Hepworth, Emily Loiacano and Allison Ouellette have been great sources for administrative help and support. Suresh Gupta, a computer guru, saved me a lot of time and helped triage several computer crises.

The staff at the animal facility also deserve acknowledgement, especially Gwen Williams and Melissa McPherson who first trained me on animal handling and more advanced procedures. I'd also like to thank veterinarian and now director Dr. Karen Lencioni for her advice on caring for mice with tumors and assistance in expedited review of protocols. Erika Martinez-Carcamo, Lorena Sandoval, John Papsys and Gloria Martinez were all incredibly helpful in providing animal husbandry and a pleasure to work with.

Several members of the greater Caltech community had a tremendous impact on my personal development as well, especially the staff at the Caltech Diversity Center and Larissa Charnsangavej who helped me come to understand and gain confidence in my identity. I'd also like to thank Felicia Hunt, Kate McAnulty, Nilza Santana-Castillo and my fellow RAs for being incredible teammates in building residential community on campus.

Many friends helped encourage me during my PhD training. In particular, I’d like to thank my softball family for their friendship and support. My teammates have been a constant source of laughter, and helped take my mind off science once in a while. I’d also like to thank the many friends with whom I began this experience at Caltech, as we’ve taken turns offering words of encouragement. I’d also like to thank my dear friend Obi Onyeacholem, who has been there to support me every step of the way.

I would also like to thank my incredibly supportive better half, Cora Went, for being a constant source of encouragement during my time at Caltech. From sharing countless outdoor adventures to cooking me incredible meals in the final stretch, her unwavering love has brought me to the finish line, even as she embarked on her own PhD.

I’d also like to thank my family who has helped shape the person I have become, and has given me countless opportunities to pursue my passions. My mom who has shown me what it means to be a strong woman and my dad who has always nurtured my compassionate side have been a constant source of love. And my brother, who put up with an entirely too competitive little sister and taught me so much by finding his own path.

Finally, I’d like to dedicate this work to one person very important to me whose loss inspired my return to academia to pursue my PhD, specifically in the area of brain drug delivery. To my grandfather, Dr. Edmund John Harris, who was a source of incomparable joy and strength.

ABSTRACT

Brain metastases of human epidermal growth factor receptor 2 (HER2)-positive breast cancer are presenting an increasing problem in the clinic. While HER2-targeted therapies effectively control systemic disease, their efficacy against brain metastases is hindered by their inability to penetrate the blood-brain and blood-tumor barriers (BBB and BTB). One promising strategy to increase brain penetration of systemic therapeutics is to exploit endogenous transport systems at the BBB to shuttle drugs into the brain. Previous studies showed that gold nanoparticles designed to shed transferrin receptor (TfR)-targeting ligands under acidic conditions encountered during transcytosis of the BBB demonstrated increased accumulation in the brain. The focus of this work was to determine whether therapeutic, TfR-targeted nanoparticles using an improved acid-cleavable chemistry could be used to deliver therapeutically useful amounts of drug to the brain.

To accomplish this goal, a new animal model of HER2-positive breast cancer brain metastasis was developed in an attempt to create a clinically representative, impermeable barrier to standard therapeutics. This new model establishes brain metastases by methods that more closely resemble the human disease, forming whole-body tumors that eventually metastasize to the brain. Brain metastases formed by this new methodology show no response to standard HER2-targeted agents, mimicking the clinical situation.

Next, efficacy and brain uptake of TfR-targeted, single-agent therapeutic nanoparticles were investigated in the newly developed model, as well as two common models from the literature. These nanoparticles show significant tumor growth delay and increased accumulation in both brain metastases and healthy brain tissue in all three models, highlighting their therapeutic potential. Additionally, non-BBB-penetrant small

molecule and non-targeted nanoparticle therapeutics elicit a substantial antitumor response as well as brain tumor accumulation in the most commonly used literature model. In contrast, the new model and one gaining popularity in the literature provide for a more clinically relevant, impermeable barrier to non-BBB-penetrant agents, indicating that the method used to establish brain metastases can affect efficacy and brain uptake of therapeutics.

PUBLISHED CONTENT AND CONTRIBUTIONS

Wyatt EA, Davis ME (2018) Method of establishing breast cancer brain metastases affects brain uptake and efficacy of targeted, therapeutic nanoparticles. *Bioengineering and Translational Medicine* 1–8.

E.A.W. designed and performed research, analyzed data and wrote the manuscript.

TABLE OF CONTENTS

DETAILED TABLE OF CONTENTS

LIST OF FIGURES

Chapter II

Chapter III

LIST OF TABLES

ABBREVIATIONS

Ab. Antibody

ABC. Adenosine triphosphate-binding cassette

ACN. Acetonitrile

ADCC. Antibody-dependent cellular cytotoxicity

AMT. Adsorptive-mediated transcytosis

Apo-Tf. Iron-free form of transferrin

ATP. Adenoside triphosphate

AuNP. Gold nanoparticle

A4P0. Solution of 4% acrylamide in phosphate buffered saline

BBB. Blood-brain barrier

BM. Brain metastasis

BTB. Blood-tumor barrier

Bzl. Benzyl

CD31. Cluster of differentiation 31

CED. Convection-enhanced diffusion/delivery

CFP. Cerulean fluorescent protein

CLARITY. Clear Lipid-exchanged Acrylamide-hybridized Rigid Imaging/Immunostaining/in situ-hybridization-compatible Tissue hYdrogel

CPT. Camptothecin

CPT-gly.TFA. 20-O-Glycincamptothecin trifluoroacetic acid salt

CSF. Cerebrospinal fluid

CTLA-4. Cytotoxic T-lymphocyte–associated antigen 4

DAB. 3,3′-Diaminobenzidine tetrahydrochloride

DAPI. 4',6-diamidino-2-phenylindole

DCM. Dichloromethane

DIPEA. N,N-diisopropylethylamine

DLS. Dynamic light scattering

DMEM. Dulbecco's modified Eagle's medium

DMF. Dimethylformamide

DMSO. Dimethylsufoxide

DSC. N,N'-disuccinimidyl carbonate

EDC. 1-Ethyl-3-(3-dimethylaminopropyl)carbodiimide

EDTA. Ethylenediaminetetraacetic acid

EGFR. Epidermal growth factor receptor type 1

ER. Estrogen receptor

ESI. Electrospray ionization

EtOH. Ethanol

FBS. Fetal bovine serum

FDA. Food and Drug Administration

FUS. Focused ultrasound

GBM. Glioblastoma multiforme

Gluc. Gaussia luciferase

GPC. Gel permeation chromatography

H&E. Hematoxylin and eosin

HCl. Hydrochloric acid

HER2. Human epidermal growth factor receptor 2

Holo-Tf. Iron-saturated form of transferrin

HPLC. High-performance liquid chromatography

HMPA. *N*-(2-hydroxypropyl)methacrylamide

H_2SO_4. Sulfuric acid

IC. Intracranial

IC-CPT. Camptothecin treatment group in intracranial model

IC-Non. Non-targeted nanoparticle treatment group in intracranial model

IC-TfR. Transferrin receptor-targeted nanoparticle treatment group in intracranial model

ICD. Intracardiac

ICD-CPT. Camptothecin treatment group in intracardiac model

ICD-Non. Non-targeted nanoparticle treatment group in intracardiac model

ICD-TfR. Transferrin receptor-targeted nanoparticle treatment group in intracardiac model

ICI. Intracerebral implantation

ICV. Intracerebroventricular

Il2rg. Interleukin-2 receptor subunit gamma

InsR. Insulin receptor

IV. Intravenous

IV-CPT. Camptothecin treatment group in intravenous model

IV-Non. Non-targeted nanoparticle treatment group in intravenous model

IV-TfR. Transferrin receptor-targeted nanoparticle treatment group in intravenous model

LRP1/2. Low-density lipoprotein-receptor-related proteins 1 and 2

MALDI-TOF. Matrix assisted laser desorption ionization-time of flight

MAP. Mucic acid polymer

MAP-CPT. Mucic acid polymer conjugate of camptothecin

MAPK. Mitogen-activated protein kinase

MeOH. Methanol

MIP. Maximum intensity projection

MRI. Magnetic resonance imaging

MW. Molecular weight

MWCO. Molecular weight cut-off

NaN_3. Sodium azide

ND. Not detectable

NHS. N-hydroxysuccinimide

nitroPBA. 3-carboxy-5-nitrophenyl boronic acid

NK. Natural killer

NMR. Nuclear magnetic resonance

NOESY. Nuclear Overhauser effect spectroscopy

Non-targeted MAP-CPT nanoparticle. Nanoparticle formulation containing a mucic acid polymer conjugate of camptothecin nanoparticle core with methoxy-terminated polyethylene glycol on the particle surface

NSCLC. Non-small cell lung cancer

OMe-PEG-nitroPBA. Methoxy-terminated polyethylene glycol conjugated to 3-carboxy-5-nitrophenyl boronic acid

OX26. Anti-transferrin receptor antibody IgG2a

PB. Phosphate buffer

PBS. Phosphate buffered saline

PBST. Phosphate buffered saline with 0.2% (v/v) Tween 20

PCL. Polycaprolactone

$Pd(OH)_2$. Palladium hydroxide on carbon

PD-1. Programmed death 1 (PD-1)

PEG. Polyethylene glycol

PET. Positron emission tomography

PI3K. Phosphatidylinositol-3 kinase

PFS. Progression-free survival

PLA. Poly(lactic acid)

PLGA. Poly(lactic-co-glycolic acid)

PPD. Passive paracellular diffusion

PTD. Passive transcellular diffusion

PTFE. Polytetrafluoroethylene

Rag2. Recombination activating gene 2

RARE. Rapid acquisition enhanced relaxation

RIPA. Radioimmunoprecipitation assay

RMT. Receptor-mediated transcytosis

RPMI. Roswell Park Memorial Institute

SCP. Solute carrier protein

SD. Standard deviation

SDS. Sodium dodecyl sulfate

SE. Standard error of the mean

SEER. Surveillance, Epidemiology, and End Results program

TEA. Triethylamine

TEER. Transepithelial resistance

TEM. Transmission electron microscopy

***Tert*-Boc.** *Tert*-butyloxycarbonyl

Tf. Transferrin

TFA. Trifluoroacetic acid

Tf-PEG-nitroPBA. Transferrin protein conjugated to 3-carboxy-5-nitrophenyl boronic acid with a polyethylene glycol spacer

TfR. Transferrin receptor

TfR-targeted MAP-CPT nanoparticle. Nanoparticle formulation containing a mucic acid polymer conjugate of camptothecin nanoparticle core with transferrin on the particle surface

THF. Tetrahydrofuran

TJM. Tight junction modulation

TNBSA. 2,4,6-trinitrobenzene sulfonic acid

UV-VIS. Ultraviolet–visible

Chapter I

INTRODUCTION

1.1 Recent developments in cancer treatment: opportunities and challenges

Significant improvements in cancer care have been made over the past decade, as evidenced by declining incidence and mortality rates. Overall cancer incidence, defined as the rate of cancer diagnoses per 100,000 residents, decreased significantly, dropping a near 1% annually (1). For some cancer types, such as prostate, lung, colorectal and stomach cancers, incidence has dropped at even faster rates (Fig 1.1A). A number of factors have contributed to this decline, particularly prevention efforts (e.g. routine primary care, tobacco cessation, programs that target obesity) and advances in screening practices (1,2). Additionally, because of improvements in early detection and treatment, more Americans are surviving cancer, with about two-thirds of Americans diagnosed with cancer today living for at least 5 years (3,4). Since its peak in the early 1990s, overall cancer mortality has dropped steadily, translating into an estimated 2 million fewer deaths (2,5). For the most common cancer types – lung, breast, prostate, and colorectal – mortality rates have decreased significantly, with an annual rate of decline of 2% (Fig 1.1B).

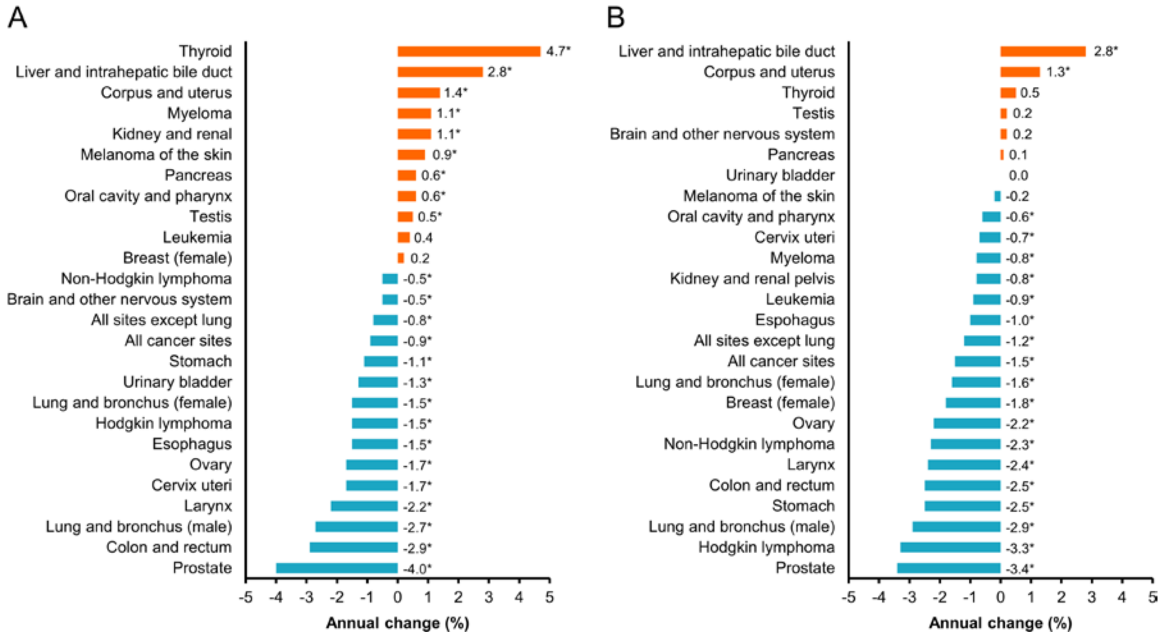

Fig. 1.1. Declining cancer incidence and mortality rates in the US. Trends in Surveillance, Epidemiology, and End Results (SEER) incidence (**A**) and cancer death rates (**B**) for common cancers, 2004 to 2013. * = $P < 0.05$. Data from (6).

Most importantly, recent advances in cancer research and treatment have led to more durable therapeutic responses and improvement in long-term survival. Perhaps the importance of continued investment in new drugs and therapeutic strategies is best illustrated by recent developments in the treatment of metastatic melanoma using immune checkpoint inhibitors. In a long-term follow-up of a phase I study of nivolumab monotherapy, a programmed death 1 (PD-1) inhibitor, in metastatic melanoma patients, more than one third of patients were alive after 5 years, a significantly higher proportion than observed previously (7). Similarly, the 3-year survival for patients in a phase I study with advanced melanoma treated with another PD-1 inhibitor, pembrolizumab, was 40% (8). Additionally, a recent phase III clinical trial showed that, for high-risk patients with metastatic melanoma, treatment with the cytotoxic T-lymphocyte–associated antigen 4 (CTLA-4) inhibitor ipilimumab led to significantly higher rates of recurrence-free survival, overall survival, and distant metastasis–free survival after 5 years than previously observed (9). The results from these as well as other recent clinical trials demonstrate the meaningful clinical benefit that can be achieved by sustained investment in cancer research, particularly the investigation of new anti-cancer therapeutic approaches.

1.1.1 Brain metastases as emerging threats to long-term survival

Brain metastases are becoming increasingly more common among cancer survivors as more effective treatments prolong survival, thus giving the cancer more time to spread to the brain. Metastatic brain tumors most commonly arise from lung, skin (melanoma) and breast cancers, but have also been observed in patients with other cancer types (10). The incidence of metastasis to the brain is highest in patients with lung cancer. Brain metastases are present in approximately 10-25% of these patients at initial diagnosis, with another 40-50% developing them over time and an even greater incidence at autopsy (11). For non-small cell lung cancer (NSCLC) patients in particular, brain metastases are extremely common and confer a generally poor prognosis (12). In patients with metastatic melanoma, autopsy reports indicate the incidence of brain metastasis may be as high as 75% (13). Similar to lung cancer patients, the prognosis for patients with brain metastases resulting from melanoma is dismal, with a median survival of approximately 4 months after diagnosis (14). For patients with breast cancer, brain metastasis incidence varies with the cancer subtype. Patients with triple-negative or human epidermal growth factor receptor 2 (HER2)-positive breast cancers have a brain metastasis incidence of approximately 20% and 25-50%, respectively (15-17). Of particular concern, for HER2-positive, metastatic breast cancer patients, the brain is increasingly the first site of progression after treatment

(18). The incidence is lower in patients with estrogen receptor (ER) positive disease (15,16).

Detection of brain metastases is critical for initial staging of patients with metastatic disease. In some cases, brain metastases are indicated by neurological symptoms. However, brain metastases are asymptomatic 60-75% of the time (19). Symptoms of brain metastases typically vary depending on their size, number and location. Persistent headache is the most common presenting symptom, but patients may also present with more serious symptoms such as seizures, cognitive decline and loss of motor and sensory function as a consequence of increased intracranial pressure (20). In symptomatic or high-risk patients with known malignancies, computed tomography (CT) or magnetic resonance imaging (MRI) modalities are typically used to detect brain metastases (21).

Current treatments for brain metastases are largely palliative, as surgery and radiation remain the cornerstones of therapy (22). For patients with only one lesion or a small number of lesions in accessible regions of the brain, surgery may be a viable option and provide initial relief of symptoms. Stereotactic radiosurgery (SRS) or whole-brain radiotherapy (WBRT) are the two most common types of radiation therapy used in brain metastasis patients. These treatment strategies have been associated with modest initial clinical improvement in most patients, but the responses are not durable (23,24). Improvements in patient survival are measured in weeks or months. Additionally, despite recent advances, such as image-based guidance for surgical resection (25), these treatment strategies have several limitations depending on the location of the brain tumor as well as significant, well-recognized adverse effects (22). Most importantly, standard chemotherapy and molecularly targeted drugs that effectively control systemic disease have demonstrated little to no efficacy against brain metastases in the clinic (26,27). Only a handful of clinical responses have been reported, and the effects are modest (28-30). Clinical data on the responsiveness of brain metastases to the combination of chemotherapy and WBRT are also disappointing (27).

Historically, the lack of durability in response was not a significant problem because most patients developed brain metastases late in the course of their disease and systemic progression was typically to blame for mortality. Thus, development of treatment strategies for brain metastases was not a priority. However, as new systemic therapies continue to extend survival for metastatic cancer patients, brain metastases are expected to become more prevalent and arise more often in other cancer types. Unless improvements are made in the treatment of these brain metastases, an increasing proportion of patients will be at risk of mortality as a result of brain progression, even at a time when their systemic disease is well-controlled.

1.1.2 Human epidermal growth factor 2 (HER2)-positive breast cancer brain metastases

Human epidermal growth factor 2 (HER2)-positive, metastatic breast cancer is a particularly compelling example where brain metastases threaten to limit the gains made with improved systemic therapies. HER2 overexpression is observed in approximately 25% of human breast cancers, and is associated with increased aggressiveness of the tumor and poor patient prognosis (31). The anti-HER2 monoclonal antibody trastuzumab was fast-tracked by the FDA and approved in 1998 as first-line therapy for the treatment of metastatic, HER2-positive cancer based on data from a pivotal trial demonstrating that the addition of trastuzumab to chemotherapy improved disease-free and overall survival (32). However, shortly after the introduction of trastuzumab, clinicians started to observe an apparent increase in the incidence of brain metastases compared to historical numbers. This observation led to a number of retrospective studies reporting incidences of approximately 25-40% (33-37). The findings from these studies are provided in Table 1.1.

Study	Patients included in analysis	# of patients with metastatic breast cancer	Incidence of BM (%)	Median survival from BM diagnosis (mo)
Bendell et al. (33)	Initiating trastuzumab between 1998–2000	122	34	13
Altaha et al. (34)	With HER2-positive breast cancer diagnosed between 1998–2003	31	48	Not reported
Clayton et al. (35)	Initiating trastuzumab between 1999–2002	93	25	5.4
Stemmler et al. (36)	Initiating trastuzumab between 1999–2002	136	31	13
Yau et al. (37)	Initiating trastuzumab between 1999–2002	87	30 (at 1 y)	4

Table 1.1. Incidence of brain metastases among patients with HER2-positive breast cancer, as documented in retrospective studies. BM, brain metastases. Adapted from (17).

Since then, considerable clinical data has accumulated on the incidence of brain metastases in HER2-positive breast cancer patients and their outcomes. Current estimates suggest that up to 50% of metastatic, HER2-positive breast cancer patients will develop brain metastases over the course of their disease, and the incidence appears to be rising (38). Though systemic disease is well-controlled with trastuzumab and other HER2-targeted therapies, brain metastases from HER2-positive breast cancer patients do not respond to therapy, and are often the reason for treatment failure (36,39). The limited efficacy of these agents is mostly attributed to their lack of penetration through the blood-brain and blood-tumor barriers (BBB and BTB), though this is fiercely debated in the literature (see sections 1.2.3 and 2.1.2). Nevertheless, one thing is clear: improvements in systemic control and overall survival with HER2-targeted therapy have unveiled a patient population in whom brain metastases are a significant source of mortality that would have otherwise remained silent.

The changing face of HER2-positive, metastatic disease has broader implications, as similar advances in systemic treatment are being made in other cancers. The combination of cancer types that have a high propensity to colonize the brain and therapeutics that are effective systemically, but that do not penetrate the brain creates the opportunity for brain metastatic cancers to become an even greater clinical challenge, limiting the gains that have been made over the past decades in controlling systemic disease. Additionally, the example of HER2-positive breast cancer brain metastasis illustrates factors common to many brain diseases, namely: (i) complex disease progression reducing the possibility of a single "silver bullet" treatment, (ii) limited to no disease-modifying treatment options currently available, and (iii) few promising candidate therapies in the pipeline. There is reason to be hopeful, however, as new strategies to increase the brain uptake of therapeutics begin to emerge.

1.2 The blood-brain and blood-tumor barriers (BBB and BTB)

1.2.1 Structure and function of the BBB

A major reason for the limited progress in treating brain diseases is the inability of most systemic therapeutics to access the brain from the blood. The delivery of drugs to the brain is impaired by the blood-brain barrier (BBB), an anatomical barrier that separates the vasculature and brain parenchyma. This highly restrictive, physiologic barrier excludes more than 98% of small-molecule drugs and nearly all large-molecule therapeutics from the brain (40). The BBB problem is illustrated in Figure 1.2, a whole body autoradiogram of a mouse sacrificed shortly after systemic administration of a radiolabeled small molecule, histamine. Despite the common misconception, most small molecules do not readily cross the BBB (see section #).

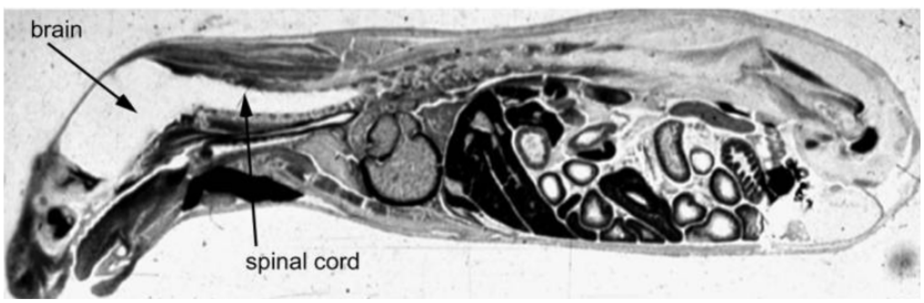

Fig. 1.2. Radiolabeled histamine accumulates in all organs of an adult mouse, except for the brain and spinal cord, following intravenous injection. Image from (40).

The BBB is formed by endothelial cells, pericytes and astrocyte end foot processes (Fig. 1.3), and plays a key role in maintaining homeostasis within the brain, with functions including: (i) control of molecular traffic (e.g. influx and efflux of waste), (ii) maintenance of optimum ion concentrations for neural signaling and (iii) control of immune surveillance (41). These diverse and finely controlled functions are largely facilitated by the presence of tight junctions between the endothelial cells, a key feature of the BBB (42). The junctions significantly reduce paracellular diffusion of polar solutes, macromolecules and cells, forcing solute transport into the brain to primarily occur across individual endothelial cells, where it can be tightly controlled. Even sodium ions with a hydrated radius of 3.6 Å cannot squeeze past them. Nearby supporting cells, particularly astrocytes, play a critical role in maintaining the tight junctions and barrier function (42).

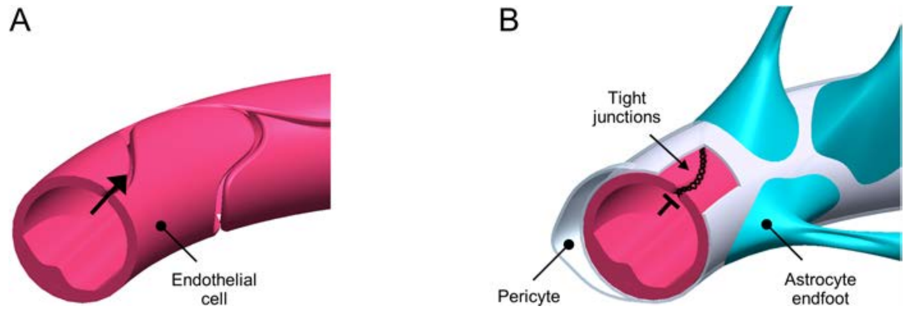

Fig. 1.3. Schematic of the BBB. Unlike those that line a general blood vessel (**A**) endothelial cells lining a brain blood vessel (**B**) form tight junctions at their margins, that are further modified by pericytes and astrocyte end feet to form the BBB.

1.2.2 Solute transport at the BBB: regulation, not isolation

Though the BBB severely limits the passage of compounds into the brain, its role is one of regulation, not isolation. Several transport systems exist at the BBB endothelium to allow the influx of necessary nutrients and their carrier proteins. There are six main transport mechanisms at the BBB, including: (i) passive paracellular diffusion (PPD), (ii) passive transcellular diffusion (PTD), (iii) solute carrier proteins (SCP), (iv) receptor-mediated transcytosis (RMT), (v) adsorptive-mediated transcytosis (AMT) and (vi) tight junction modulation (TJM) (Fig. 1.4) (42).

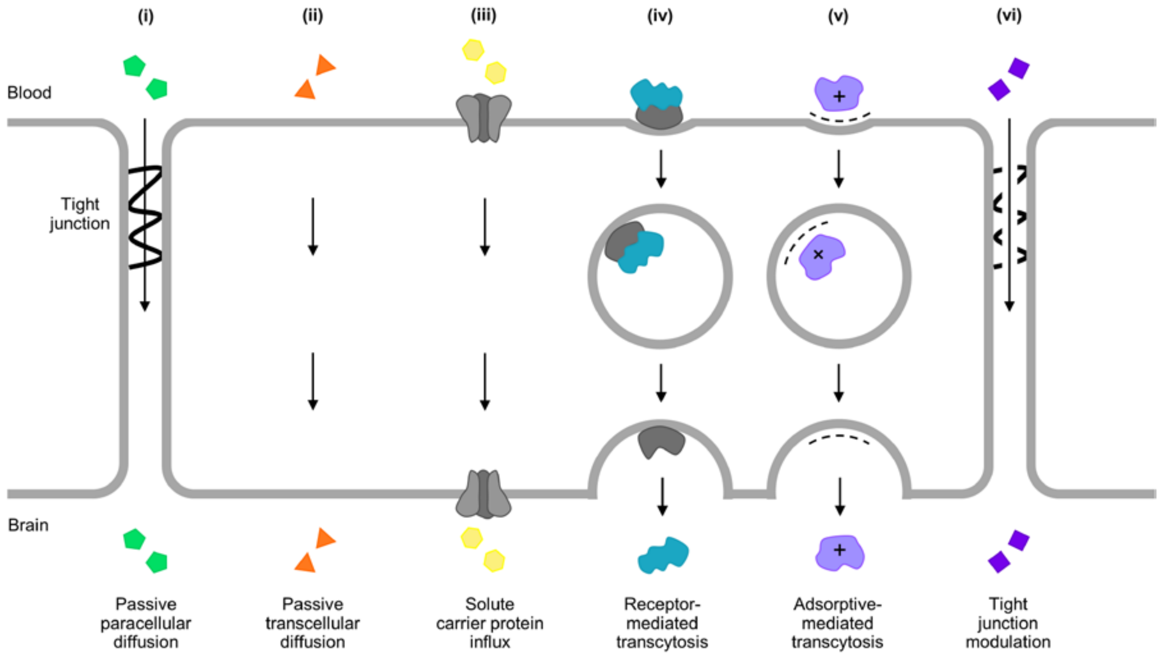

Fig. 1.4. Solute transport systems at the BBB. Solutes can cross the BBB through six different pathways: (i) passive paracellular diffusion, (ii) passive transcellular diffusion, (iii) solute carrier protein influx, (iv) receptor-mediated transcytosis, (v) adsorptive-mediated transcytosis and (vi) tight junction modulation.

PTD is primarily limited to small (<450 Da), lipophilic molecules capable of diffusing through the cell membrane. Molecules with high polar surface areas (>60-80 Å^2) and that tend to form more than 6 hydrogen bonds, a factor that increases the free energy requirement of moving from the aqueous blood to lipid membrane, are severely restricted from crossing by PTD (42). Additionally, tight junctions severely inhibit PPD of polar solutes. Thus, the polar solutes are generally incapable of passively diffusing through the BBB.

This restricted diffusion of polar solutes potentially isolates the brain from many essential nutrients, such as glucose, amino acids and nucleosides. However, the BBB endothelium contains a number of specific transport proteins to supply the brain with these substances (42). SCPs on the apical surface of the BBB recognize their solute in the blood and transport it into the BBB endothelial cells by facilitative diffusion. Equivalent transport proteins on the basal membrane then transport the solute into the brain parenchyma. SCPs are highly specific for their solute and often directional, limiting their ability to transport different or new compounds. Facilitative diffusion through SCPs is also restricted to small molecules capable of moving through the protein channels.

Transcytosis mechanism exist to transport macromolecules such as proteins across the BBB. In this process, events on the apical surface of the BBB trigger the formation of an endocytic vesicle encapsulating the macromolecules. The vesicle is then routed to the basolateral side of the endothelium where it fuses with the basal membrane to release the macromolecules into the brain. In RMT, the specific binding of a macromolecular ligand to its transcytosing receptor on the apical side of the BBB triggers the internalization. Dissociation of the ligand and receptor occurs during the cellular transit or the exocytic event. Several serum proteins use this process to enter the brain from circulation, including: (i) transferrin (Tf), (ii) insulin and (iii) low-density lipoprotein-receptor-related proteins 1 and 2 (LRP1 and LRP2) (42). In contrast, AMT is a non-specific process that requires the transcytosing protein to be highly cationic. Interaction with the negatively charged proteins on the endothelial cell surface induces transcytosis, though the exact mechanisms by which AMT occurs are not as well-understood as those for RMT (43).

The final mechanism for solute transport at the BBB is TJM. TJM can be induced pharmacologically or by cell signaling, and results in complete or partial opening of the PPD pathway. TJM mainly occurs in pathological conditions such as malignant gliomas (44).

1.2.3 Barrier integrity in HER2-positive breast cancer brain metastases

There is considerable debate in the brain metastasis research field regarding the extent to which the BBB remains intact with brain metastases in the form of the blood-tumor barrier (BTB). Imaging studies showing a greater uptake of contrast agents in brain metastases compared with healthy tissue have suggested that the lesions may have some increased permeability (Fig. 1.5). On the other hand, chemotherapy has been unambiguously ineffective in the clinic (10). Although metastatic cancer is generally considered incurable, brain metastases appear to be more refractory to standard therapeutics than systemic tumors. At least two theories may explain this phenomenon. First, metastatic tumor cells in the brain are more resistant to chemotherapy than those in systemic metastases either mediated by the brain microenvironment or as a result of their late development following multiple rounds of chemotherapy. Second, even if the barrier has some increased permeability, it is not sufficiently permeable to allow adequate drug accumulation in the brain metastases. To further complicate the debate, there is also evidence that suggests BBB/BTB permeability may be cancer type- and even subtype-dependent (45).

A B

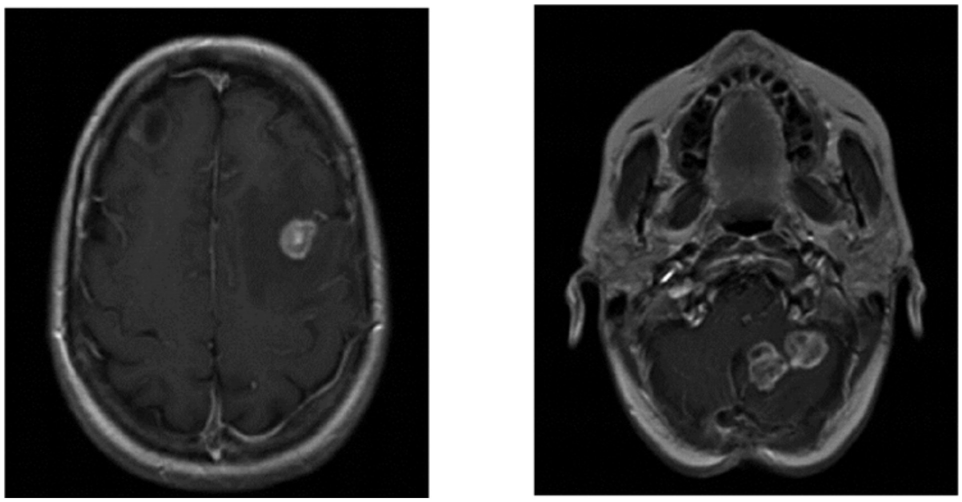

Fig. 1.5. Axial MRI images of multiple brain metastases in a HER2-positive breast cancer patient. Lesions in the left frontal lobe (A) and left cerebellum (B) show uptake of gadolinium contrast agent in T1-weighted scans. Images from (17).

In the case of HER2-positive breast cancer brain metastases, the available evidence suggests that both theories may be at play. Recent studies in experimental brain metastasis models indicate that the brain microenvironment has a role in resistance (46). Considerable evidence has also accumulated to suggest that HER2-targeted therapeutic efficacy is severely diminished by poor brain penetration through a non-permissive BBB/BTB (45,47,49,50). In one study, the ratio of trastuzumab levels in the serum to cerebrospinal fluid (CSF) was 420:1. Even after WBRT, which is thought to disrupt the BBB, the ratio only rose to 76:1 (47). These levels are considered subtherapeutic. However, the CSF represents a separate compartment from the brain parenchyma, separated from the brain by the glia limitans (48). Perhaps more convincing evidence for inadequate therapeutic penetration as a reason for its ineffectiveness comes from an investigation of uptake in brain metastases resected from HER2-positive breast cancer patients. Significant heterogeneity in lapatinib concentrations was observed both among patients and within individual lesions (49). This theory is further strengthened by a study characterizing the incidence and timing of isolated brain metastases in patients with HER2-positive, metastatic breast cancer treated with trastuzumab as first-line treatment. Approximately 10% of patients developed isolated brain metastases as first site of tumor progression, with brain progression occurring at a time when their systemic disease was responsive to trastuzumab (50). These data support the hypothesis that the brain is a “sanctuary site”, as the BBB/BTB limit the ability of drugs to achieve sufficient accumulation in brain metastases to elicit an antitumor response. Thus, new strategies to overcome impaired drug delivery to brain metastases are essential to improve clinical outcomes, particularly for HER2-positive, metastatic breast cancer patients.

1.3 Current approaches for drug delivery to the brain

1.3.1 Physically bypassing the BBB

Drug delivery methods that physically bypass the BBB have been investigated for several decades to treat brain diseases. Three similar approaches involving direct introduction of drug to the brain parenchyma have been developed with varying, but overall limited success, namely: (i) intracerebral implantation (ICI), (ii) intracerebroventricular (ICV) or intraventricular infusion and (iii) convection-enhanced diffusion or delivery (CED) (40).

ICI involves direct implantation of drugs into the brain parenchyma. This method was piloted in glioma patients by crudely placing a chemotherapeutic-soaked sponge in the tumor-resection cavity to provide immediate chemotherapy to residual tumor cells (51,52).

Following the introduction of biodegradable polymers to medicine in the 1980s, several drug-loaded, biodegradable wafers have been investigated using the same, but more-refined approach, particularly for gliomas (53,54). Similarly, ICV infusion involves direct intraventricular delivery of drugs to the CSF, allowing the drug to access the entire ventricular system. This approach has been moderately successful in cases where the disease target is in the subarachnoid space (55). However, both the ICI and ICV methods have demonstrated little to no clinical benefit over systemic treatments for most brain diseases, largely due to limited drug penetration from the site of introduction. Because these delivery methods are diffusion-mediated, drug concentration drops off exponentially with the distance from the implantation site (40).

CED attempts to improve upon the diffusional limitations of ICI and ICV. Unlike diffusion-limited delivery, CED provides pressure-driven bulk flow of drug into the brain parenchyma to enhance its interstitial penetration. The bulk flow is created by a small pressure gradient from an infusion pump that pushes the drug through a catheter targeted within the brain. Initial clinical investigation suggested that CED may hold some promise, effectively delivering therapeutics to substantial volumes of tissue (56). However, several technical limitations, such as the catheter design, infusate reflux and post-procedural imaging, have limited its reliability. Two CED treatments have reached phase III clinical trials in glioblastoma multiforme (GBM) patients, but ultimately failed owing in large part to these technical shortcomings (57). Research on CED delivery is ongoing to address these limitations.

1.3.2 Transiently disrupting the BBB

Methods to temporarily disrupt the BBB have also been investigated to enable brain delivery of circulating drugs. One such technique involves arterial injection of a hyperosmotic solution such as mannitol. The high salt concentration in the blood causes shrinkage of endothelial cells at the BBB endothelium and consequently stretching of tight junctions (58,59). Expansion of the tight junctions increases the permeability of the paracellular pathway, allowing circulating drugs to enter the brain. This procedure has been shown to improve delivery of therapeutics to brain tumors, and has been used most successfully for primary central nervous system lymphoma (60,61). Other agents such as bradykinin analogs have also been investigated (62). While this technique may be an effective means to deliver drugs to large brain regions, it is an invasive procedure that brings significant side effects, including seizures and hypotension (63). These effects are likely due to accumulation of serum proteins and toxic substances in the brain following widespread, non-specific disruption. Additionally, in the case of metastatic cancers, there is concern that BBB disruption may allow circulating cancer cells to more readily access the brain, potentially forming new brain lesions.

Recently, the use of focused ultrasound (FUS) combined with circulating microbubbles has been investigated as a method to more safely disrupt the BBB. The exact mechanism by which microbubble-enhanced FUS leads to BBB disruption remains unknown. Current understanding is that either FUS/microbubble interactions stretch the endothelium similar to hyperosmotic solutions or trigger a physiological response that leads to temporary BBB breakdown (63). Nevertheless, FUS has garnered considerable interest because it offers the potential to control the spatial location as well as the magnitude of BBB disruption through modification of the ultrasound parameters. Furthermore, the procedure can be easily repeated and is non-invasive. Recent studies in non-human primates have not shown the significant side effects observed for widespread BBB disruption (64). A pilot clinical trial using FUS to delivery doxorubicin to GBM patients has been completed, and a number of clinical trials are underway to investigate FUS in other brain diseases (65). Results from these trials are not yet available. In addition to efficacy, of particular concern is the long-term safety of this method in humans.

1.3.3 Exploiting endogenous solute transport systems at the BBB

Compared to the invasive, local strategies detailed above, therapeutics that are capable of entering the brain from circulation by using endogenous transport systems (detailed in section 1.2.2) offer a distinct advantage in treating diffuse brain diseases, including: (i) metastatic cancers with multiple foci, (ii) fingers of gliomas and (iii) neurodegenerative diseases. The human brain contains about 400 miles of blood vessels, corresponding to a total surface area for exchange near 20 m^2. Additionally, no cell in the brain is more than 25 µm away from a blood vessel, allowing for significantly shorter diffusional distances to reach the disease target compared to locally administered drugs (40). Even a macromolecular protein will diffuse this distance in less than a second (66).

Some small molecules are able to reach the brain through PTD. However, the molecular properties that favor PTD transport are significantly more restricted than those typically used to design small molecule drugs (Fig. 1.6). Generally, brain penetrant small molecules require a: (i) low molecular weight (<450 Da), (ii) limited polar surface area

(<60-80 Å^2), (iii) moderate lipophilicity (logP<5), (iv) neutral or basic pKa (7.5-10.5) and (v) limited number of hydrogen bond donors and acceptors (<7) (67). The vast majority of small molecule therapeutics do not meet these criteria, and are therefore ineffective in the treatment of brain diseases due to their low brain permeability.

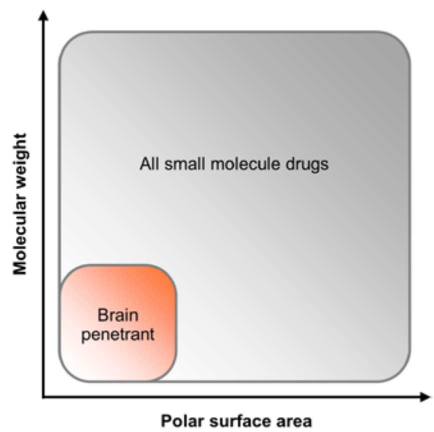

Fig. 1.6. Molecular properties that allow for small molecule drug brain penetration impose tight restrictions on drug design, particularly molecular weight and total polar surface area.

Another aspect affecting small molecule drug delivery to the brain – either systemically or by invasively bypassing or disrupting the BBB – is the presence of efflux pumps on the basal side of the endothelium. Specific ATP-binding cassette (ABC) efflux transporters exist to clear neurotoxins from the brain parenchyma, including: (i) p-glycoprotein, (ii) multidrug resistance-associated proteins and (iii) breast cancer-resistance protein (68). In fact, most small molecule chemotherapeutics have been shown to be substrates of one or more of these ABC transporters (69,70). Thus, small molecule drugs for the treatment of brain diseases must be designed not only for brain penetration, but also evasion of efflux pumps, severely limiting the treatment options using PTD.

Drug delivery using SCPs requires mimicking the endogenous small molecule ligand or conjugation of the drug to the substrate. This approach can be successful for small molecule drugs, such as gabapentin and L-dopa, both of which are primarily shuttled into the brain by the large neutral amino acid transporter (LAT1) (71,72). However, as with PTD, the potential chemistries compatible with SCPs are fairly limited, and neither approach is conductive to transport of large, macromolecular therapeutics, such as potent biologics and nanoscale drug delivery systems.

Of the endogenous transport mechanisms at the BBB, only the transcytosis pathways are compatible with delivery of macromolecular agents. Drug targeting using AMT relies on chemical modifications, such as polyamination of proteins, to increase their positive charge (73). However, the nonspecific nature of AMT severely limits its therapeutic potential, as broad cellular uptake can lead to off-target toxicities as well as less favorable pharmacokinetic properties. Additionally, positively charged compounds are known to disrupt the BBB (74), calling into question the safety of this approach as a means of increasing brain penetration.

Unlike AMT, the RMT pathway is highly specific. The idea of using this mechanism to shuttle therapeutics into the brain was proposed decades ago (40). The general approach has been to conjugate the drug to a ligand that binds a transcytosing receptor at the BBB endothelium. Binding of the ligand portion of the ligand-drug conjugate facilitates its transit across the BBB in the transcytosing vesicle. Then, once released in the brain, the drug can diffuse to its target. This strategy of "masking" the therapeutic has been dubbed the "Trojan-horse" approach to smuggling drugs into the brain (40). RMT across the BBB has already been investigated to deliver a variety of payloads to the brain, including: (i) protein-drug conjugates (75), (ii) therapeutic antibodies (76), (iii) liposomes (77) and (iv) nanoparticles (78,79).

1.4 Transferrin receptor (TfR)-targeted drug delivery to the brain

1.4.1 Receptor-mediated transcytosis (RMT) of transferrin (Tf)

Several receptors are known to undergo RMT at the BBB endothelium, and have been investigated for targeted drug delivery to the brain, including: (i) insulin receptor (InsR), (ii) transferrin receptor (TfR), (iii) low-density lipoprotein receptor-related protein 1 (LRP1) and (iv) folate receptor (80). Of these, the TfR pathway has been one of the most widely explored RMT systems for drug delivery.

TfR is a transmembrane homodimer of two glycoprotein subunits that regulates intracellular delivery of iron (81). Each TfR subunit can bind one iron-carrying Tf ligand (82). In most epithelial cells, binding of iron-loaded Tf (holo-Tf) triggers clathrin-mediated endocytosis of the protein-receptor complex. A drop in pH (to pH 5.5) within the endosome causes a conformation change in Tf, leading to the release of iron into the endosomal compartment and recycling of apo-Tf (Tf without bound iron) to the cell surface. The decreased affinity of apo-Tf for TfR at extracellular pH allows for its release from the receptor (83) (Fig. 1.7).

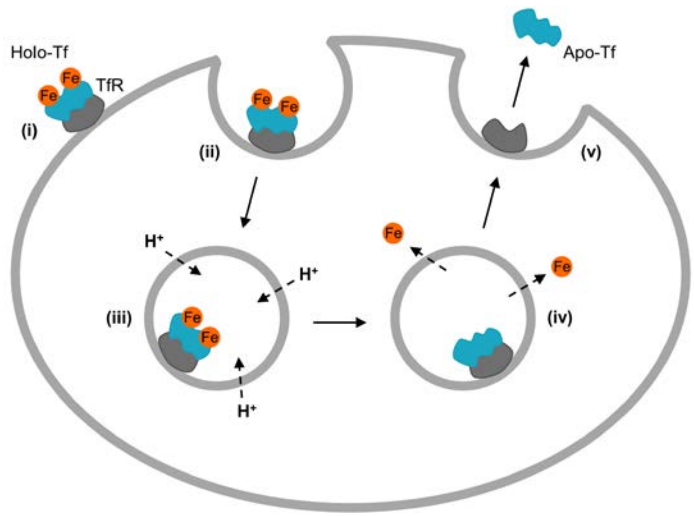

Fig. 1.7. Endocytic recycling of TfR in apolar cells. (**i**) Holo-Tf carrying two Fe^{3+} atoms binds TfR on the plasma membrane. (**ii**) Binding induces endocytosis of the Tf:TfR complex. (**iii**) Protons are actively pumped into the endosome, reducing the pH to ~5.5. (**iv**) Acidification of the endosome triggers a conformational change in Tf, leading to release of bound iron. (**v**) Recycling of TfR to the cell surface allows for release of iron-free Tf (apo-Tf).

In polarized cells such as the BBB endothelium, this process is slightly modified to allow Tf to enter the brain. After endocytosis, intracellular machinery sorts the Tf-containing vesicle to the transcytosis pathway, routing it across the cell to the basal membrane (83,84). Although there is still debate regarding the exact mechanism by which Tf is sorted to undergo transcytosis, it is well-established that Tf must undergo some portion of endocytosis before diverting to transcytosis (85,86).

TfR-targeting is an attractive strategy for drug delivery to the brain because it is highly expressed on the BBB endothelium (81). TfR is similarly upregulated in many cancers, and has been successfully targeted by siRNA-containing nanoparticles in clinical trials (88). Additionally, TfR at the BBB is not saturated by endogenous Tf, as seen in other tissues, providing accessible binding sites for targeted therapeutics (89). Thus, many groups have attempted to exploit this pathway by either developing antibodies to TfR or targeting with the Tf ligand.

1.4.2 Drug delivery across the BBB using anti-TfR antibodies (Abs)

Anti-TfR Abs have garnered the most interest because of their ability to bind TfR with high affinity and specificity as well as their ability to trigger endocytosis through binding of a different epitope than endogenous Tf (83,90). Pioneering studies in the early 1990s with an Ab against the rat TfR (OX26) were among the first to show that an anti-TfR Ab could cross the BBB and enter the brain (91,92). Several practical limitations, however, prevented the translation of these early studies to the clinic. Of particular concern was the observation that a majority of the Abs accumulated in the BBB endothelium, instead of penetrating the brain (93). The authors discussed the possibility of high-affinity Ab:TfR interactions preventing the release of OX26 into the brain following transcytosis, evidence for which would come many years later.

Subsequent studies began to uncover the mechanisms preventing accumulation of large numbers of anti-TfR Abs in the brain, leading to a resurgence in interest in the delivery strategy. The first of these studies showed that reducing the affinity of anti-TfR Abs to TfR maximizes their uptake into the brain parenchyma (94). The authors proposed that high-affinity Abs induce transcytosis, but remain bound to TfR once the vesicle fuses to the basal endothelium, and are thus unable to penetrate the brain while lower-affinity variants could dissociate from TfR because of their reduced affinity (Fig. 1.8). With this approach, they were able to deliver nearly 1% of the lower-affinity anti-TfR Ab to the brain parenchyma, an amount deemed therapeutically useful (94). However, this level of accumulation required extraordinarily high systemic doses – a cause for concern in future translational studies.

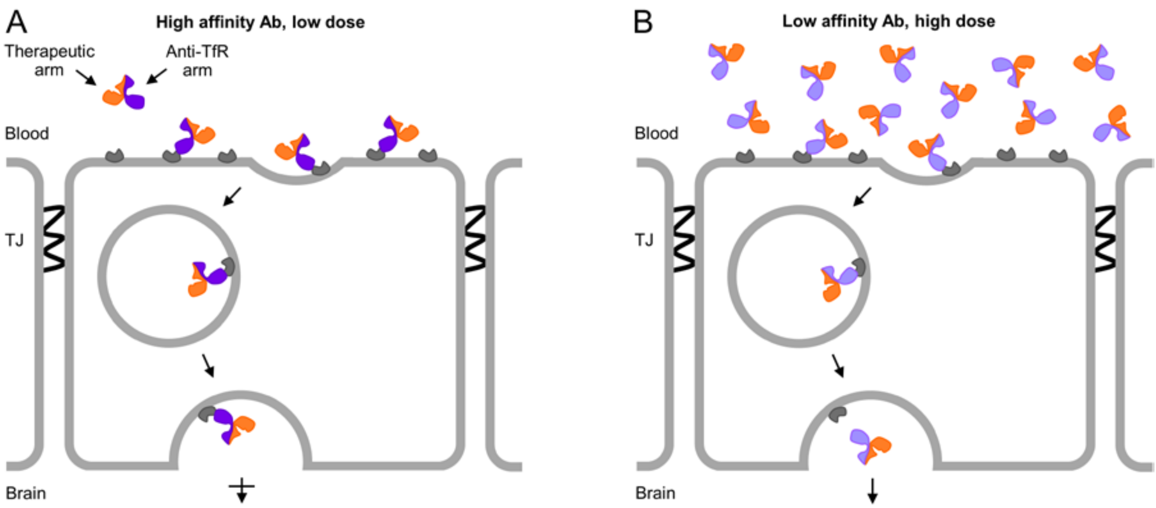

Fig. 1.8. Inverse relationship between the affinity of anti-TfR Abs and their brain uptake. High-affinity Abs transcytose the BBB endothelium, but are restricted from entering the brain by the strong Ab:TfR interactions (**A**), whereas lower-affinity variants can accumulate in the brain in greater numbers if administered at very high doses (**B**). TJ, tight junction.

Further investigation revealed that while greater brain exposure of anti-TfR Abs is achieved as the affinity for TfR is reduced, a different mechanism is at play – affinity influences the intracellular trafficking of anti-TfR Abs. High-affinity anti-TfR Abs are trafficked to the lysosome, while lower-affinity variants are more capable of transcytosis (95) (Fig. 1.9). Around the same time, it was shown that bivalent Ab:TfR binding also leads to lysosomal sorting, whereas monovalent binding facilitates transcytosis (96) (Fig. 1.10). Furthermore, recent evidence indicates that intracellular tubules mediate this sorting mechanism (97).

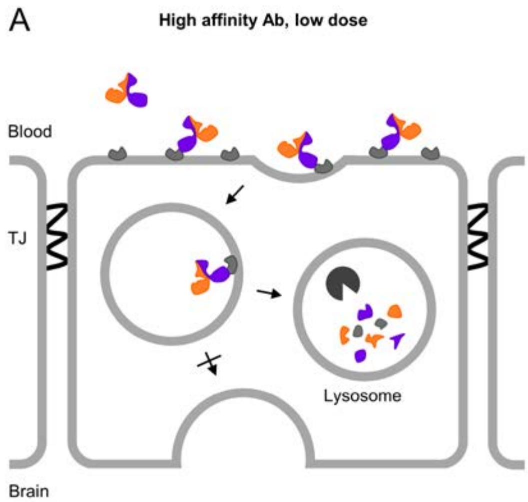

Fig. 1.9. Mechanism for decreased brain exposure of high-affinity anti-TfR Abs. High-affinity Abs are sorted to the lysosome for degradation (**A**), whereas lower-affinity variants may be transcytosed to the brain parenchyma (**B**).

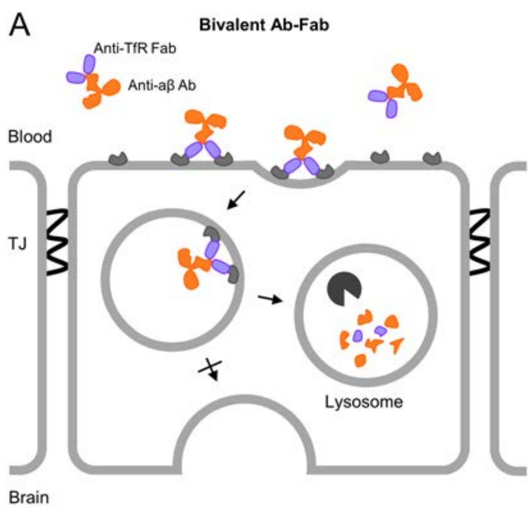

Fig. 1.10. Binding valency effect on intracellular sorting and transcytosis capacity of anti-TfR Abs. Bivalent Ab:TfR binding induces abnormal configuration of TfR and trafficking to the lysosome (**A**), whereas monovalent binding preserves natural trafficking, allowing for Ab transcytosis (**B**).

In addition to affinity and valency, recent in vitro results suggest that pH-sensitivity of TfR binding also affects intracellular trafficking of anti-TfR Abs; an Ab with reduced affinity at endosomal pH 5.5 showed a greater ability to transcytose than pH-independent

Abs of comparable affinities at extracellular pH 7.4 (98). These data suggest an approach in addition to reducing binding affinity that may facilitate greater brain parenchyma uptake of anti-TfR Abs – pH-dependent binding to TfR.

Despite a thorough understanding of the properties that favor transcytosis, several challenges exist in translating anti-TfR Abs into the clinic, including the need to: (i) dose very high quantities (90), (ii) mitigate effector-function driven safety concerns (99) and (iii) develop species-specific Abs (100).

1.4.3 Transport of TfR-targeted gold nanoparticles at the BBB

Motivated by the results from anti-TfR Ab trafficking at the BBB, our group began to investigate how fundamental aspects of TfR-targeted nanoparticle design affect transcytosis capacity, namely: (i) nanoparticle size, (ii) charge and (iii) targeting ligand density (101). Targeted nanoparticles were chosen for their ability to deliver large quantities and a variety of drugs to specific tissues at well-controlled release rates (detailed in section 1.5) (102). Initially, gold nanoparticles (AuNPs) of varying diameters (ca. 20-80 nm) were prepared with increasing quantities of Tf on the surface and assessed for their ability to enter the brain in mice. Zeta potentials of all formulations were kept near neutral by adding a dense polyethylene glycol (PEG) coating to the gold surface because it has been shown that near neutral to slightly anionic particles do not compromise BBB integrity, unlike cationic formulations (74).

In analogy to the results obtained with anti-TfR Abs, the authors found that Tf-coated AuNPs with reduced avidity to TfR showed the greatest ability to cross the BBB (101). As was initially proposed for anti-TfR Abs, they hypothesized that the numerous, multidentate Tf:TfR interactions with the high-avidity formulations prevented their release into the brain, while the lower-avidity formulations we able to complete the transcytosis process (Fig. 1.11). Interestingly, high-avidity, Tf-coated AuNPs were not seen within lysosomes using transmission electron microscopy (TEM) (101), indicating that vesicle trafficking may be affected by the particular targeting ligand. Furthermore, in contrast to anti-TfR Abs, these data suggest that the limiting factor in delivering Tf-coated AuNPs may not be sequestration to the lysosome, and that targeting TfR with its endogenous ligand may help promote transcytosis. Despite showing promise, questions regarding the need for very high systemic dosing to achieve sufficient brain accumulation led to alternative nanoparticle designs.

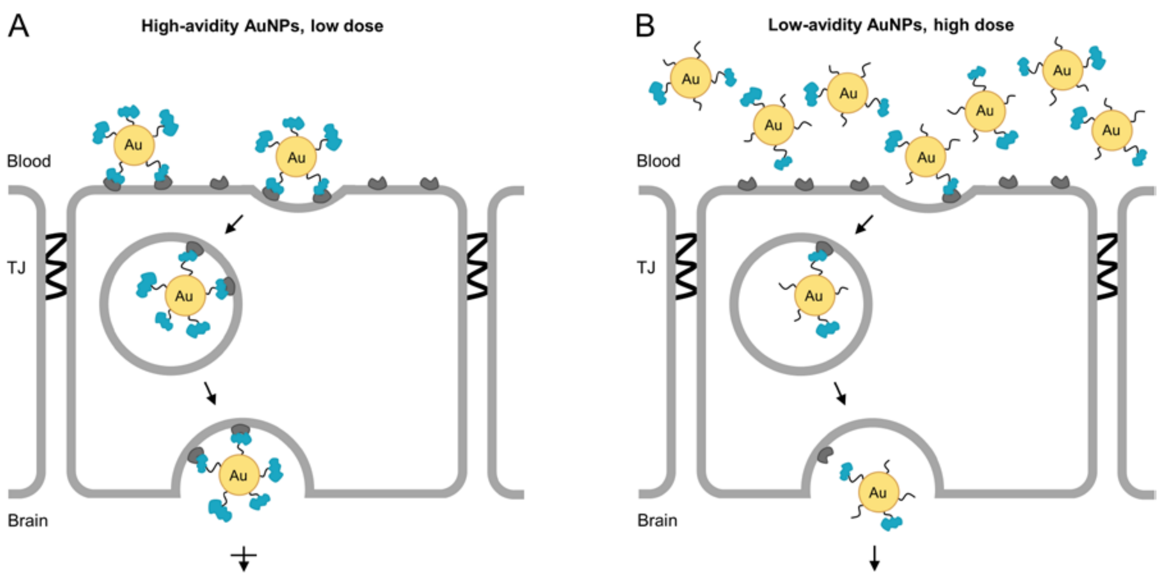

Fig. 1.11. Tf-coated nanoparticles are similarly constrained at the BBB compared to anti-TfR Abs. (**A**) High-avidity AuNPs are held up by the BBB endothelium, whereas (**B**) lower-avidity AuNPs can accumulate in the brain in greater amounts, but only with very high systemic dosing.

Recently, our group incorporated an acid-cleavable targeting strategy into the nanoparticle design to increase the ability of high-avidity nanoparticles to enter the brain (79). With this design, nanoparticles can bind TfR with high avidity on the blood side of the BBB to enable practical, systemic dosing, but shed the targeting ligands upon acidification during transcytosis (83,103), allowing free diffusion into the parenchyma (Fig. 1.12). Incorporation of an acid-cleavable linkage between Tf and the nanoparticle core increased brain accumulation of high-avidity Tf-coated AuNPs nearly 3-fold (79). In contrast, no improvement was observed with high-affinity anti-TfR-coated AuNPs with the cleavable linker, consistent with their trafficking to the lysosome. These results further bolster the hypothesis that intracellular trafficking may be affected by the particular targeting ligand, and demonstrate the utility of the acid-cleavable targeting scheme to increase brain penetration of nanoparticles.

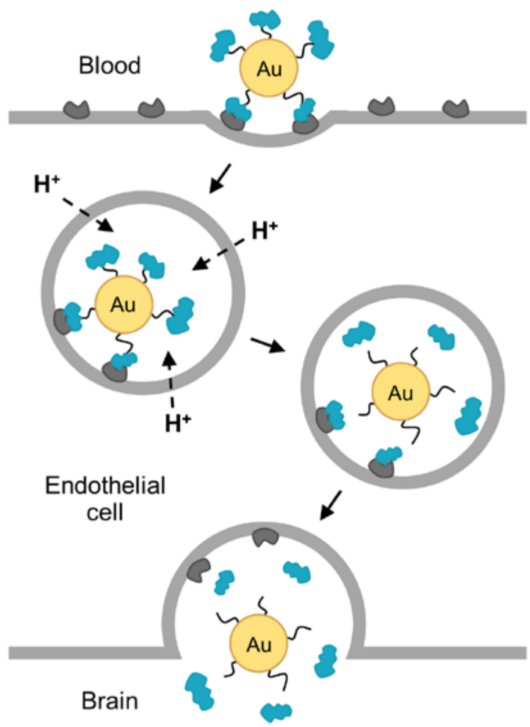

Fig. 1.12. Acid-cleavable targeting strategy to increase brain uptake of high-avidity nanoparticles. (**i**) High-avidity Tf-coated AuNPs readily bind TfR on the blood side of the BBB, inducing endocytosis of the Tf-coated AuNP:TfR complex. (**ii**) Protons are actively pumped into the endosome, reducing the pH to ~5.5. (**iii**) Acidification of the endosome triggers detachment of Tf from the AuNP surface. (**iv**) Vesicle fusion with the basal membrane allows for free diffusion of the AuNP into the brain parenchyma.

1.5 Nanoparticle drug delivery systems

Nanoparticles have garnered tremendous interest in the medical community over the last several decades. They offer several distinct advantages for drug delivery over standard therapeutics, including their ability to: (i) improve the pharmacologic profile of a drug without altering the molecule itself, (ii) be loaded with large quantities of drug compared to ligand-drug conjugates (by several orders of magnitude), (ii) release drugs at a tunable rate, (iv) deliver multiple therapeutic agents simultaneously at controlled ratios and (v) accumulate within specific tissues, thereby enhancing efficacy and minimizing off-target toxicities (102). Moreover, nanoparticles have proven clinical efficacy, with several formulations receiving FDA approval and on the market, and hundreds more in various stages of preclinical and clinical development for cancer therapy (104).

1.5.1 Polymeric nanoparticle formulations

In particular, there is growing optimism for polymeric nanoparticle formulations (105-107). The versatility of polymer chemistry has enabled the development of different types of nanoparticle systems to either encapsulate or covalently attach active drug molecules with distinct physiochemical structures and properties. Several FDA-approved polymers, such as *N*-(2-hydroxypropyl)methacrylamide (HPMA), poly(lactic acid) (PLA), poly(lactic-co-glycolic acid) (PLGA), polycaprolactone (PCL), and polyethylene glycol (PEG) have been developed for these delivery systems (107). The most common polymeric nanoparticle platforms include solid polymeric nanoparticles, polymeric micelles, polymersomes, dendrimers, and polymer-drug conjugates (Fig. 1.13).

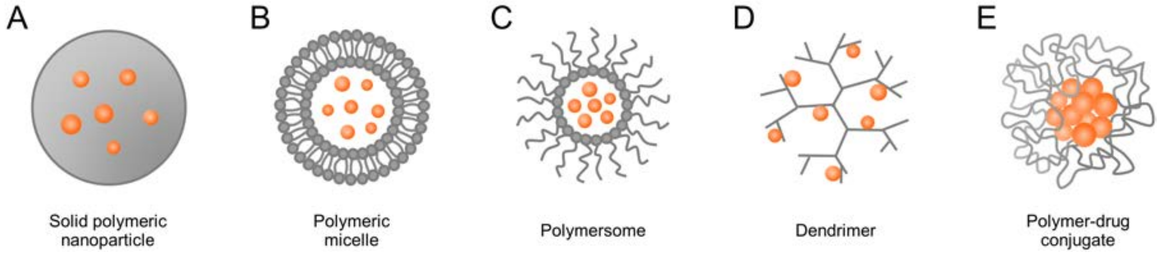

Fig. 1.13. Types of polymeric nanoparticle systems for drug delivery. Gray denotes polymeric material and orange active drug. (**A**) Solid polymeric nanoparticles are carriers in which a drug is encapsulated in a polymer matrix. (**B**) Polymeric micelles are formed by amphiphilic di- or tri-block copolymers, resulting in a core/shell structure. Drugs are encapsulated within the hydrophobic core. (**C**) Polymersomes are polymeric analogs of liposomes. Amphiphilic block copolymers assemble a lipid bilayer-like structure, enclosing an aqueous core containing drug molecules. (**D**) Dendrimers are synthetic, branched polymeric macromolecules that form star-like structures. Typically, drug molecules are conjugated to the scaffold. (**E**) Polymer-drug conjugates are formulations where one or more drug(s) is covalently attached to a linear, hydrophilic polymer. The amphiphilic nature of the conjugate material (hydrophilic polymer/hydrophobic drug) often drives its assembly into nanoparticles in aqueous media.

Of these polymeric nanoparticle systems, polymer-drug conjugates are the most actively explored (102,108,109) and are of greatest relevance to this work. The covalent bond between the polymer and drug offers significant opportunity for greater control of drug release through design of specific chemical linkers. Moreover, higher drug loadings can generally be achieved with polymer-drug conjugates compared to encapsulation techniques, thereby enhancing the potency of nanoparticles that reach the site of disease (110). However, this platform also comes with challenges, as not all drugs have functional groups that allow for simple, reversible covalent conjugation (detailed in Appendix A). Nevertheless, polymer-drug conjugates remain an attractive delivery platform, and many have been successfully translated to the clinic for cancer therapy (108,109), including CRLX101 (IT-101), a nanoparticle therapeutic developed in our group (111).

1.5.2 Passive and active targeting of nanoparticles

As mentioned, one of the advantages of nanoparticle therapeutics is their ability to achieve preferential accumulation in targeted tissues or cells. Two approaches are primarily used to facilitate nanoparticle homing to the desired site: passive and active targeting. Passive targeting involves the use of disease-specific features such as enhanced vascular permeability in tumors, whereas active targeting is achieved by adding a targeting ligand to the surface of nanoparticles to direct preferential accumulation (102). A number of types of affinity ligands have been explored for active targeting of polymeric nanoparticles, including peptides and antibodies (112,113). The targeting agent enables nanoparticle binding to extracellular matrix proteins in the diseased tissue or to antigens on the plasma membrane of target cells, facilitating their endocytic internalization (102). Moreover, actively-targeted nanoparticles have proven more effective than their non-targeted counterparts, largely due to their ability to be retained by target cells and locally release the drug (114).

1.5.3 Stimuli-responsive systems

Stimuli-responsive systems add a further level of refinement to these nanoparticle formulations. The general approach has been to design systems that have the ability to respond to environmental changes at the site of action (e.g. pH, temperature), triggering destabilization or degradation and allowing release of the drug (102). Many types of stimuli-responsive nanomedicines have been developed (115,116), with some reaching clinical trials (117). For polymeric nanoparticles, stimuli-responsive chemistry has been incorporated both at the point of attachment of stabilizing polymers or within the polymer chain itself (118,119). However, our acid cleavable targeting strategy (79) that was developed to improve the ability of high-avidity nanoparticles to enter the brain is the first demonstration of using stimuli-responsive chemistry to facilitate intact nanoparticle transit across cellular barriers.

1.6 Thesis objectives and organization

Previous studies showed that attaching TfR-targeting ligands to the nanoparticle core via a link that would cleave during BBB transcytosis could enable high-avidity AuNPs to cross the BBB and accumulate in the brain. However, the acid-cleavable linker investigated did not provide optimal cleavage kinetics to remove all the targeting ligand during transcytosis (79). The goal of this work was to determine whether TfR-targeted, polymer-drug conjugate nanoparticles using an improved acid-cleavable chemistry could be used to deliver pharmacologically active amounts of drug to the brain parenchyma (Fig. 1.14).

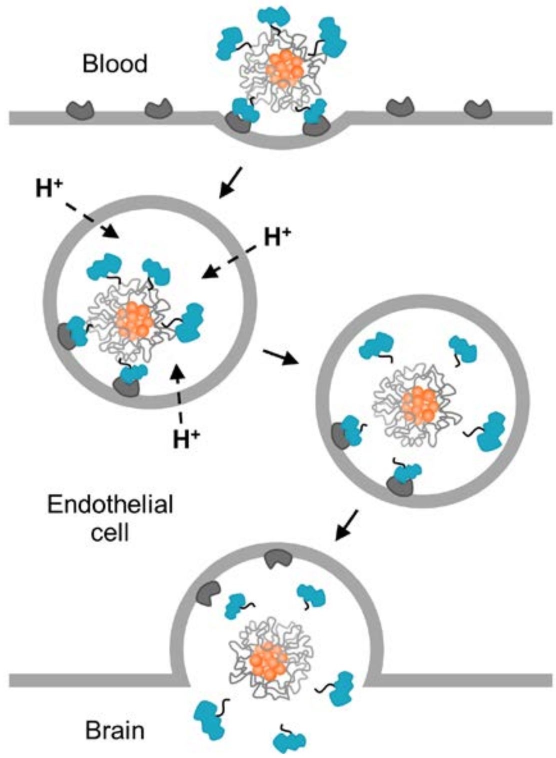

Fig. 1.14. Brain delivery of TfR-targeted, therapeutic nanoparticles using improved acid-cleavable targeting chemistry. Following endocytosis of the nanoparticle, acidification of the endosome occurs within minutes (120). Tf has been shown to transcytose within 30 minutes of systemic injection (121). Thus, for optimal transcytosis, TfR-targeting ligands must cleave on the order of tens of minutes within the acidified endosome to release the nanoparticle core. Additionally, the polymer-drug conjugate linker within the core must remain stable within this timeframe to allow for delivery of intact nanoparticles to the brain and their subsequent diffusion into the parenchyma.

First, in an attempt to create a clinically representative, non-permissive barrier to standard therapeutics, a new murine model of HER2-positive breast cancer brain metastasis was developed that more closely resembles human brain metastasis development (Chapter II). Initial characterization revealed that brain metastases established by this new method were not responsive to standard HER2-targeted agents, replicating the clinical situation.

Next, the newly developed model as well as two common models from the literature were used to evaluate the efficacy and brain uptake of TfR-targeted, single-agent therapeutic nanoparticles (Chapter III). TfR-targeted, therapeutic nanoparticles showed significant accumulation in brain metastases, and led to improved antitumor activity compared with free drug and non-targeted nanoparticles across all models investigated. Furthermore, TfR-targeted nanoparticles showed an increased ability to cross an intact BBB, resulting in whole-brain penetration. Additionally, a significant antitumor response as well as brain tumor accumulation of non-BBB-penetrant small molecule and non-targeted nanoparticle therapeutics were observed in the most commonly used model from the literature. Both the new model and one emerging in the literature provided for a more intact BBB/BTB. These data show that the method of establishing metastatic brain tumors can dramatically affect the efficacy of therapeutics and their brain penetration.

1.7 References

1. Siegel RL, Miller KD, Jemal A (2018) Cancer statistics, 2018. *CA: A Cancer Journal for Clinicians* 68(1):7–30.

2. Siegel RL, Miller KD, Jemal A (2017) Cancer statistics, 2017. *CA: A Cancer Journal for Clinicians* 66(1):7–30.

3. American Cancer Society. *Cancer treatment & survivorship facts & figures, 2016-2017.* Atlanta: American Cancer Society; 2016.

4. Yu PP (2016) Challenges in measuring cost and value in oncology: Making it personal. *Value in Health* 19(5):520–524.

5. Bluethmann SM, Mariotto AB, Rowland JH (2016) Anticipating the "silver tsunami": Prevalence trajectories and comorbidity burden among older cancer survivors in the United States. *Cancer Epidemiology, Biomarkers & Prevention* 25(7):1029–1036.

6. American Society of Clinical Oncology (2017) The state of cancer care in America, 2017: A report by the American Society of Clinical Oncology. *Journal of Oncology Practice* 13(4):e353–e394.

7. Hodi FS, Kluger H, Sznol M, Carvajal R, Lawrence D, et al. (2016) Durable, long-term survival in previously treated patients with advanced melanoma (MEL) who received nivolumab (NIVO) monotherapy in a phase I trial. *Proceedings: AACR 107th Annual Meeting* (abstract CT001).

8. Robert C, Ribas A, Hamid O, Daud A, Wolchok JD, et al. (2016) Three-year overall survival for patients with advanced melanoma treated with pembrolizumab in KEYNOTE-001. *Journal of Clinical Oncology* 34:15 (abstract 9503).

9. Eggermont AM, Chiarion-Sileni V, Grob JJ, Dummer R, Wolchok JD, et al. (2016) Prolonged survival in stage III melanoma with ipilimumab adjuvant therapy. *The New England Journal of Medicine* 375(19):1845–1855.

10. Steeg PS, Camphausen KA, Smith QR (2011) Brain metastases as preventive and therapeutic targets. *Nature Reviews Cancer* 11(5):352–363.

11. Yamanaka R (2009) Medical management of brain metastases from lung cancer (Review). *Oncology Reports* 22(6):1269–1276.

12. Dawe DE, Greenspoon JN, Ellis PM (2014) Brain metastases in non-small cell lung cancer. *Clinical Lung Cancer* 15(4):249–257.

13. McWilliams RR, Rao RD, Buckner JC, Link MJ, Markovic S, Brown PD (2008) Melanoma-induced brain metastases. *Expert Review of Anticancer Therpay* 8(5):743–755.

14. Chapman PB (2018) Changing the standard of care for treating melanoma brain metastases. *The Lancet Oncology* 19(5):589–591.

15. Kennecke H, Yerushalmi R, Woods R, Cheang MC, Voduc D, et al. (2010) Metastatic behavior of breast cancer subtypes. *Journal of Clinical Oncology* 28(20):3271–3277.

16. Aversa C, Rossi V, Geuna E, Martinello R, Milani A, et al. (2014) Metastatic breast cancer subtypes and central nervous system metastases. *Breast* 23(5):623–628.

17. Lin NU, Winer EP (2007) Brain metastases: The HER2 paradigm. *Clinical Cancer Research* 13(6):1648–1655.

18. Bendell JC, Domchek SM, Burstein HJ, Harris L, Younger J, et al. (2003) Central nervous system metastases in women who receive trastuzumab-based therapy for metastatic breast carcinoma. *Cancer* 97(12):2972–2977.

19. Soffietti R, Cornu P, Delattre JY, Grant R, Graus F, et al. (2006) EFNS Guidelines on diagnosis and treatment of brain metastases: report of an EFNS Task Force. *European Journal of Neurology* 13(7):674–681.

20. Forsyth PA, Posner JB (1993) Headaches in patients with brain tumors: a study of 111 patients. *Neurology* 43(9):1678–1683.

21. Fink KR, Fink JR (2013) Imaging of breast metastases. *Surgical Neurology International* 4(Suppl 4):S209–S219.

22. Owonikoko TK, Arbiser J, Zelnak A, Shu HK, Shim H, et al. (2014) Current approaches to the treatment of metastatic brain tumours. *Nature Reviews Clinical Oncology* 11(4):203–222.

23. Cairncross JG, Kim JH, Posner JB (1980) Radiation therapy for brain metastases. *Annals of Neurology* 7(6):529–541.

24. Borgelt B, Gelber R, Kramer S, Brady LW, Chang CH, et al. (1980) The palliation of brain metastases: final results of the first two studies by the Radiation Therapy Oncology Group. *International Journal of Radiation Oncology, Biology, Physics* 6(1):1–9.

25. Garber ST, Jensen RL (2012) Image guidance for brain metastases resection. *Surgical Neurology International* 3(Suppl 2):S111–S117.

26. Trudeau ME, Crump M, Charpentier D, Yelle L, Bordeleau L, et al. (2006) *Annals of Oncology* 17(6):952–956.

27. Mehta MP, Paleologos NA, Mikkelsen T, Robinson PD, Ammirati M, et al. (2010) The role of chemotherapy in the management of newly diagnosed brain metastases: a systematic review and evidence-based clinical practice guideline. *Journal of Neuro-Oncology* 96(1):71–83.

28. Boogerd W, Dalesio O, Bais EM, van der Sande JJ (1992) Response of brain metastases from breast cancer to systemic chemotherapy. *Cancer* 69(4):972–980.

29. Quirt I, Verma S, Petrella T, Bak K, Charette M (2007) Temozolomide for the treatment of metastatic melanoma: a systematic review. *The Oncologist* 12(9):1114–1123.

30. Lin NU, Diéras V, Paul D, Lossignol D, Christodoulou C, et al. (2009) Multicenter phase II study of lapatinib in patients with brain metastases from HER2-positive breast cancer. *Clinical Cancer Research* 15(4):1452–1459.

31. Slamon DJ, Clark GM, Wong SG, Levin WJ, Ullrich A, McGuire WL (1987) Human breast cancer: Correlation of relapse and survival with amplification of the HER-2/*neu* oncogene. *Science* 235(4785):177–182.

32. Slamon DJ, Leyland-Jones B, Shak S, Fuchs H, Paton V, et al (2001) Use of chemotherapy plus a monoclonal antibody against HER2 for metastatic breast cancer that overexpresses HER2. *The New England Journal of Medicine* 344(11):783–792.

33. Bendell JC, Domchek SM, Burstein HJ, Harris L, Younger J, et al. (2003) Central nervous system metastases in women who receive trastuzumab-based therapy for metastatic breast carcinoma. *Cancer* 97(12):2972–2977.

34. Altaha R, Crowell E, Ducatman B, Higa G, Abraham J (2004) Risk of brain metastases in HER2/neu-positive breast cancer. *Journal of Clinical Oncology* 22(14 Suppl):682.

35. Clayton AJ, Danson S, Jolly S, Ryder WD, Burt PA, et al. (2004) Incidence of cerebral metastases in patients treated with trastuzumab for metastatic breast cancer. *British Journal of Cancer* 91(4):639–643.

36. Stemmler HJ, Kahlert S, Siekiera W, Untch M, Heinrich B, Heinemann V (2006) Characteristics of patients with brain metastases receiving trastuzumab for HER2 overexpressing metastatic breast cancer. *Breast* 15(2):219–225.

37. Yau T, Swanton C, Chua S, Sue A, Walsh G, et al. (2006) Incidence, pattern, and timing of brain metastases among patients with advanced breast cancer treated with trastuzumab. *Acta Oncologica* 45(2):196–201.

38. Ramakrishna N, et al. (2014) Recommendations on disease management for patients with advanced human epidermal growth factor receptor 2-positive breast cancer and brain metastases: American Society of Clinical Oncology clinical practice guideline. *Journal of Clinical Oncology* 32(19):2100–2108.

39. Sledge GW Jr. (2011) HER2011: the changing face of HER2-positive breast cancer. *Clinical Breast Cancer* 11(1):9.

40. Pardridge WM (2004). The blood-brain barrier: bottleneck in brain drug development. *NeuroRx* 2(1):3–14.

41. Abbott NJ (2013) Blood–brain barrier structure and function and the challenges for CNS drug delivery. *Journal of Inherited Metabolic Disease* 36(3):437–449.

42. Abbott NJ, Patabendige AAK, Dolman DEM, Yusof SR, Begley DJ (2010) Structure and function of the blood–brain barrier. *Neurobiology of Disease* 37(1):13–25.

43. Hervé F, Ghinea N, Scherrmann JM (2008) CNS delivery via adsorptive transcytosis. *The AAPS Journal* 10(3):455–472.

44. Watkins S, Robel S, Kimbrough IF, Robert SM, Ellis-Davies G, Sontheimer H (2014). Disruption of astrocyte-vascular coupling and the blood-brain barrier by invading glioma cells. *Nature Communications* 5:4196.

45. Yonemori K, Tsuta K, Ono M, Shimizu C, Hirakawa A, et al. (2010) Disruption of the blood brain barrier by brain metastases of triple-negative and basal-type breast cancer but not HER2/neu-positive breast cancer. *Cancer* 116(2):302–308.

46. Kodack DP, Askoxylakis V, Ferraro GB, Sheng Q, Badeaux M, et al. (2017) The brain microenvironment mediates resistance in luminal breast cancer to PI3K inhibition through HER3 activation. *Science Translational Medicine* 9(391).

47. Stemmler HJ, Schmitt M, Willems A, Bernhard H, Harbeck N, Heinemann V (2007) Ratio of trastuzumab levels in serum and cerebrospinal fluid is altered in HER2-positive breast cancer patients with brain metastases and impairment of the blood-brain barrier. *Anticancer Drugs* 18(1):23–28.

48. Engelhardt B, Carare RO, Bechmann I, Flügel A, Laman JD, Weller RO (2016) Vascular, glial, and lymphatic immune gateways of the central nervous system. *Acta Neuropathologica* 132(3):317–338.

49. Morikawa A, et al. (2015) Capecitabine and lapatinib uptake in surgically resected brain metastases from metastatic breast cancer patients: a prospective study. *Neuro Oncol* 17(2):289–295.

50. Burstein HJ, Lieberman G, Slamon DJ, Winer EP, Klein P (2005) Isolated central nervous system metastases in patients with HER2-overexpressing advanced breast cancer treated with first-line trastuzumab-based therapy. *Annals of Oncology* 16(11):1772–1777.

51. Heppner F, Diemath HE (1963) Local chemotherapy of brain tumors. *Acta Nuerochirurgica* 11:287–293.

52. Ringkjob R (1968) Treatment of intracranial gliomas and metastatic carcinomas by local application of cytostatic agents. *Acta Neurologica Scandinavica* 44(3):318–322.

53. Tomita T (1991) Interstitial chemotherapy for brain tumors: review. *Journal of Neuro-Oncology 10*(1):57–74.

54. Wait S1, Prabhu RS, Burri SH, Atkins TG, Asher AL (2015) Polymeric drug delivery for the treatment of glioblastoma. *Neuro-Oncology* 17(Suppl 2):ii9–ii23.

55. Fleischhack G, Jaehde U, Bode U (2005) Pharmacokinetics following intraventricular administration of chemotherapy in patients with neoplastic meningitis. *Clinical Pharmacokinetics* 44(1):1–31.

56. Vogelbaum MA, Aghi MK (2015) Convection-enhanced delivery for the treatment of glioblastoma. *Neuro-Oncology* 17(Suppl 2):ii3–ii8.

57. Jahangiri A, Chin AT, Flanigan PM, Chen R, Bankiewicz K, Aghi MK (2017) Convection-enhanced delivery in glioblastoma: a review of preclinical and clinical studies. *Journal of Neurosurgery* 126(1):191–200.

58. Rapoport SI (1970) Effect of concentrated solutions on blood-brain barrier. *Journal of Physiology* 219(1):270–274.

59. Rapoport SI (2001) Advances in osmotic opening of the blood–brain barrier to enhance CNS chemotherapy. *Expert Opinion on Investigational Drugs* 10:1809–1818.

60. Muldoon LL, Soussain C, Jahnke K, Johanson C, Siegal T, et al. (2006) Chemotherapy delivery issues in central nervous system malignancy: a reality check. *Journal of Clinical Oncology* 25(16):2295–2305.

61. Angelov L, Doolittle ND, Kraemer DF, Siegal T, Barnett GH, et al. (2009) Blood-brain barrier disruption and intra-arterial methotrexate-based therapy for newly diagnosed primary CNS lymphoma: a multi-institutional experience. *Journal of Clinical Oncology* 27(21):3503–3509.

62. Eichler AF, Chung E, Kodack DP, Loeffler JS, Fukumura D, Jain RK (2011) The biology of brain metastases-translation to new therapies. *Nature Reviews Clinical Oncology* 8(6):344–356.

63. Aryal M, Arvanitis CD, Alexander PM, McDannold N (2014) Ultrasound-mediated blood-brain barrier disruption for targeted drug delivery in the central nervous system. *Advanced Drug Delivery Reviews* 72:94–109.

64. McDannold N, Arvanitis CD, Vykhodtseva N, Livingstone MS (2012) Temporary disruption of the blood-brain barrier by use of ultrasound and microbubbles: safety and efficacy evaluation in rhesus macaques. *Cancer Research* 72(14):3652–3663.

65. Focused Ultrasound Foundation (2017) *2017 year in review*. Retrieved from Focused Ultrasound Foundation Website: http://goo.gl/VAoaG2.

66. Pardridge WM (2001) *Brain drug targeting: the future of brain drug development.* (Cambridge University Press, Cambridge).

67. Pajouhesh H, Lenz GR (2005) Medicinal chemical properties of successful central nervous system drugs. *NeuroRx* 2(4):541–553.

68. Deeken JF, Löscher W (2007) The blood-brain barrier and cancer: transporters, treatment, and Trojan horses. *Clinical Cancer Research* 13(6):1663–1674.

69. Szakács G, Paterson JK, Ludwig JA, Booth-Genthe C, Gottesman MM (2006) Targeting multidrug resistance in cancer. *Nature Reviews Drug Discovery* 5(3):219–234.

70. Noguchi K, Katayama K, Mitsuhashi J, Sugimoto Y (2009) Functions of the breast cancer resistance protein (BCRP/ABCG2) in chemotherapy. *Advanced Drug Delivery Reviews* 61(1):26–33.

71. Cundy KC, Branch R, Chernov-Rogan T, Dias T, Estrada T, et al. (2004) XP13512 [(+/-)-1-([(alpha-isobutanoyloxyethoxy)carbonyl] aminomethyl)-1-cyclohexane acetic acid], a novel gabapentin prodrug: I. Design, synthesis, enzymatic conversion to gabapentin, and transport by intestinal solute transporters. *The Journal of Pharmacology and Experimental Therapeutics* 311(1):315–323.

72. Gomes P, Soares-da-Silva P (1999) L-DOPA transport properties in an immortalised cell line of rat capillary cerebral endothelial cells, RBE 4. *Brain Research* 829:143–150.

73. Poduslo JF, Curran GL (1996) Polyamine modification increases the permeability of proteins at the blood-nerve and blood–brain barriers. *Journal of Neurochemistry* 66(4):1599–1609.

74. Lockman PR, Koziara JM, Mumper RJ, Allen DD (2004) Nanoparticle surface charges alter blood–brain barrier integrity and permeability. *Journal of Drug Targeting* 12(9-10):635–641.

75. Thomas FC, Taskar K, Rudraraju V, Goda S, Thorsheim HR (2009) Uptake of ANG1005, a novel paclitaxel derivative, through the blood-brain barrier into brain and experimental brain metastases of breast cancer. *Pharmaceutical Research* 26(11):2486–2494.

76. Yu YJ, Watts RJ (2013) Developing therapeutic antibodies for neurodegenerative disease. *Neurotherapeutics* 10(3):459–472.

77. Schnyder A, Huwyler J (2005) Drug transport to brain with targeted liposomes. *NeuroRx* 2(1):99–107.

78. Kreuter J, Shamenkov D, Petrov V, Ramge P, Cychutek K, et al. (2002) Apolipoprotein-mediated transport of nanoparticle-bound drugs across the blood-brain barrier. *Journal of Drug Targeting* 10(4):317–325.

79. Clark AJ, Davis ME (2015) Increased brain uptake of targeted nanoparticles by adding an acid-cleavable linkage between transferrin and the nanoparticle core. *Proceedings of the National Academy of Sciences USA* 112(40):12486–12491.

80. Freskgård P-O, Urich E (2017) Antibody therapies in CNS diseases. *Neuropharacology* 120:38–55.

81. Jefferies WA, Brandon MR, Hunt SV, Williams AF, Gatter KC, Mason DY (1984) Transferrin receptor on endothelium of brain capillaries. *Nature* 312(5990):162–163.

82. Moos T, Morgan EH (2000) Transferrin and transferrin receptor function in brain barrier systems. *Cellular and Molecular Neurobiology* 20(1):77–95.

83. Widera A, Norouziyan F, Shen WC (2003) Mechanisms of TfR-mediated transcytosis and sorting in epithelial cells and applications toward drug delivery. *Advanced Drug Delivery Reviews* 55(11):1439–1466.

84. Sahay G, Alakhova DY, Kabanov AV (2010) Endocytosis of nanomedicines. *Journal of Controlled Release* 145(3):182–195.

85. Skarlatos S, Yoshikawa T, Pardridge WM (1995) Transport of [^{125}I]transferrin through the rat blood-brain barrier. *Brain Research* 683(2):164–171.

86. Visser CC, Voorwinden LH, Crommelin DJ, Danhof M, de Boer AG (2004) Characterization and modulation of the transferrin receptor on brain capillary endothelial cells. *Pharmaceutic Research* 21(5):761–769.

87. Uchida Y, Ohtsuki S, Katsukura Y, Ikeda C, Suzuki T, et al. (2011) Quantitative targeted absolute proteomics of human blood-brain barrier transporters and receptors. *Journal of Neurochemistry* 117(2):333–345.

88. Eliasof S, Lazarus D, Peters CG, Case RI, Cole RO, et al. (2013) Correlating preclinical animal studies and human clinical trials of a multifunctional, polymeric nanoparticle. *Proceedings of the National Academy of Sciences USA* 110(37):15127–15132.

89. Gatter KC, Brown G, Trowbridge IS, Woolston RE, Mason DY (1983) Transferrin receptors in human tissues: their distribution and possible clinical relevance. *Journal of Clinical Pathology* 36(5):539–545.

90. Lajoie JM, Shusta EV (2015) Targeting receptor-mediated transport for delivery of biologics across the blood-brain barrier. *Annual Review of Pharmacology and Toxicology* 55:613–631.

91. Friden PM, Walus LR, Musso GF, Taylor MA, Malfroy B, Starzyk RM (1991) Anti-transferrin receptor antibody and antibody-drug conjugates cross the blood-brain barrier. *Proceedings of the National Academy of Sciences USA* 88(11):4771–4775.

92. Pardridge WM, Buciak JL, Friden PM (1991) Selective transport of an anti-transferrin receptor antibody through the blood–brain barrier in vivo. *Journal of Pharmacology and Experimental Therapeutics* 259(1):66–70.

93. Moos T, Morgan EH (2001) Restricted transport of anti-transferrin receptor antibody (OX26) through the blood–brain barrier in the rat. *Journal of Neurochemistry* 79(1):119–129.

94. Yu YJ, Zhang Y, Kenrick M, Hoyte K, Luk W, et al. (2011) Boosting brain uptake of a therapeutic antibody by reducing its affinity for a transcytosis target. *Science Translational Medicine* 3(84):84ra44.

95. Bien-Ly N, Yu YJ, Bumbaca D, Elstrott J, Boswell CA, et al. (2014) Transferrin receptor (TfR) trafficking determines brain uptake of TfR antibody affinity variants. *The Journal of Experimental Medicine* 211(2):233–244.

96. Niewoehner J, Bohrmann B, Collin L, Urich E, Sade H, et al. (2014) Increased brain penetration and potency of a therapeutic antibody using a monovalent molecular shuttle. *Neuron* 81(1):49–60.

97. Villaseñor R, Schilling M, Sundaresan J, Lutz Y, Collin L (2017) Sorting tubules regulate blood-brain barrier transcytosis. *Cell Reports* 21(11):3256–3270.

98. Sade H, Baumgartner C, Hugenmatter A, Moessner E, Freskgård P-O, Niewoehner J (2014) A human blood-brain barrier transcytosis assay reveals antibody transcytosis influenced by pH-dependent receptor binding. *PLoS One* 9(4):e96340.

99. Couch JA, et al. (2013) Addressing safety liabilities of TfR bispecific antibodies that cross the blood-brain barrier. Sci Transl Med 5(183):183ra57.

100. Yu YJ, et al. (2014) Therapeutic bispecific antibodies cross the blood-brain barrier in nonhuman primates. *Sci Transl Med* 6(261):261ra154.

101. Wiley DT, Webster P, Gale A, Davis ME (2013) Transcytosis and brain uptake of transferrin-containing nanoparticles by tuning avidity to transferrin receptor. *Proceedings of the National Academy of Sciences USA* 110(21):8662–8667.

102. Kamaly N, Xiao Z, Valencia PM, Radovic-Moreno AF, Farokhzad OC (2012) Targeted polymeric therapeutic nanoparticles: design, development and clinical translation. *Chemical Society Reviews* 41(7):2971–3010.

103. Mellman I (1996) Endocytosis and molecular sorting. *Annual Review of Cell and Developmental Biology* 12:575–625.

104. Wang AZ, Langer R, Farokhzad OC (2012) Nanoparticle delivery of cancer drugs. *Annual Review of Medicine* 63:185–198.

105. Parveen S, Sahoo SK (2008) Polymeric nanoparticles for cancer therapy. *Journal of Drug Targeting* 16(2):108–123.

106. Zhang L, Gu FX, Chan JM, Wang AZ, Langer RS, Farokhzad OC (2008) Nanoparticles in medicine: therapeutic applications and developments. *Clinical Pharmacology and Therapeutics* 83(5):761–769.

107. Prabhu RH, Patravale VB, Joshi MD (2015) Polymeric nanoparticles for targeted treatment in oncology: current insights. *International Journal of Nanomedicine* 10:1001–1018.

108. Duncan R (2006) Polymer conjugates as anticancer nanomedicines. *Nature Reviews Cancer* 6(9):688–701.

109. Larson N, Ghandehari H (2012) Polymeric conjugates for drug delivery. *Chemistry of Materials* 24(5):840–853.

110. Dawidczyk CM, Kim C, Park JH, Russell LM, Lee KH, Pomper MG, Searson PC (2014) State-of-the-art in design rules for drug delivery platforms: lessons learned from FDA-approved nanomedicines. *Journal of Controlled Release* 187:133–144.

111. Davis, ME (2009) Design and development of IT-101, a cyclodextrin-containing polymer conjugate of camptothecin. *Advanced Drug Delivery Reviews* 61(13):1189–1192.

112. Kamaly N, Fredman, G, Subramanian M, Gadde S, Pesic A, et al. (2013) Development and in vivo efficacy of targeted polymeric inflammation-resolving nanoparticles. *Proceedings of the National Academy of Sciences* 110(16):6506–6511.

113. Han H, Davis ME (2013) Targeted nanoparticles assembled via complexation of boronic-acid-containing targeting moieties to diol-containing polymers. *Bioconjugate Chemistry* 24(4):669–677.

114. Farokhzad OC, Cheng J, Teply BA, Sherifi I, Jon S, et al. (2006) Targeted nanoparticle-aptamer bioconjugates for cancer chemotherapy in vivo. *Proceedings of the National Academy of Sciences USA* 103(16):6315–6320.

115. Mahmoud EA, Sankaranarayanan J, Morachis JM, Kim G, Almutairi A (2011) Inflammation responsive logic gate nanoparticles for the delivery of proteins. *Bioconjugate Chemistry* 22(7):1416–1421.

116. Shao W, Miao K, Liu H, Ye C, Du J, Zhao Y (2013) Acid and reduction dually cleavable amphiphilic comb-like copolymer micelles for controlled drug delivery. *Polymer Chemistry* 4(11):3398.

117. Eliasof S, Lazarus D, Peters CG (2013) Correlating preclinical animal studies and human clinical trials of a multifunctional, polymeric nanoparticle. *Proceedings of the National Academy of Sciences* 110(37):15127–15132.

118. Gao W, Langer R, Farokhzad OC (2010) Poly(ethylene glycol) with observable shedding. *Angewandte Chemie International Edition* 49(37):6567–6571.

119. Paramonov SE, Bachelder EM, Beaudette TT, Standley SM, Lee CC, et al. (2008) Fully acid-degradable biocompatible polyacetal microparticles for drug delivery. *Bioconjugate Chemistry* 19(4):911–919.

120. Gao W, Chan JM, Farokhzad OC (2010) pH-responsive nanoparticles for drug delivery. *Molecular Pharmaceutics* 7(6):1913–1920.

121. Fishman JB, Rubin JB, Handrahan JV, Connor JR, Fine RE (1987) Receptor-mediated transcytosis of transferrin across the blood brain barrier. *Journal of Neuroscience Research* 18(2):299–304.

Chapter II

DEVELOPMENT OF MOUSE MODEL THAT REPLICATES THE METASTASIS PROCESS IN HER2-POSITIVE BREAST CANCER BRAIN METASTASIS PATIENTS*

*Excerpts from this chapter are reprinted from Wyatt EA, Davis ME (2018) Method of establishing breast cancer brain metastases affects brain uptake of targeted, therapeutic nanoparticles. *Bioengineering and Translational Medicine* 1–8 with permissions from *Bioeng Transl Med*.

2.1 Introduction

2.1.1 HER2-positive breast cancer brain metastasis

Human epidermal growth factor receptor 2 (HER2) protein overexpression is observed in about 25% of human breast cancers. It confers a more aggressive phenotype and, historically, has been associated with poor patient prognosis (1). HER2-targeted therapies, such as the anti-HER2 antibody (Ab) trastuzumab, have improved outcomes in patients with HER2-positive, metastatic disease. However, with improved control of systemic disease and prolonged survival, the incidence of brain metastases is increasing in these patients (2,3). Currently, as many as half of patients with HER2-positive, metastatic breast cancer develop brain metastases over time (4). Treatment of these brain tumors is a growing clinical challenge, in large part due to the poor penetration of HER2-targeted agents through the blood-brain barrier (BBB) (4).

2.1.2 The BBB/BTB debate

There is considerable debate in the literature regarding the extent to which the BBB remains intact with brain metastases (in the form of the blood-tumor barrier (BTB)). Contrast agents show enhanced uptake in brain metastases, but chemotherapy has been generally ineffective in the clinic (5). Recent studies in experimental brain metastasis models reveal that, although the majority of metastases have some increased vascular permeability, their uptake of chemotherapeutics is limited (6). Furthermore, significant heterogeneity in therapeutic uptake is observed in brain metastases resected from patients, both among patients and within individual lesions (7). Additionally, an investigation of breast cancer subtypes showed that there is no significant disruption of the barrier by brain metastases resected from patients with HER2-positive breast cancer (8). Thus, while brain metastases may have some increased permeability, approaches to overcome limited drug delivery to the brain will be important to improve clinical outcomes, particularly for HER2-positive, metastatic disease.

2.1.3 Animal models of breast cancer brain metastasis

Mouse models of breast cancer brain metastasis are needed to both identify the biological mechanisms that contribute to the disease pathogenesis as well as to evaluate potential treatment strategies (9), including investigation of new approaches to increase the brain penetration of therapeutic agents. One of the most widely used methods to study breast cancer brain metastasis involves direct injection of human breast cancer cells into the mouse brain parenchyma (Fig. 2.1A). This intracranial (IC) model provides important insight into specific molecular events and pathways associated with tumor progression, as well as the utility of particular combination therapies (10, 11). However, because antitumor response to non-BBB-penetrant therapeutics has been observed in this model (10,11), we hypothesized that this method of establishing breast cancer brain metastases may not provide a clinically relevant, impermeable BBB/BTB to traditional therapeutic agents, thus limiting its usefulness for our investigation of nanoparticle delivery across the BBB/BTB to breast cancer brain metastases.

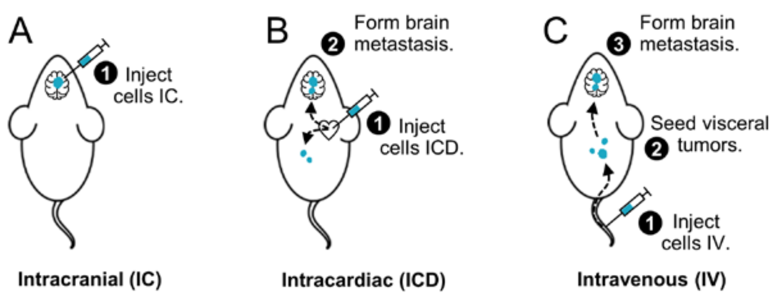

Fig. 2.1. Illustration of breast cancer brain metastasis models. (**A**) Intracranial (IC) injection of tumor cells allows for direct establishment of brain metastases. (**B**) Following intracardiac (ICD) injection into the left ventricle, tumor cells can head to brain vasculature, as well as to other organs. Some cells will successfully extravasate and form macroscopic brain tumors. (**C**) After intravenous (IV) injection, most tumor cells will arrest in the lung capillary bed, as well as other sites, followed by subsequent metastasis to the brain.

The preclinical study of fully metastatic breast cancer brain metastases in murine models has been limited by the fact that, in most cases, human breast cancer cell lines derived from metastatic tumors fail to consistently metastasize in immunodeficient mice, such as nude mice (12-14). Furthermore, tumor foci only occasionally form in the brain, limiting the practicality of this approach. Recently, it has been shown that modifications to the experimental conditions can increase the propensity of breast cancer cells to metastasize to the brain in mice, such as using special injection routes (e.g. intracardiac

(ICD), Fig. 2.1B) or developing cell variants with specific organ tropism (e.g. brain-tropic metastatic breast cancer cells) (15-17). However, such modifications can give rise to preclinical models that are further removed from clinical relevance and lack critical aspects of the human disease. For example, although brain metastases are most commonly observed among HER2-positive metastatic breast cancer patients, the majority of preclinical studies are based on established “brain-seeking” breast cancer cell lines that are HER2-negative, particularly brain-colonizing sublines of the human MDA-MB-231 breast cancer cell line (18,19).

As an alternative to manipulating human-derived breast cancer cells lines, a more permissive host can be used that may allow for improved metastatic dissemination. Evidence suggests that natural killer (NK) cells play a critical role in preventing metastatic spread of tumor cells in classical nude mice (20). Pretreatment of nude mice with NK-depleting antibodies was initially investigated as a potential solution to allow for metastatic dissemination of cancer cells (21); however, this only provided a narrow temporal window of inhibited NK activity that was not sufficient for lengthier studies of metastasis, such as dissemination from local tumors. Recently, Rag2$^{-/-}$;Il2rg$^{-/-}$ mice that lack B, T, and NK cells (22) have shown the ability to permit the systemic spread of several human cancer cell types without the need for additional modification of the cancer cells (cite sarcoma and breast papers) (21,23).

Here, we present a new murine model for HER2-positive breast cancer brain metastasis that involves intravenous (IV) injection of breast cancer cells in Rag2$^{-/-}$;Il2rg$^{-/-}$ mice (Fig. 2.1C). This new model developed here establishes brain metastases by methods that more closely resemble the human disease, forming whole-body tumors that eventually metastasize to the brain. Our results suggest that IV-formed brain tumors maintain a more intact BBB/BTB than those established by IC injection, enabling future studies that investigate new strategies to increase brain uptake of therapeutics.

2.2 Results and discussion

2.2.1 Rag2$^{-/-}$; Il2rg$^{-/-}$ mice are permissive to brain metastasis following IV injection of HER2-positive BT474-Gluc breast cancer cells

In an attempt to create a clinically representative, impermeable barrier to standard therapeutics, we developed a new model of HER2-positive breast cancer brain metastasis that reproduces human cancer dissemination. HER2-positive BT474-Gluc cells were IV injected into Rag2$^{-/-}$;Il2rg$^{-/-}$ mice, and formation of brain metastases was monitored by MRI. This cell line was engineered to express cerulean fluorescent protein (CFP) and Gaussia luciferase (Gluc) that can be used as a surrogate for tumor burden (24). Rag2$^{-/-}$; Il2rg$^{-/-}$ mice were chosen because they have shown the ability to allow multi-organ metastatic spread of HER2-positive breast cancer cell lines injected IV (23).

After IV injection, BT474-Gluc brain tumors developed in a majority of the mice (> 90%) before they succumbed to visceral tumor burden, with a distribution similar to that observed in patients (Fig. 2.2). The median time to establishment of brain metastatic tumors visible by MRI was 4.2 months (range 2.9 – 6.1 months).

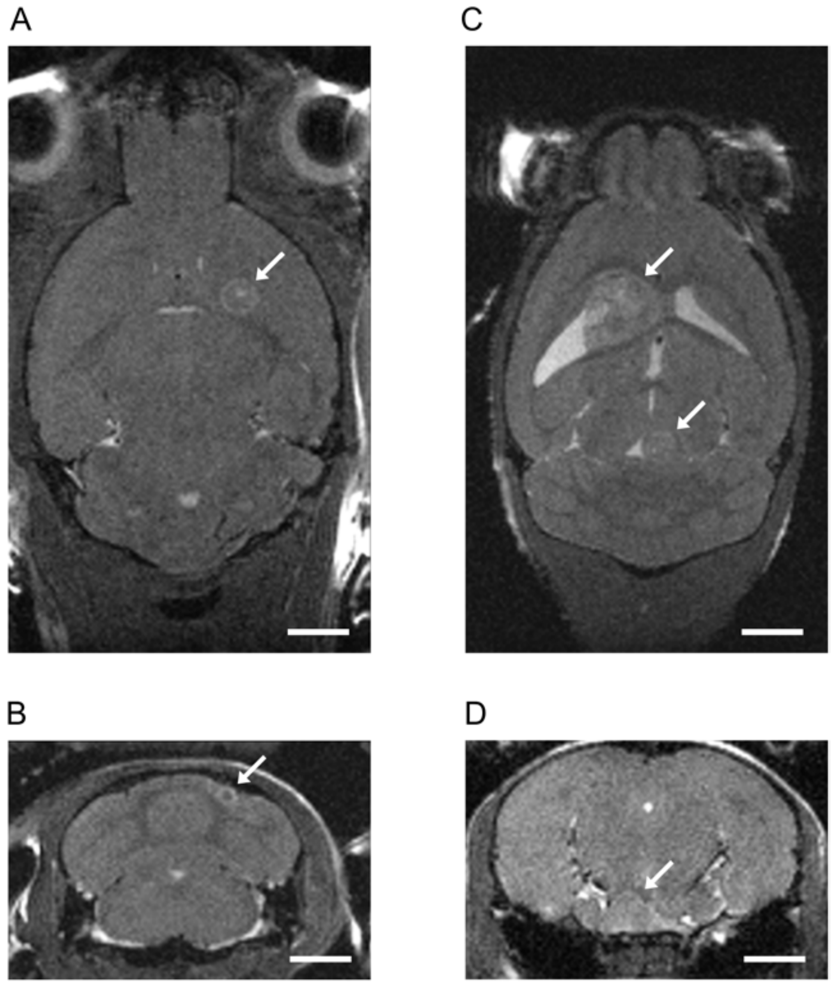

Fig. 2.2. Metastatic brain tumors imaged by MRI following IV injection of BT474-Gluc cells. Intracerebral (**A**,**B**,**C**) and leptomeningeal metastases were detected (**D**). Most intracerebral metastases were located in the cerebrum (**A**), with occasional metastases in the cerebellum (**B**). Multifocal metastases were occasionally observed (**C**). Leptomeningeal metastases most commonly grew in the subarachnoid space (**D**). Scale bar, 2 mm.

2.2.2 Brain tumors display differential morphology and response to standard HER2-targeted therapy when established by IV versus IC method

We compared BT474-Gluc brain metastatic tumors established by the IV method versus the standard IC method in Rag2$^{-/-}$;Il2rg$^{-/-}$ mice. After IV or IC injection of BT474-Gluc cells, formation of brain metastatic tumors was monitored by MRI. Interestingly, when compared to IC-formed metastases, brain tumors established by IV injection displayed more uniform MRI contrast and an increased invasive phenotype by infiltrating rather than displacing neighboring brain regions (Fig. 2.3). Furthermore, a marked increase in necrotic fraction of the tumor tissue was observed for tumors established by IC injection relative to IV injection.

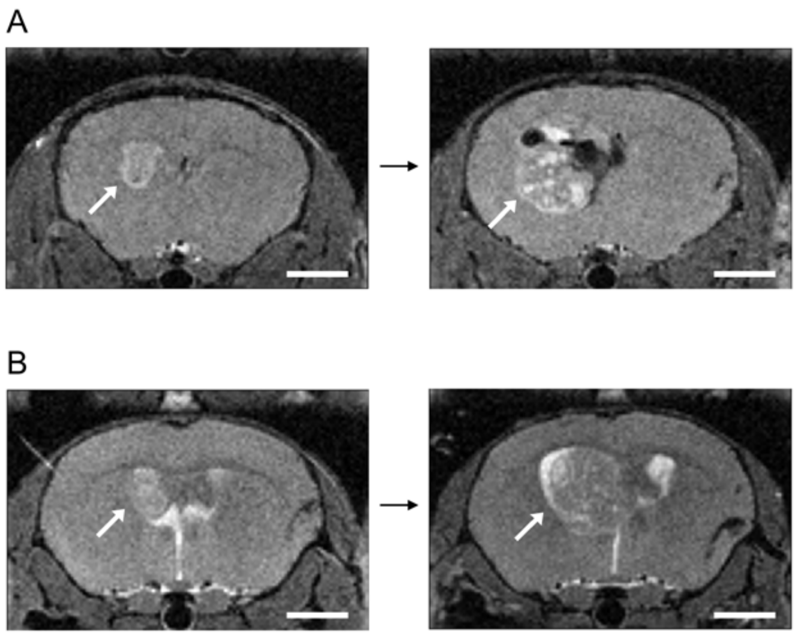

Fig. 2.3. Growth of BT474-Gluc metastatic brain tumors when established by IC and IV injection of breast cancer cells, as monitored by MRI. (**A**) IC-formed brain tumors. (**B**) IV-formed brain tumors. Scale bar, 2 mm.

Additionally, we examined the vasculature in BT474-Gluc brain metastatic tumor tissue following IV- and IC-establishment. 1 mm-thick tissue sections of brain tumor and healthy brain tissue were prepared using the CLARITY method for clearing large tissue volumes (25). Tissue samples were nuclear stained with DAPI as well as immunostained with an antibody against CD31, and imaged using confocal microscopy. In both tumor models, imaging studies revealed marked abnormality and significant increase in diameter of the tumor vasculature relative to healthy brain vasculature (Fig. 2.4). These observations are consistent with previous reports that suggest perivascular growth of HER2-positive breast cancer brain metastases is angiogenic (26). Tumor vasculature in IC-formed brain tumors was more irregular (e.g. forming abnormal loops), as compared to that in IV-formed brain tumors that showed more regular branching.

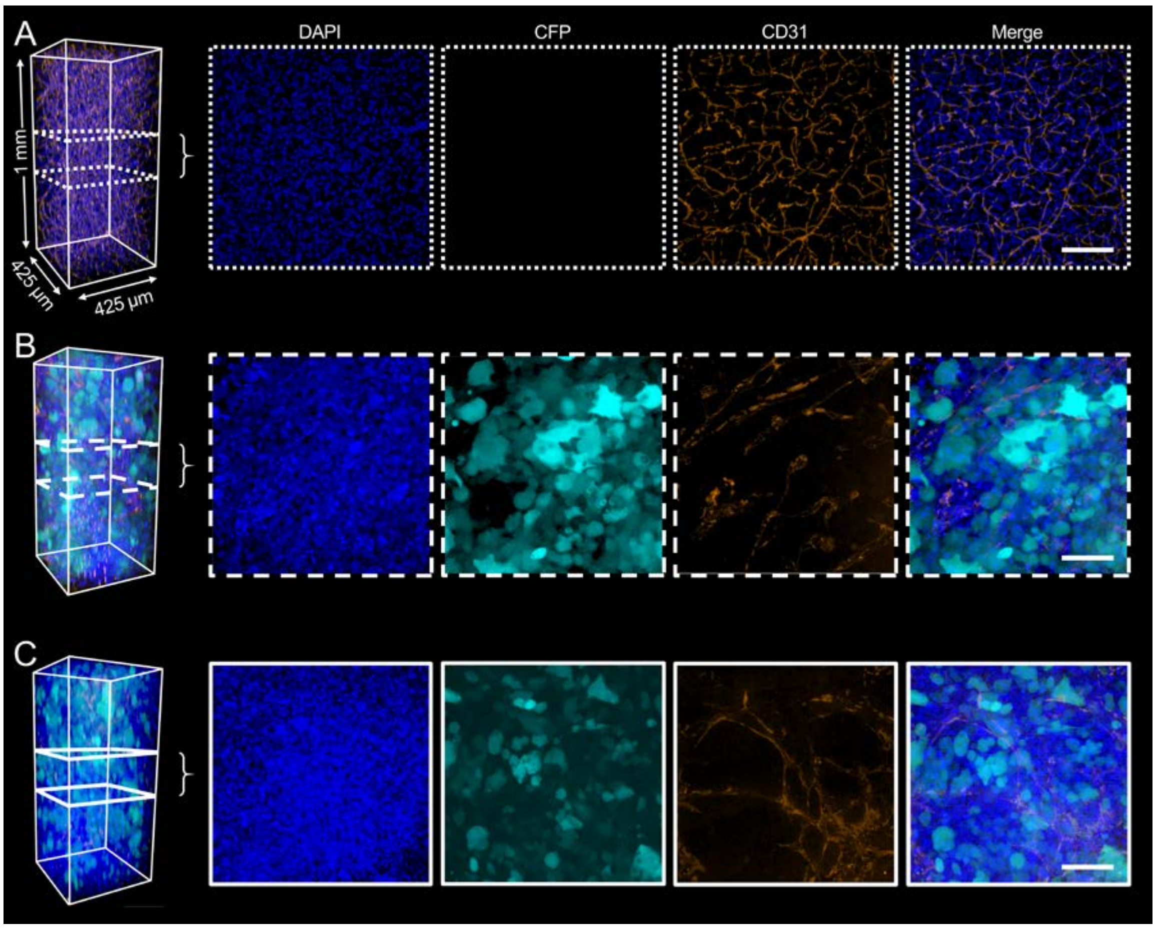

Fig. 2.4. Confocal images of CLARITY processed Rag2$^{-/-}$;Il2rg$^{-/-}$ healthy and tumor brain vasculature. Provided are representative volume renderings (left) and 200 µm thick maximum intensity projections (MIPs) centered at 500 µm depth (right) for healthy brain tissue (**A**), IC-formed brain tumor tissue (**B**) and IV-formed brain tumor tissue (**C**). In addition to endogenous tumor marker (CFP), tissue was nuclear stained (DAPI) as well as vascular immunostained (CD31). Scale bar, 100 µm.

Most importantly, we tested the effects of a standard anti-HER2 therapy, trastuzumab, on the growth of BT474-Gluc tumors established by IV injection versus the commonly used IC method. Trastuzumab at 5 mg/kg was administered twice weekly via intravenous tail vein injection, and treatment was initiated when tumors reached 10 mm^3 in volume. MRI was used to monitor brain tumor size and response to therapy. Treatment with trastuzumab led to delay in tumor progression when tumors were established by IC injection, suggesting this method of forming brain tumors may disrupt the BBB/BTB (Fig. 2.5). In contrast, trastuzumab failed to control tumor growth for tumors established IV, mimicking the clinical situation. Similarly, treatment with lapatinib did not slow tumor progression for IV-formed tumors.

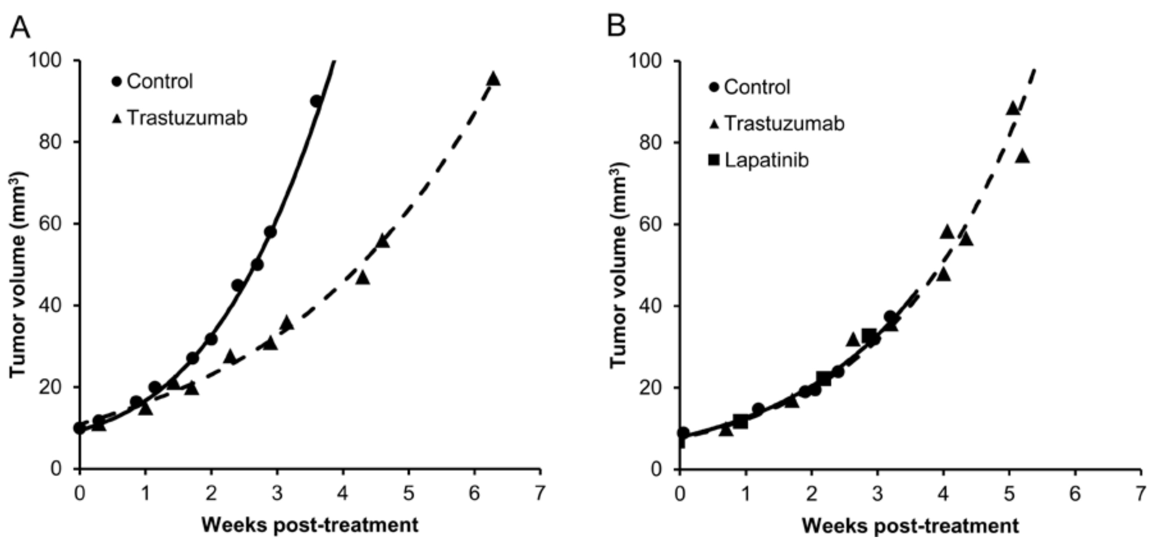

Fig. 2.5. Effect of anti-HER2 therapy on HER2-positive BT474-Gluc breast cancer brain metastases established in $Rag2^{-/-}$;$Il2rg^{-/-}$ mice. Tumors established by IC injection (**A**) showed significant delay in tumor progression, whereas those established by IV injection (**B**) did not. Data shown are 4 mice per treatment group for the IC model, and 8, 12 and 2 mice for saline, trastuzumab and lapatinib groups, respectively, for the IV model.

2.2.3 IV model of HER2-positive breast cancer brain metastasis reproduces metastatic pattern observed in patients

To assess the metastatic spread of BT474-Gluc breast cancer cells in Rag2$^{-/-}$; Il2rg$^{-/-}$ mice following IV injection, all organs were collected for analysis and metastases were identified using a number of methods. A hematoxylin and eosin (H&E) stain was performed first on thin-fixed tissue samples to identify potential tumor foci (Fig. 2.6A). Subsequently, BT474-Gluc metastases were confirmed using two methods, including: (i) immunohistochemistry by staining for HER2 overexpression, and (ii) confocal microscopy by presence of tumor-associated CFP (Fig. 2.6B and C). CLARITY was also performed to assess tumor burden in large volumes of tissue (Fig. 2.6D). Notably, IV injection of BT474-Gluc cells reproduced the full metastatic pattern observed in breast cancer patients, with multiple metastatic sites including brain, lung, bone, liver, ovary and lymph tissues among others (Table 2.1).

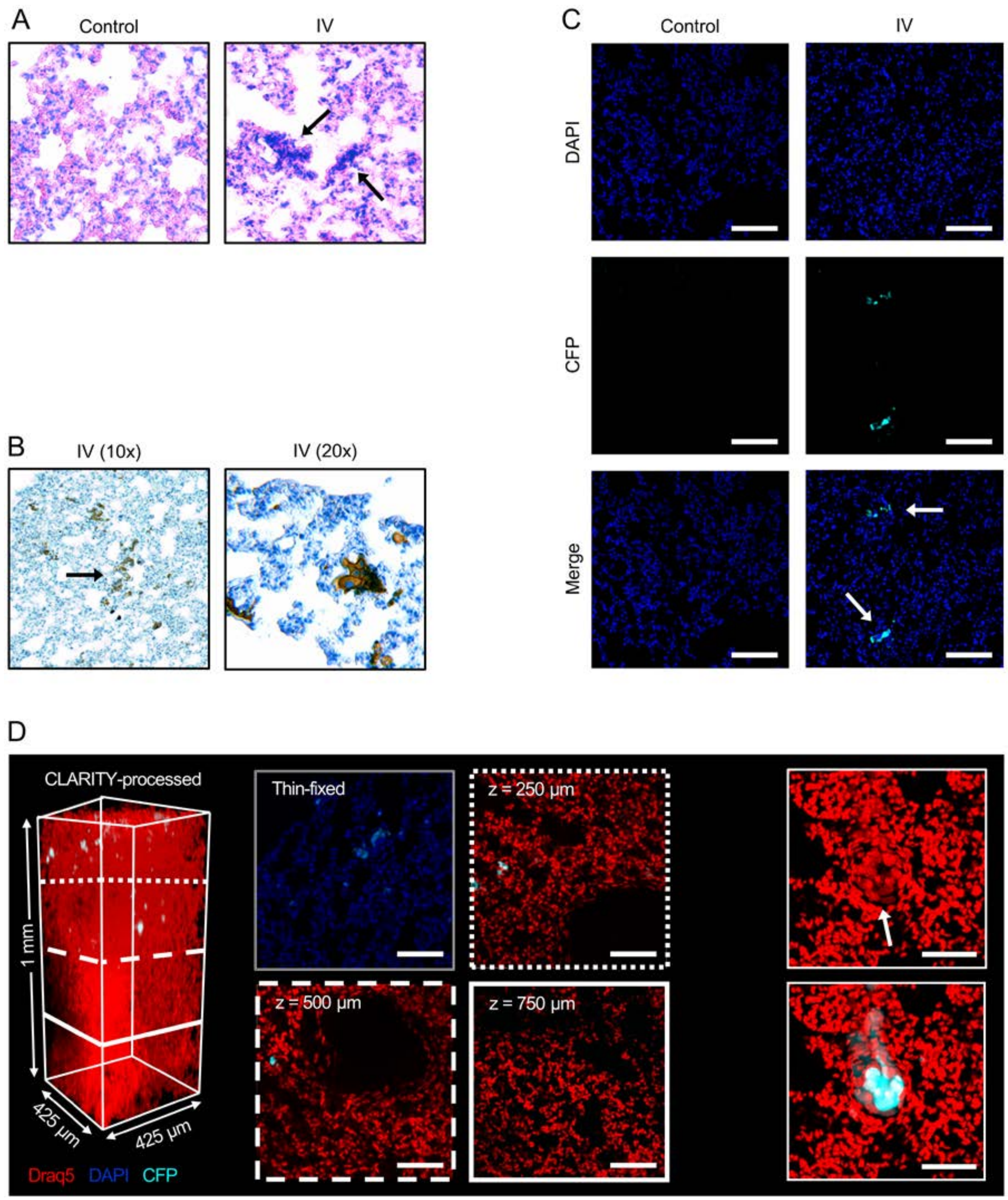

Fig. 2.6. Metastasis identification in Rag2$^{-/-}$;Il2rg$^{-/-}$ mice following IV injection of BT474-Gluc breast cancer cells. Thin-fixed tissue sections were analyzed by H&E histology (**A**), HER2 immunohistochemistry (**B**), and confocal microscopy (**C**). Large tissue volumes were CLARITY processed, nuclear stained (Draq5) and imaged by confocal microscopy (**D**). Provided are a full volume rendering and 200 µm thick MIPs compared to a thin-fixed section (left), and higher magnification of an individual metastasis (right). The results shown here for lung tissue are indicative of the observations in the other tissue types. Scale bar, 100 µm.

Brain	Lung	Bone	Liver	Ovary	Lymph	Other*
22/24	24/24	6/8	16/17	24/24	24/24	19/24

Table 2.1. Metastatic ability of human BT474-Gluc breast cancer cells in Rag2$^{-/-}$;Il2rg$^{-/-}$ mice following IV injection. Metastasis incidence provided by site per number of mice for which tissue type was analyzed. *Other metastatic sites included kidney, salivary glands, and interscapular space.

2.3 Conclusions

Here, we describe a new preclinical model of human HER2-positive breast cancer brain metastasis based on an immunodeficient Rag2$^{-/-}$;Il2rg$^{-/-}$ mouse that lacks B, T, and NK cell activity. This more permissive host enabled complete, multiorgan metastatic spread of HER2-positive BT474-Gluc human breast cancer cells, without the need for selections or additional modifications to the system. Importantly, BT474-Gluc cells injected intravenously consistently metastasized to the brain, allowing the study of brain metastatic tumors before the mice succumbed to systemic tumor burden. Additionally, we show that brain metastases formed by IV injection of breast cancer cells differ from those established by the commonly used IC method. We observed a significant antitumor response to a standard anti-HER2 agent in brain tumors that were formed by IC injection of human breast cancer cells. In contrast, the HER2-inhibitor failed to control tumor growth in metastases established by the IV method, replicating the clinical situation.

After our development work was completed, the model that uses an ICD injection to establish brain metastases gained popularity in the literature. Thus, we included both commonly used models from the literature in addition to our new model here to investigate the efficacy and brain penetration of targeted, therapeutic nanoparticles.

2.4 Materials and methods

IC and IV Brain Metastasis Models. All animals were treated according to the NIH guidelines for animal care and use as approved by the Caltech Institutional Animal Care and Use Committee (27). BT474-Gluc cells, transduced with an expression cassette encoding Gluc and CFP separated by an internal ribosomal entry site using a lentiviral vector, were obtained from Dr. Jain at Harvard University. BT474-Gluc cells were maintained in RPMI 1640 supplemented with 10% (v/v) FBS in a humidified oven at 37°C with 5% CO_2. For the IC model, 50,000 BT474-Gluc cells in 2 µL RPMI were intracranially injected into the right cerebral hemisphere of female Rag2$^{-/-}$;Il2rg$^{-/-}$ mice (Jackson Laboratory) using a stereotaxic apparatus at a rate of 0.1 µL/min. The coordinates for injection were 2 mm posterior, 1.5 mm lateral to bregma, and 2.5 mm depth from bregma. For the IV model, 2 M cells were suspended in 150 µL RPMI and slowly injected into the lateral tail vein of restrained female Rag2$^{-/-}$;Il2rg$^{-/-}$ mice.

Tumor Size Monitoring. For the IV model, formation of BT474-Gluc brain metastatic tumors was monitored by MRI on a 11.7-T magnet every few weeks until macroscopic tumors were visible (~0.2 mm^3 in volume). Tumor growth was then monitored by MRI approximately weekly, as for the IC model. Mice were anaesthetized with 1.5–2% (v/v) isoflurane in O_2 at a flow rate of 1–1.5 mL/min. T2-weighted 3D RARE images were acquired to assess the tumor volume. The image acquisition parameters were as follows: echo time: 6.1 ms; repetition time: 250 ms; rapid acquisition relaxation enhanced (RARE) factor: 4; number of averages: 4; field of view: 2.0 cm x 1.2 cm x 0.8 cm; matrix: 200 x

120 x 80 (100 µm isotropic resolution). Tumor volume was determined manually from the T2 hyperintense tumor regions of the brain using Fiji software.

Treatments. Treatment began when brain metastatic tumors reached ~10 mm^3, as measured by MRI. Mice in the IC model were randomized into two groups of four mice per group. Mice in the IV model were randomized into two groups of 8 and 12 mice for the saline and Herceptin groups, respectively. Herceptin at 5 mg/kg was freshly prepared in PBS, pH 7.4. The control treatment was 0.9% (w/v) saline. The different formulations were systemically administered by lateral tail vein injection twice weekly with injections were standardized to 150 µL per 20 g body weight. Lapatinib was dissolved at 10 mg/mL in sterile water with 0.5% Tween 80 (Sigma) and administered at 100 mg/kg daily by oral gavage.

Tissue Processing. Mice were sacrificed following signs of prolonged distress or loss of >20% body weight. The mice were anaesthetized and transcardially perfused with a 10% sucrose solution, followed by a 4% (v/v) formaldehyde in PBS, pH 7.4. All organs were collected for analysis. The freshly collected tissues were post-fixed in 4% (v/v) formaldehyde in PBS, pH 7.4 overnight at 4 °C, then washed in PBS, pH 7.4 with 0.02% NaN_3 to remove excess fixative. Individual tissues were dehydrated in increasing concentrations of ethanol (3 x 30 min each for 50, 70, 95 and 100% EtOH), followed by xylenes (3 x 30 min) and 50:50 xylene:paraffin mixture (1 x 30 min). The tissues were then incubated in molten paraffin (3 x 1 h) at 60 °C, then placed in a paraffin mold and stored at 4 °C until sectioning. A Leica 1512 microtome was used to cut 5 µm sections. Slides were stored at 4 °C, protected from light until time for further processing.

H&E Histology. Paraffin-embedded sections were deparaffinized in xylenes, rehydrated using decreasing concentrations of ethanol and washed in pure water (3 x 1 min). Sections were stained in hematoxylin for 5 min, dipped in acidic EtOH, incubated in bluing agent (0.2% (v/v) ammonium hydroxide in water) for 2 min, and stained in eosin for 1 min with 30 sec rinses in tap water between incubation steps. They were then dehydrated with increasing concentration of ethanol and xylenes. Tissues were mounted using Permount (Fisher) and images acquired on an Olympus IX50 microscope using a 10x CPlan objective and QCapture Pro 6 imaging software (QImaging).

HER2 Tumor Biomarker Immunohistochemistry. Paraffin-embedded sections were deparaffinized in xylenes, rehydrated using decreasing concentrations of ethanol, and washed in pure water (3 x 1 min). Epitope retrieval was performed by baking the tissues at 90-95°C in 10 mM citrate buffer, pH 6.0 for 40 min. The tissues were cooled for 20 min, then washed in PBST, endogenous peroxidase quenched with a 3% (v/v) hydrogen peroxide for 5 min, and rinsed again with PBST (2 x 5 min). For HER2 identification, tissues were incubated with a 1:100 dilution of an anti-human HER2 rabbit primary Ab (Dako A0485) in PBST for 1 h at room temperature, washed with PBST (2 x 5 min), followed by incubation with a 1:100 of a HRP-conjugated anti-rabbit goat secondary Ab (Abcam ab97051) in PBST for 1 h at room temperature, and finally washed with PBST (2 x 5 min). Tissues sections were then developed with a DAB solution (Thermo Scientific) for 5 min at room temperature, rinsed with PBST (2 x 3 min), followed by counterstaining with hematoxylin for 2 min. Sections containing no primary Ab stain as well as no tumor were processed simultaneously and used as negative controls while samples known to strongly express HER2 served as positive controls. Tissues were mounted using Prolong Gold antifade reagent and images acquired on an Olympus IX50 microscope using a 10x CPlan objective and QCapture Pro 6 imaging software (QImaging).

CLARITY. Excised tissue was post-fixed in 4% (v/v) formaldehyde in PBS, pH 7.4 overnight at 4 °C, then washed in PBS, pH 7.4 with 0.02% NaN_3 to remove excess fixative. Tissue was sectioned on a vibratome to a thickness of 1 mm, and stored at 4 °C, protected from light until further processing. Tissues were incubated in A4P0 hydrogel monomer solution (4% acrylamide in PBS, pH 7.4) overnight with shaking (acrylamide solution, Bio-Rad; thermal initiator, Wako). Samples were degassed, then polymerized in a 37 °C incubator for 3 h. Following polymerization, samples were washed in PBS, pH 7.4 to remove residual hydrogel, then cleared at 37 °C with gentle agitation in 8% (w/v) SDS with 0.02% NaN_3 in PBS, pH 8.0 until optically transparent. Clearing times varied for tissue types. Samples were washed in PBS, pH 7.4 with 0.02% NaN_3 for 2 days with minimum of four exchanges. Nuclear stained tissues were incubated in either a 1 μg/mL dilution of DAPI (Life Technologies) or a 1:1000 dilution of Draq5 (Cell Signaling) with 0.02% NaN_3 in PBST for 2 days with shaking, then washed in PBS, pH 7.4 with 0.02% NaN_3 for 2 days with a minimum of four exchanges.

For vasculature identification, brain samples were incubated with a 1:200 dilution of an anti-CD31 rabbit primary Ab (Abcam ab28364) and a 1:200 dilution of an AlexaFlor 594-conjugated anti-rabbit donkey secondary Ab (Jackson ImmunoResearch 711-585-152) with 0.02% NaN_3 in PBST for 7 days each with shaking to visualize vasculature. Draq5 nuclear stain, as above, was added to secondary Ab cocktail. Immunostains were replaced every one-two days with fresh cocktail, and tissues were washed for two days with a minimum of four exchanges in PBST with 0.02% NaN_3 between stains and after final stain. Samples were incubated in RIMS (prepared with Histodenz, Sigma-Aldrich, RI = 1.46) with gentle agitation for one day. Glass slides were prepared with 1 mm iSpacers (SunJin Lab Co.). Samples were placed inside the spacer, followed by slight overfill of fresh RIMS, and a coverslip.

Z-stacks were acquired with a Zeiss LSM 710 confocal microscope using an Achroplan 20 / 0.5 NA water objective with ~40-50% overlap. Linear laser power z-correction was applied in Zen software (Zeiss) to ensure uniform signal intensity throughout the sample, as even cleared tissue will scatter at depth. For comparative analysis between samples, all laser and gain settings were set at the beginning of imaging and were unchanged. Image analysis was performed with Imaris (Bitplane).

2.5 References

1. Slamon DJ, et al. (1987) Human breast cancer: Correlation of relapse and survival with amplification of the HER-2/neu oncogene. *Science* 235(4785):177–182.

2. Lin NU, Winer EP (2007) Brain metastases: The HER2 paradigm. *Clinical Cancer Research* 13(6):1648–1655.

3. Chien AJ, Rugo HS (2013) Emerging treatment options for the management of brain metastases in patients with HER2-positive metastatic breast cancer. *Breast Cancer Research and Treatment* 137(1):1–12.

4. Ramakrishna N, et al. (2014) Recommendations on disease management for patients with advanced human epidermal growth factor receptor 2-positive breast cancer and brain metastases: American Society of Clinical Oncology clinical practice guideline. *Journal of Clinical Oncology* 32(19):2100–2108.

5. Steeg PS, Camphausen KA, Smith QR (2011) Brain metastases as preventive and therapeutic targets. *Nature Reviews Cancer* 11(5):352–363.

6. Lockman PR, et al. (2010) Heterogeneous blood-tumor barrier permeability determines drug efficacy in experimental brain metastases of breast cancer. *Clinical Cancer Research* 16(23):5664–5678.

7. Morikawa A, et al. (2015) Capecitabine and lapatinib uptake in surgically resected brain metastases from metastatic breast cancer patients: a prospective study. *Neuro-Oncology* 17(2):289–295.

8. Yonemori K, et al. (2010) Disruption of the blood brain barrier by brain metastases of triple-negative and basal-type breast cancer but not HER2/neu-positive breast cancer. *Cancer* 116(2):302–308.

9. Clarke R (1996) Animal models of breast cancer: Their diversity and role in biomedical research. *Breast Cancer Research and Treatment* 39(1):1–6.

10. Kodack DP, Chung E, Yamashita H, Incio J, Duyverman AMMJ, et al. (2012) Combined targeting of HER2 and VEGFR2 for effective treatment of *HER2*-amplified breast cancer brain metastases. *Proceedings of the National Academy of Sciences USA* 109(45):E3119–E3127.

11. Ni J, Ramkissoon SH, Xie S, Goel S, Stover DG, et al. (2016) Combination inhibition of PI3K and mTORC1 yields durable remissions in mice bearing orthotopic patient-derived xenografts of HER2-positive breast cancer brain metastases. *Nature Medicine* 22(7):723–726.

12. Price JE (1996) Metastasis from human breast cancer cell lines. *Breast Cancer Research Treatment* 39(1):93–102.

13. Lacroix M, Leclercq G (2004) Relevance of breast cancer cell lines as models for breast tumours: an update. *Breast Cancer Research Treatment* 83(3):249–289.

14. Bos PD, Nguyen DX, Massagué J (2010) Modeling metastasis in the mouse. *Current Opinion in Pharmacology* 10(5):571–577.

15. Bos PD, Zhang XH, Nadal C, Shu W, Gomis RR, et al. (2009) Genes that mediate breast cancer metastasis to the brain. *Nature* 459(7249):1005–1009.

16. Francia G, Cruz-Munoz W, Man S, Xu P, Kerbel RS (2011) Mouse models of advanced spontaneous metastasis for experimental therapeutics. *Nature Reviews Cancer* 11(2):135–141.

17. Martínez-Aranda A, Hernández V, Picón C, Modolell I, Sierra A (2013) Development of a preclinical therapeutic model of human brain metastasis with chemoradiotherapy. *International Journal of Molecular Sciences* 14(4):8306–8327.

18. Kim LS, Huang S, Lu W, Lev DC, Price JE (2004) Vascular endothelial growth factor expression promotes the growth of breast cancer brain metastases in nude mice. *Clinical and Experimental Metastasis* 21(2):107–118.

19. Palmieri D, Chambers AF, Felding-Habermann B, Huang S, Steeg PS (2007) The biology of metastasis to a sanctuary site. *Clinical Cancer Research* 13(6):1656–1662.

20. Hanna N, Burton RC (1981) Definitive evidence that natural killer (NK) cells inhibit experimental tumor metastases in vivo. *The Journal of Immunology* 127(5):1754–1758.

21. Nanni P, Nicoletti G, Landuzzi L, Croci S, Murgo A, et al. (2010) High metastatic efficiency of human sarcoma cells in Rag2/gammac double knockout mice provides a powerful test system for antimetastatic targeted therapy. *European Journal of Cancer* 46(3):659–668.

22. Traggiai E, Chicha L, Mazzucchelli L, Bronz L, Piffaretti JC, et al. (2004) Development of a human adaptive immune system in cord blood cell-transplanted mice. *Science* 304(5667):104–107.

23. Nanni P, et al. (2012) Multiorgan metastasis of human HER-2^{+} breast cancer in Rag2$^{-/-}$;Il2rg$^{-/-}$ mice and treatment with PI3K inhibitor. *PLoS One* 7(6):e39626.

24. Chung E, et al. (2009) Secreted Gaussia luciferase as a biomarker for monitoring tumor progression and treatment response of systemic metastases. *PLoS One* 4(12):e8316.

25. Treweek JB, Chan KY, Flytzanis NC, Yang B, Deverman BE, et al. (2015) Whole-body tissue stabilization and selective extractions via tissue-hydrogel hybrids for high-resolution intact circuit mapping and phenotyping. *Nature Protocols* 10(11):1860–1896.

26. Kienast Y, von Baumgarten L, Fuhrmann M, Klinkert WE, Goldbrunner R, et al. (2010) Real-time imaging reveals the single steps of brain metastasis formation. *Nature Medicine* 16(1):116–122.

27. Committee on care and use of laboratory animals (1996) *Guide for the care and use of laboratory animals* (Natl Inst Health, Bethesda), DHHS Publ No (NIH) 85-23.

Chapter III

INVESTIGATION OF TARGETED, SINGLE-AGENT THERAPEUTIC NANOPARTICLES IN MOUSE MODELS OF BREAST CANCER BRAIN METASTASIS†

†Excerpts from this chapter are reprinted from Wyatt EA, Davis ME (2018) Method of establishing breast cancer brain metastases affects brain uptake of targeted, therapeutic nanoparticles. *Bioengineering and Translational Medicine* 1–8 with permissions from *Bioeng Transl Med*.

3.1 Introduction

3.1.1 Intracellular trafficking at the BBB

Of the many strategies to increase brain penetration of systemic therapeutics, perhaps one of the most promising is the use of receptor-mediated transcytosis (RMT) (1,2). Transferrin receptor (TfR) has been actively explored for RMT across the BBB, due to its high expression on BBB endothelium (3). In particular, anti-TfR antibodies (Abs) have garnered the most interest because of their ability to bind TfR with high affinity without interfering with endogenous transferrin (Tf) (4,5). Results from initial studies suggested that reducing the affinity of anti-TfR Abs to TfR maximizes their uptake into the brain parenchyma (6). Further investigation revealed that affinity influences intracellular trafficking; high-affinity anti-TfR Abs are trafficked to the lysosome, while lower-affinity variants are more capable of transcytosis (7). Recently, it has been shown that bivalent Ab:TfR binding leads to lysosomal sorting, whereas monovalent binding facilitates transcytosis (8). In addition to affinity and valency, *in vitro* results suggest that pH-sensitivity of TfR binding also affects trafficking of anti-TfR Abs; an Ab with reduced affinity at endosomal pH 5.5 showed a greater ability to transcytose than pH-independent Abs of comparable affinities at extracellular pH 7.4 (9). However, despite a more detailed understanding of the properties that promote transcytosis, several challenges exist in translating anti-TfR Abs into the clinic, including the need to: (i) dose very high quantities (5), (ii) mitigate effector-function driven safety concerns (10) and (iii) develop species-specific Abs (11).

Motivated by the results from anti-TfR Ab trafficking at the BBB, we began to investigate how fundamental properties of TfR-targeted nanoparticles affect their transcytosis capacity (12). Targeted nanoparticles were chosen for their ability to deliver large quantities and a variety of drugs to specific tissues at well-controlled release rates (13). In analogy to the results obtained with anti-TfR Abs, Tf-coated gold nanoparticles (AuNPs) with reduced avidity to TfR demonstrated the greatest ability to cross the BBB (12). Despite showing promise, questions regarding the need for very high systemic dosing to achieve sufficient brain accumulation led to alternative nanoparticle designs. Recently, an acid-cleavable targeting strategy was incorporated into nanoparticles to increase the ability of high-avidity nanoparticles to enter the brain (14). With this design, nanoparticles can bind TfR with high avidity on the blood side of the BBB to enable practical, systemic dosing, but shed the targeting ligands upon acidification during transcytosis (15), allowing free diffusion into the parenchyma (Fig. 3.1). Incorporation of an acid-cleavable linkage between Tf and the nanoparticle core increased brain uptake of high-avidity Tf-coated AuNPs nearly 3-fold (14). In contrast, no improvement was observed with high-affinity anti-TfR-coated AuNPs with the cleavable linker, consistent with their trafficking to the lysosome. These results suggest that intracellular trafficking may also be affected by the particular targeting ligand.

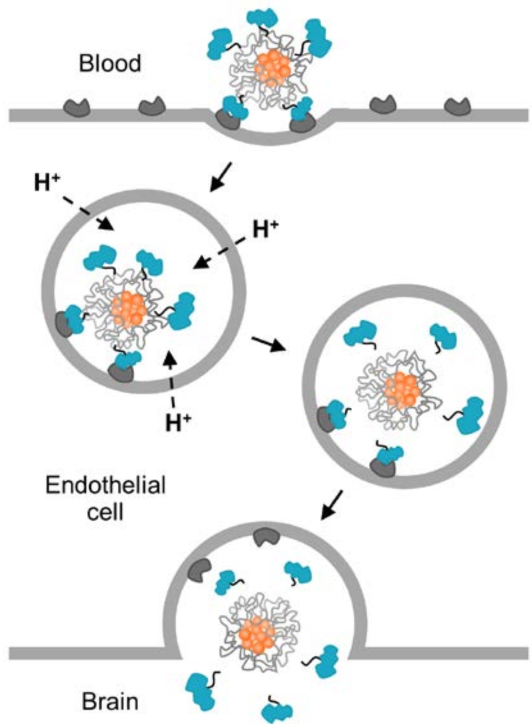

Fig. 3.1. Scheme of acid-cleavable targeting strategy. Following endocytosis, rapid acidification of endosome triggers separation of Tf ligands from the nanoparticle core, allowing free diffusion of the nanoparticle into the brain parenchyma after transcytosis.

3.1.2 Investigation of TfR-targeted, therapeutic nanoparticles in models of breast cancer brain metastasis

Here, we determine whether nanoparticles can be prepared to deliver therapeutic quantities of drug across the BBB. We focused on HER2-positive breast cancer brain metastasis because of the inadequate drug concentrations achieved in these tumors in the clinical setting. Although a number of preclinical models for this disease have emerged in the literature, the effect of the method used to establish metastatic brain tumors on therapeutic brain penetration has not been examined. To address these questions, we adapted a targeted nanoparticle delivery system for camptothecin (CPT) previously developed in our lab for its use at the BBB (16, 17). Tf was attached to nanoparticles consisting of a mucic acid polymer (MAP) conjugate of CPT (MAP-CPT) through a pH-dependent, boronic acid-diol complexation to form TfR-targeted MAP-CPT nanoparticles (Fig. 3.2). We investigated antitumor efficacy and brain uptake of these nanoparticles in two types of models from the literature, as well as a new, third model we developed that more fully mimics the metastasis process in patients. We found that this targeted nanoparticle delivery system can be used to deliver CPT to HER2-positive breast cancer brain metastases. Importantly, we also observed significant differences in efficacy as well as brain penetration of both TfR-targeted and non-targeted therapeutics between the models, showing that the method of establishing brain metastases can affect brain uptake of therapeutic agents.

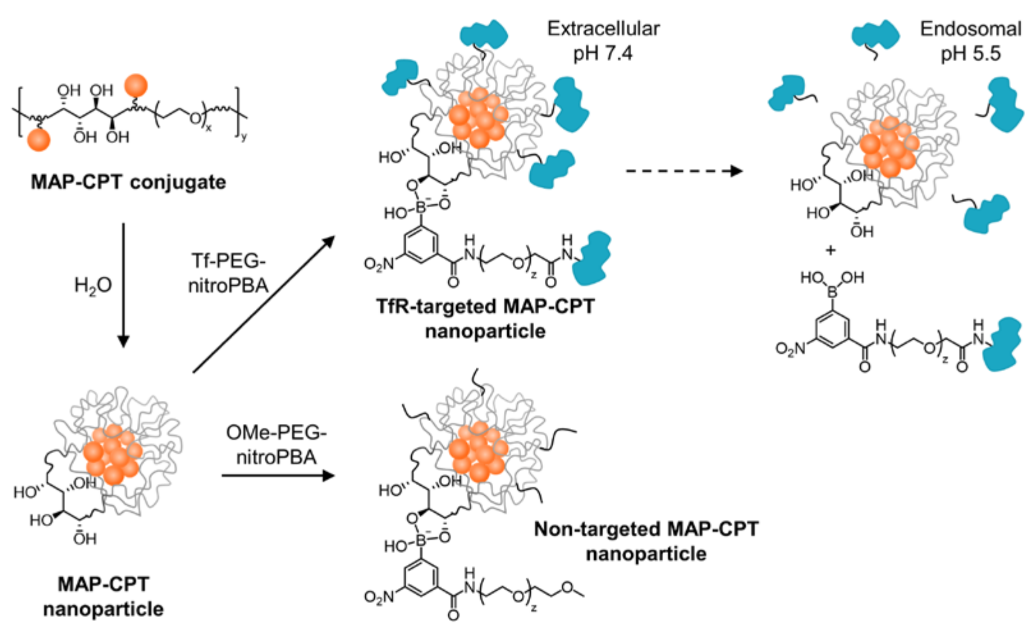

Fig. 3.2. Preparation of TfR-targeted and non-targeted MAP-CPT nanoparticles and pH-dependence of nitroPBA-diol complex. x ~ 82 for 3.4kDa PEG; y ~ 20 for material used in this study; z ~ 120 for 5kDa PEG.

3.2 Results

3.2.1 Synthesis and characterization of TfR-targeted and non-targeted MAP-CPT nanoparticles

MAP-CPT nanoparticles were chosen for this study because they retained the optimal design parameters identified in our previous AuNP formulations, including a sub-100-nm diameter and near-neutral zeta potential (12). It has also been shown that these characteristics facilitate the diffusion of nanoparticles through brain tissue (18). The ketal linker previously investigated as the acid-cleavable moiety between the Tf and the nanoparticle did not provide optimal cleavage kinetics to remove all surface Tf during transcytosis (14). The MAP delivery system allows for assembly of TfR-targeted nanoparticles using an improved acid-cleavable chemistry (Fig. 3.2), as discussed below. Furthermore, MAP-CPT nanoparticles targeted with an antibody have already been used to effectively treat breast cancer xenografts in mice (17).

MAP-CPT conjugate was synthesized in a similar manner to that previously described (Fig. 3.3) (16). Properties of the material used in this study are provided in Table 3.1. MAP-CPT conjugate was dialyzed against water to promote formation of nanoparticles with hydrophobic CPT molecules preferentially clustered in the core and vicinal diols on the surface (Fig. 3.2).

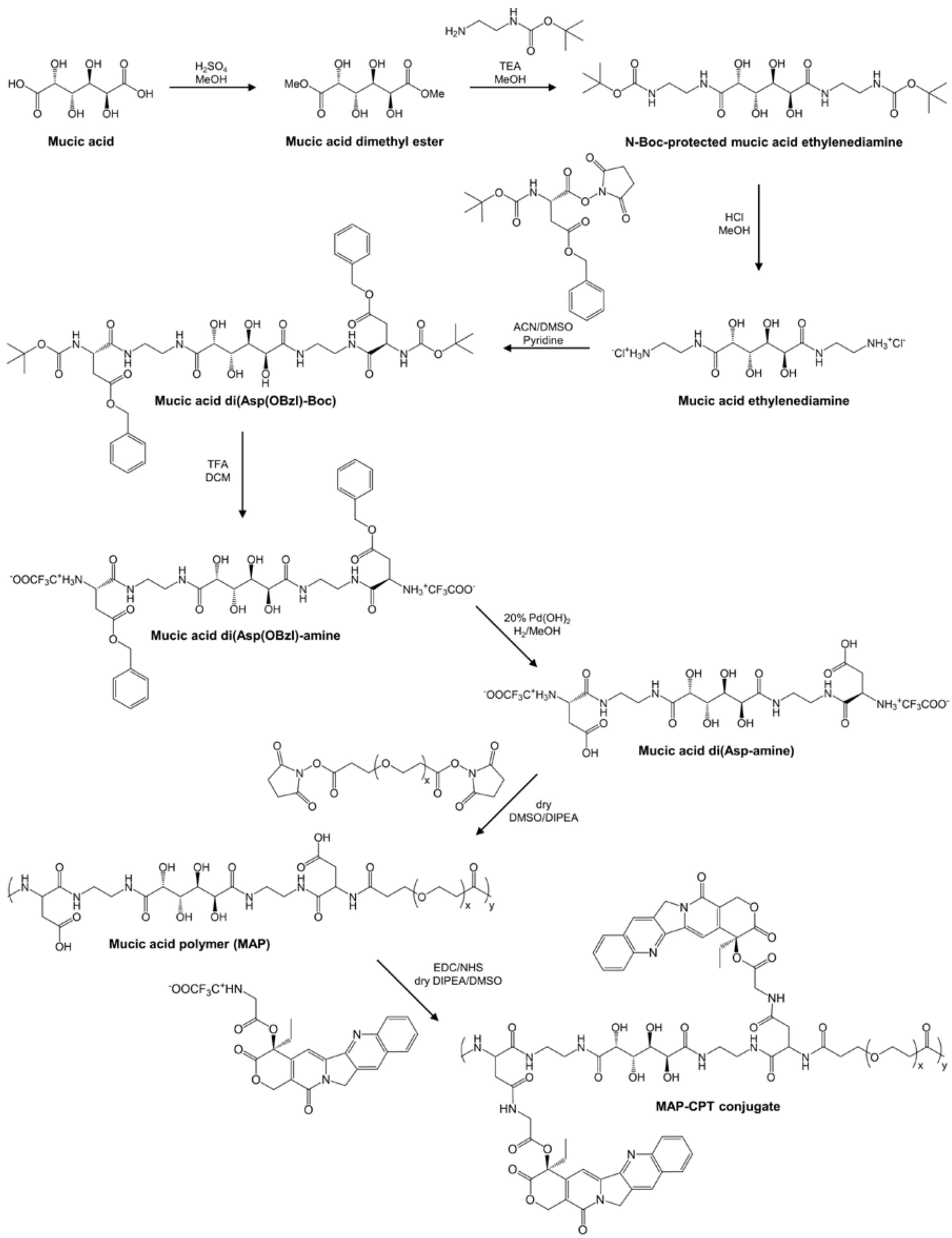

Fig. 3.3. Synthesis of MAP polymer followed by conjugation of CPT to prepare MAP-CPT conjugate. x ~ 82 for 3.4kDa PEG; y ~ 20 for material used in this study.

Material	Property	
MAP polymer	d*n*/dc (mL/g)	0.14
	MW* (kDa)	68
	Polydispersity†	1.26
MAP-CPT conjugate	Wt % CPT	11.8

Table 3.1. Properties of MAP polymer and MAP-CPT polymer-drug conjugate. *MW, molecular weight determined as $(M_w + M_n)/2$; M_w, weight average molecular weight; M_n, number average molecular weight. †Polydispersity determined as M_w / M_n.

The boronic acid derivative, 3-carboxy-5-nitrophenyl boronic acid (nitroPBA), was added to 5-kDa polyethylene glycol (PEG), followed by conjugation of the polymer to human holo-Tf (Fig. 3.4A). A non-targeted analog was prepared using methoxy-terminated 5-kDa PEG (Fig. 3.4B). NitroPBA was chosen because it forms a boronic acid ester with the MAP-CPT diols and has a pKa of 6.8 (16). The nearly instantaneous (relative to the timeframe of BBB transcytosis) dissociation of Tf-PEG-nitroPBA from the nanoparticle occurs at pH < 6.8, to provide ligand detachment during transcytosis.

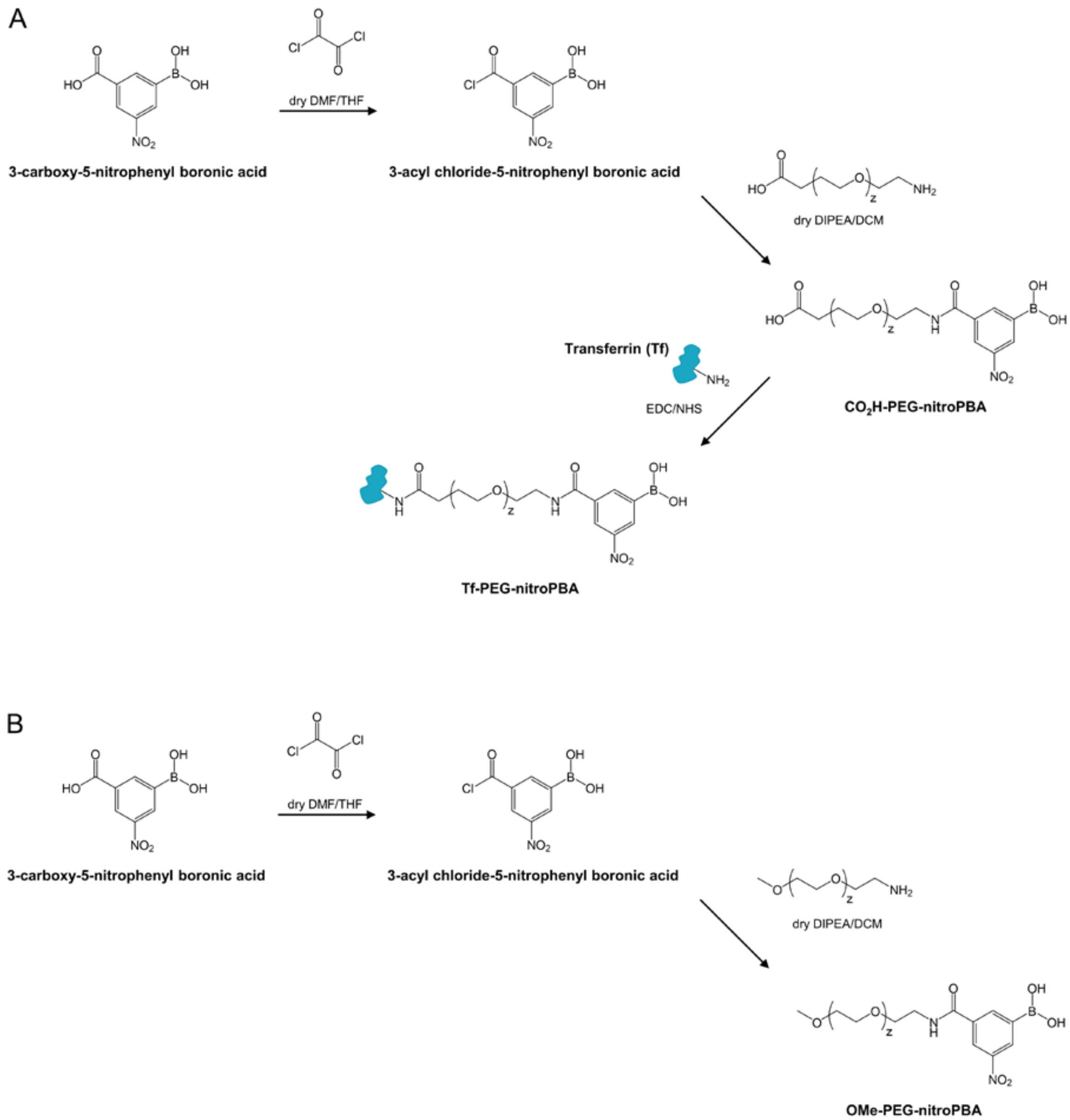

Fig. 3.4. Synthesis of nitroPBA conjugates. (**A**) Tf-PEG-nitroPBA. (**B**) OMe-PEG-nitroPBA. z ~ 120 for 5kDa PEG.

To prepare the TfR-targeted and non-targeted MAP-CPT nanoparticles, either Tf-PEG-nitroPBA or OMe-PEG-nitroPBA was added to the nanoparticles at 20 molar excess (Fig. 3.2). All nanoparticle formulations had diameters near 40 nm, as measured by dynamic light scattering, and near-neutral zeta potentials when measured in pH 7.4 buffer

(Table 3.2). The moderate increase in TfR-targeted nanoparticle size when formulated into pH 5.5 buffer is consistent with slight steric destabilization following dissociation of Tf-PEG-nitroPBA conjugates from the nanoparticle surface diols at acidic pH. Importantly, no diameter increase was observed for TfR-targeted nanoparticles after 24 h, indicating the multi-PEGylated Tfs in the crude Tf-PEG-nitroPBA mixture were not causing crosslinking between nanoparticles (Fig. 3.5).

Formulation	Nanoparticle diameter, pH 7.4, nm	Zeta potential, pH 7.4, mV	Nanoparticle diameter, pH 5.5, nm	Zeta potential, pH 5.5, mV
MAP-CPT nanoparticle	37.8 ± 1.4	-0.39 ± 0.78	38.2 ± 1.8	-0.27 ± 0.84
TfR-targeted MAP-CPT nanoparticle	29.4 ± 1.2	-1.32 ± 0.45	37.9 ± 1.3	-0.51 ± 0.42
Non-targeted MAP-CPT nanoparticle	45.6 ± 1.7	-0.57 ± 0.88	37.6 ± 1.9	-0.43 ± 0.68

Table 3.2. Nanoparticle formulations and characteristics. Data shown for hydrodynamic diameter and zeta potential are the average of 5 measurements ±1 SD.

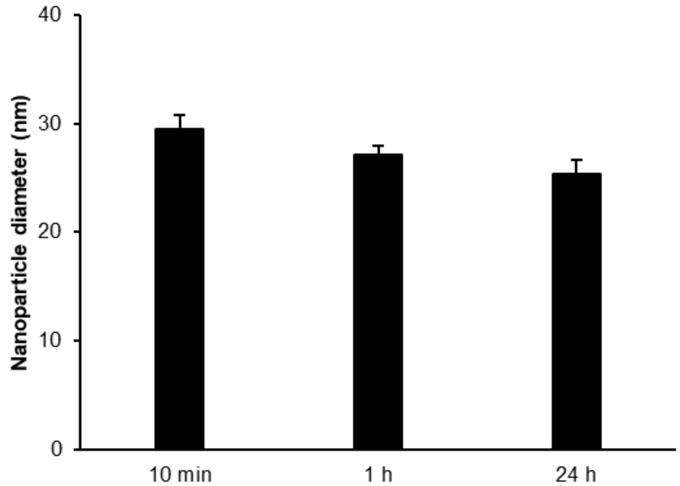

Fig. 3.5. TfR-targeted MAP-CPT nanoparticle diameter over time. No aggregation or increase in size was evident in the sample after 24 h, indicating the nanoparticles were not crosslinking due to introduction of multiple nitroPBA-PEG groups per Tf. Error bars indicate one standard deviation from the mean. Data shown are the average of 5 measurements ±1 SD.

3.2.2 Specific binding of TfR allows targeted nanoparticles to cross an *in* vitro model of the BBB

To perform an initial screen of transcytosis capacity, we used the bEnd.3 immortalized mouse brain endothelial cell line in an established *in vitro* model of the BBB (19). Nanoparticles were added to the apical compartment of bEnd.3-coated transwells in serum-free DMEM and allowed to cross the model BBB for 8 h, after which the full volume of the basal compartment was removed and CPT content measured using HPLC.

After 8 h, TfR-targeted MAP-CPT nanoparticles showed a significantly increased capacity to cross the bEnd.3 cells compared to non-targeted nanoparticles (Fig. 3.6). In addition, TfR-targeted nanoparticles showed a decreased ability to cross the model BBB when coincubated with serum concentrations of Tf, indicating TfR binding is essential to crossing. Interestingly, when coincubated with an equimolar amount of high affinity anti-

TfR Abs, TfR-targeted nanoparticles also revealed a decreased ability to cross the transwells, consistent with previous reports of high-affinity Ab:TfR interactions leading to lysosomal trafficking (7).

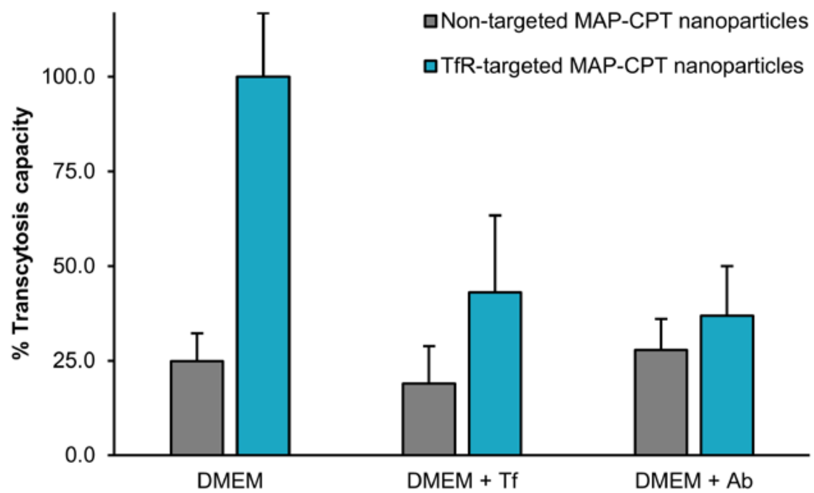

Fig. 3.6. Apical to basal transport of non-targeted and TfR-targeted MAP-CPT nanoparticles in model BBB. TfR-targeted (blue) and non-targeted (orange) nanoparticles were added to apical wells in either serum-free DMEM (DMEM), or in the presence of either 2.5 mg/mL Tf (DMEM + Tf) or equimolar high-affinity anti-TfR Ab (DMEM + Ab). Data shown are the average of 4 wells for each group. Error bars indicate SE.

3.2.3 Brain tumors show significant delay in growth with TfR-targeted nanoparticles, but their response differs when established by different methods

We compared the efficacy of TfR-targeted MAP-CPT nanoparticles, non-targeted MAP-CPT nanoparticles and CPT on the growth of BT474-Gluc brain metastatic tumors in Rag2$^{-/-}$;Il2rg$^{-/-}$ mice established by IC, ICD and IV methods (Fig. 3.7). As detailed in Chapter II, this cell line was engineered to express Gaussia luciferase (Gluc) that can be used as a surrogate for tumor burden (20). Additionally, Rag2$^{-/-}$;Il2rg$^{-/-}$ mice were chosen because they have shown the ability to allow multi-organ metastatic spread of HER2-

positive breast cancer cell lines injected IV (21). After IC, ICD or IV injection of BT474-Gluc cells, formation of brain metastatic tumors was monitored by MRI. A total of six mice were used for each treatment group per model, and treatment was initiated when tumors reached 2 mm^3 in volume. The different formulations were systemically administered by lateral tail vein injection once per week for 4 weeks at a dose of 4 mg/kg (CPT basis). Brain tumor volume was measured weekly by MRI. Blood Gluc activity was measured in addition only for the IC model, due to substantial extracranial tumor burden in the ICD and IV models.

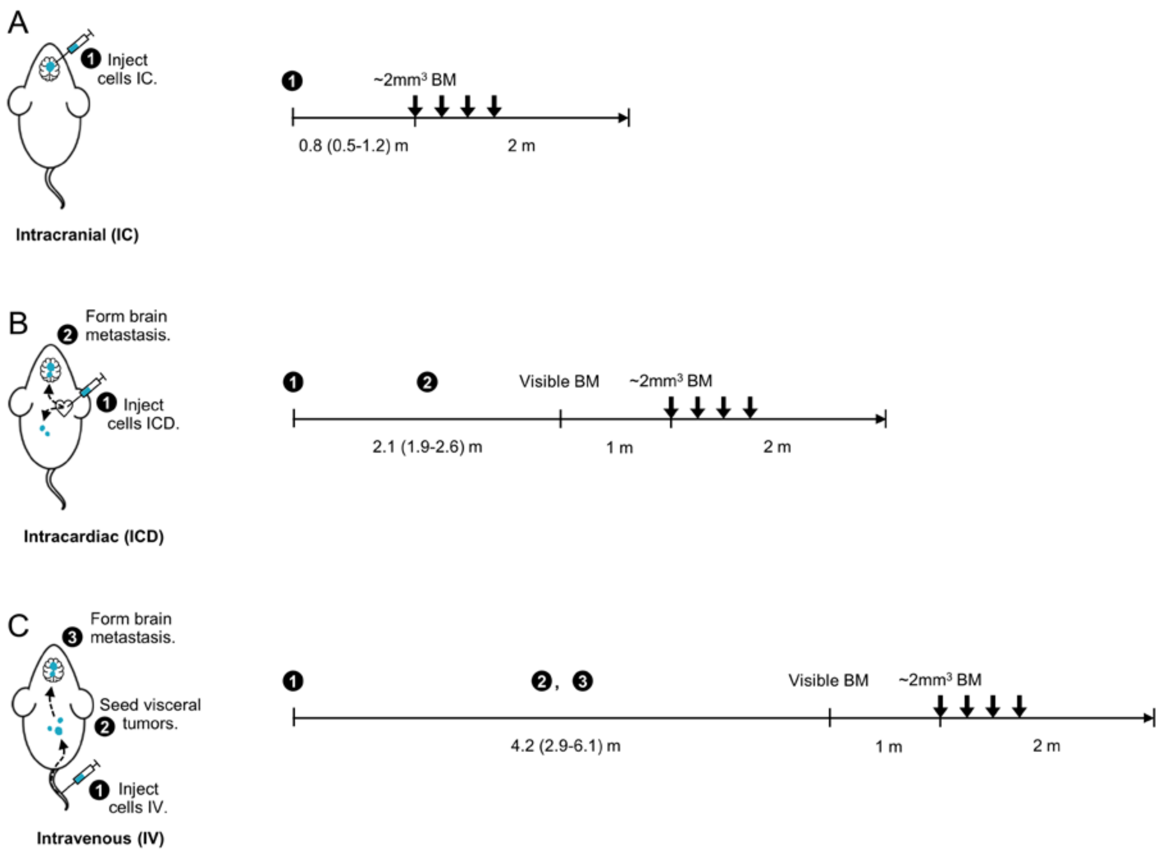

Fig. 3.7. Detailed illustration of intracranial (**A**), intracardiac (**B**), and intravenous (**C**) breast cancer brain metastasis models, and timelines for efficacy study. Numbers below timeline indicate mean (range) time in months to establishment of visible brain metastases (BM; ~0.2 mm^3 in volume) by MRI. Thick arrows denote treatment schedule for the study, with 4 weekly doses administered once tumors reached ~2 mm^3 in volume.

TfR-targeted MAP-CPT nanoparticles significantly delayed brain metastatic tumor growth compared to saline in mice bearing IC-established brain tumors, resulting in an 8.4-fold decrease in mean tumor volume by the end of the study (Fig. 3.8A and Table 3.3). However, treatment with non-targeted MAP-CPT nanoparticles or CPT also led to substantial tumor growth inhibition (3.5- or 2.6-fold reduction in mean final tumor volume, respectively), supporting the hypothesis that artificial transport pathways may be introduced following IC tumor establishment. The blood Gluc activity for each treatment group correlated well with tumor volume as measured by MRI (Fig. 3.9). Individual antitumor data are provided in Fig. 3.10.

In contrast to results from the IC model, only treatment with TfR-targeted MAP-CPT nanoparticles resulted in substantial tumor growth delay compared to saline when tumors were established by ICD injection (2.6-fold decrease in mean tumor volume; Fig. 3.8B and Table 3.4). Interestingly, we observed a modest response with CPT treatment, but not with non-targeted MAP-CPT nanoparticles (although this difference was not significant).

Similar to the ICD model, with IV-established brain tumors, TfR-targeted MAP-CPT nanoparticles markedly slowed tumor growth compared to saline (2.5-fold decrease in mean tumor volume; Fig. 3.8C and Table 3.5). Notably, no tumor growth inhibition was observed with CPT or non-targeted MAP-CPT nanoparticles compared to saline in this model, more closely replicating the clinical situation.

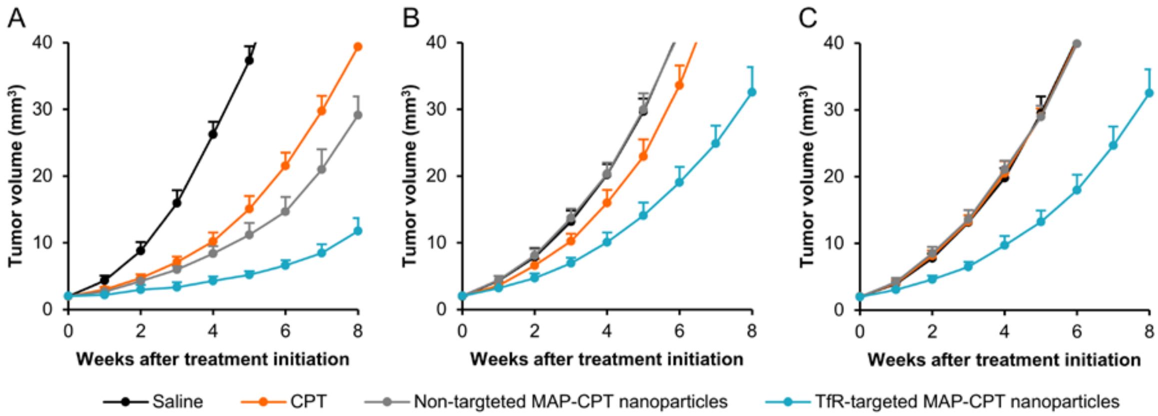

Fig. 3.8. Brain tumors established using different methods show differential response to therapeutics. Tumor growth curves of BT474-Gluc metastatic brain tumors treated with CPT (orange, 4 mg/kg), non-targeted MAP-CPT nanoparticles (gray, 4 mg CPT/kg), and TfR-targeted MAP-CPT nanoparticles (blue, 4 mg CPT/kg) compared to saline (black) when established by IC (**A**), ICD (**B**), and IV injection (**C**). Data shown are the average of 6 mice per treatment group. Error bars indicate SE. *P* values for pairwise comparisons are provided in Tables 3.3 to 3.5.

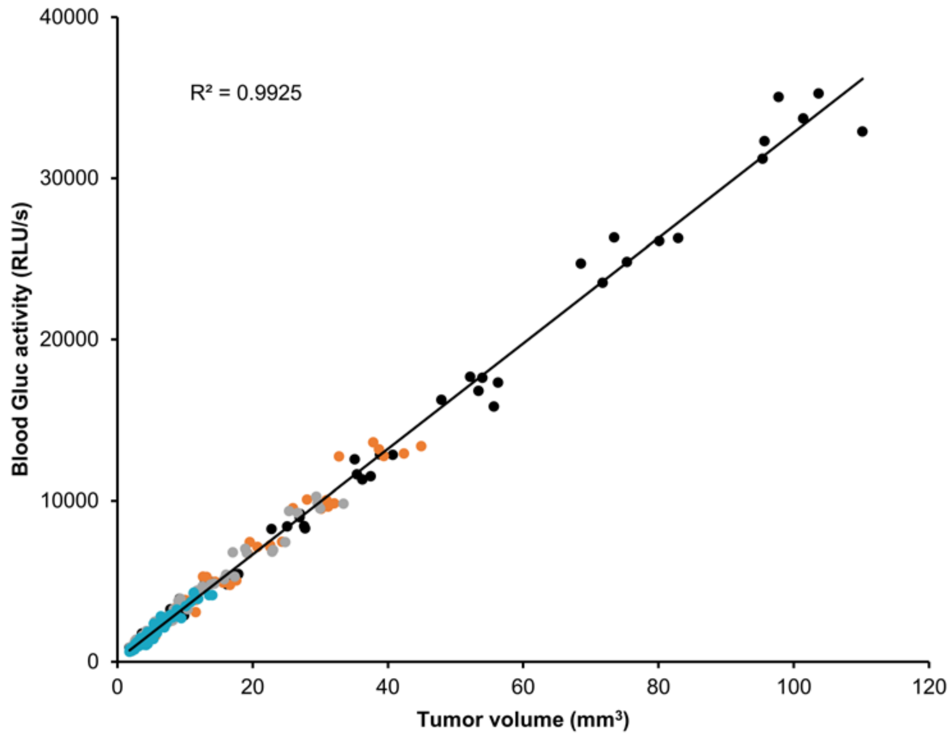

Fig. 3.9. Blood Gluc activity of IC-established tumors is correlated with tumor volume, as measured by MRI, for each treatment group. Blood Gluc activity is plotted against tumor volume for saline (black), CPT (orange), non-targeted MAP-CPT nanoparticle (gray), and TfR-targeted MAP-CPT nanoparticle (blue) treatment groups. Linear regression was performed using MATLAB.

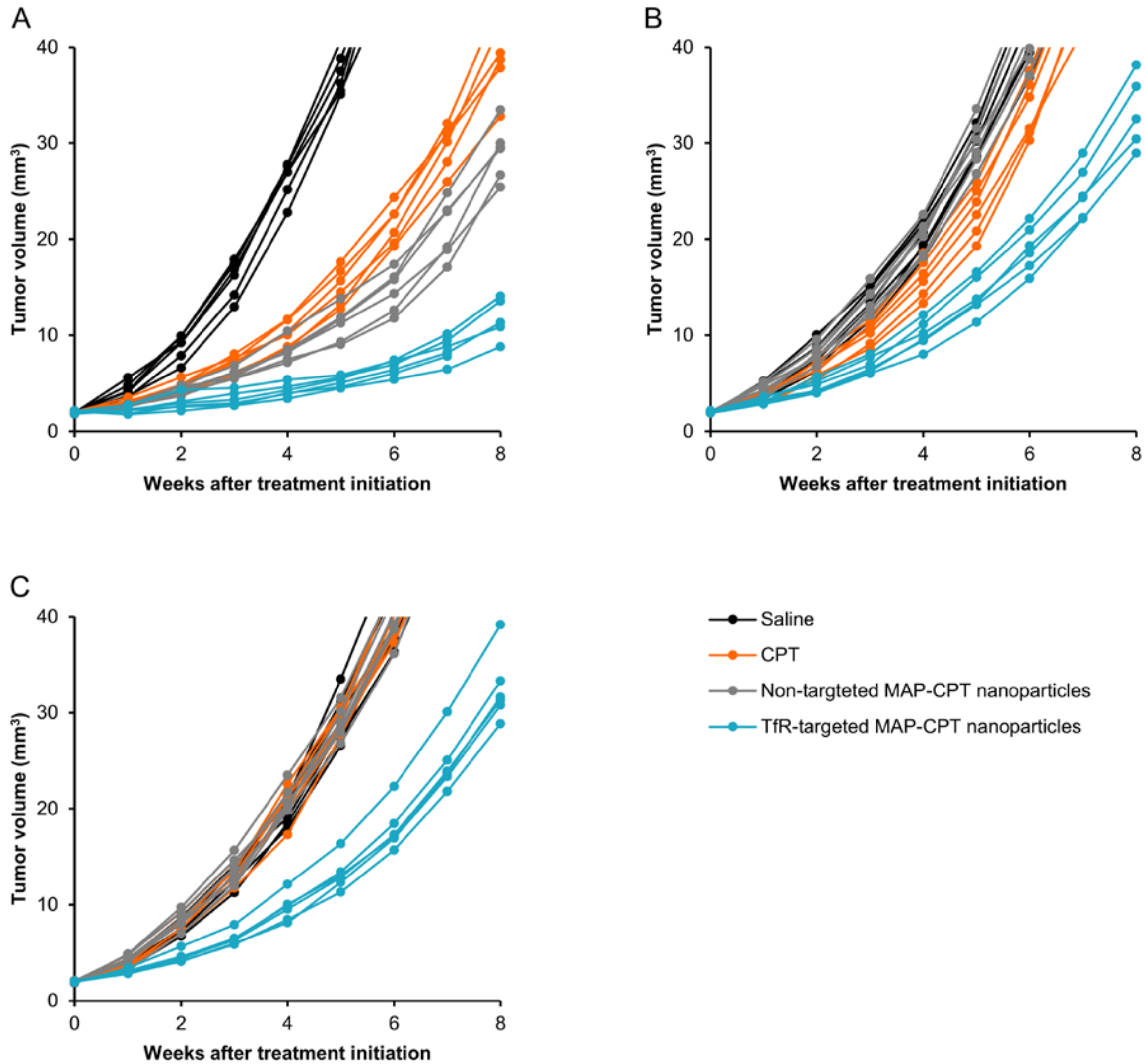

Fig. 3.10. Individual tumor growth curves of BT474-Gluc metastatic brain tumors treated with CPT (orange, 4 mg/kg), non-targeted MAP-CPT nanoparticles (gray, 4 mg CPT/kg), and TfR-targeted MAP-CPT nanoparticles (blue, 4 mg CPT/kg) compared to saline (black) when established by IC (**A**), ICD (**B**), and IV injection (**C**).

	Mean tumor volume (mm³)	Median tumor volume (mm³)	*P* vs. saline
Saline	101	100	-
CPT (4 mg/kg)	39	39	0.0022
Non-targeted MAP-CPT nanoparticle (4 mg CPT/kg)	29	30	0.0022
TfR-targeted MAP-CPT nanoparticle (4 mg CPT/kg)	12	12	0.0022

Table 3.3. Antitumor efficacy in Rag2$^{-/-}$;Il2rg$^{-/-}$ mice bearing human BT474-Gluc breast cancer metastatic brain tumors established by IC injection. Data provided are mean and median tumor volumes at the end of the study. *P* values were calculated using the Wilcoxon-Mann-Whitney test.

	Mean tumor volume (mm³)	Median tumor volume (mm³)	*P* vs. saline
Saline	87	88	-
CPT (4 mg/kg)	69	71	0.0022
Non-targeted MAP-CPT nanoparticle (4 mg of CPT/kg)	87	89	0.9372
TfR-targeted MAP-CPT nanoparticle (4 mg of CPT/kg)	33	32	0.0022

Table 3.4. Antitumor efficacy in Rag2$^{-/-}$;Il2rg$^{-/-}$ mice bearing human BT474-Gluc breast cancer metastatic brain tumors established by ICD injection. Data provided are mean and median tumor volumes at the end of the study. *P* values were calculated using the Wilcoxon-Mann-Whitney test.

	Mean tumor volume (mm³)	Median tumor volume (mm³)	*P* vs. saline
Saline	83	83	-
CPT (4 mg/kg)	86	86	0.5887
Non-targeted MAP-CPT nanoparticle (4 mg of CPT/kg)	84	84	0.9372
TfR-targeted MAP-CPT nanoparticle (4 mg of CPT/kg)	33	31	0.0022

Table 3.5. Antitumor efficacy in Rag2$^{-/-}$;Il2rg$^{-/-}$ mice bearing human BT474-Gluc breast cancer metastatic brain tumors established by IV injection. Data provided are mean and median tumor volumes at the end of the study. *P* values were calculated using the Wilcoxon-Mann-Whitney test.

3.2.4 Brain uptake of therapeutics differs in tumor, but not healthy tissue between models

To ascertain whether differences in brain penetration of the therapeutics might explain the discordance in efficacy between brain metastasis models, we systemically administered an additional dose of each treatment at the end of the efficacy study. After 24 h, mice were anesthetized and perfused with PBS to clear any remaining nanoparticles or free drug from the bloodstream. Drug uptake into tumor and healthy brain tissue was quantified by HPLC as previously described (17).

Tumor tissue collected from IC-established, but not from ICD- and IV-established brain tumors showed significant accumulation of CPT and non-targeted MAP-CPT nanoparticles, consistent with the hypothesis that the barrier in IC-established tumors may be more permeable to therapeutics than what is observed in patients with HER2-positive disease (Fig. 3.11A). In addition, cells isolated from BT474-Gluc tumors from all three models as well as the respective parental cells had comparable sensitivities to CPT in vitro (Fig. 3.12), ruling out permanent, model-specific drug sensitivity as the origin for anti-tumor differences. Thus, these data strongly implicate BBB/BTB permeability to the therapeutic agents as a mediator of the differential treatment response between the models.

Importantly, TfR-targeted MAP-CPT nanoparticles showed the highest accumulation in IC-, ICD- and IV-established brain tumor tissue. In addition, TfR-targeted nanoparticles demonstrated increased penetration into healthy brain tissue relative to free drug and non-targeted nanoparticles in all three models (Fig. 3.11B). As with the antitumor efficacy data, these results further indicate the potential of the TfR-targeted nanoparticle delivery system.

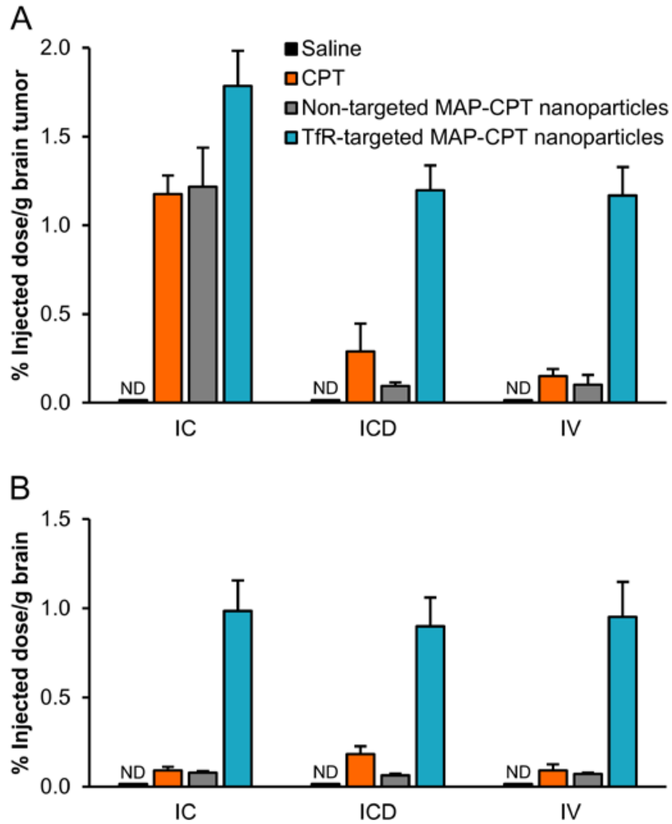

Fig. 3.11. Brain uptake of therapeutics is model-dependent in tumor, but not healthy tissue. (**A**) Brain uptake in BT474-Gluc tumor tissue as calculated by percent injected dose per g of tissue for different treatments. (**B**) Percent injected dose in healthy brain tissue. Brain uptake was determined 24 h after a 4 mg/kg dose (CPT basis). Data shown are the average of 4 mice per treatment group. Error bars indicate SE. ND, not detectable. *P* values for pairwise comparisons are provided in Tables 3.6 and 3.7.

	IC-CPT[*]	IC-Non[†]	IC-TfR[‡]	ICD-CPT[§]	ICD-Non[¶]	ICD-TfR[#]	IV-CPT[‖]	IV-Non[**]	IV-TfR[††]
IC-CPT	X	-	-	-	-	-	-	-	-
IC-Non	0.8857	X	-	-	-	-	-	-	-
IC-TfR	0.0286	0.0286	X	-	-	-	-	-	-
ICD-CPT	0.0286	0.0286	0.0286	X	-	-	-	-	-
ICD-Non	0.0286	0.0286	0.0286	0.0571	X	-	-	-	-
ICD-TfR	0.8857	0.8857	0.0286	0.0286	0.0286	X	-	-	-
IV-CPT	0.0286	0.0286	0.0286	0.2286	0.0571	0.0286	X	-	-
IV-Non	0.0286	0.0286	0.0286	0.0571	0.9714	0.0286	0.2000	X	-
IV-TfR	0.8857	0.8571	0.0286	0.0286	0.0286	1.000	0.0286	0.0286	X

Table 3.6. *P* values for pairwise comparisons of uptake of therapeutics in brain metastases. Values were calculated using the Wilcoxon-Mann-Whitney test. [*]CPT, IC model; [†]Non-targeted MAP-CPT nanoparticles, IC model; [‡]TfR-targeted MAP-CPT nanoparticles, IC model; [§]CPT, ICD model; [¶]Non-targeted MAP-CPT nanoparticles, ICD model; [#]TfR-targeted MAP-CPT nanoparticles, ICD model; [‖]CPT, IV model; [**]Non-targeted MAP-CPT nanoparticles, IV model; [††]TfR-targeted MAP-CPT nanoparticles, IV model.

	IC-CPT*	IC-Non†	IC-TfR‡	ICD-CPT§	ICD-Non¶	ICD-TfR#	IV-CPT‖	IV-Non**	IV-TfR††
IC-CPT	X	-	-	-	-	-	-	-	-
IC-Non	0.5714	X	-	-	-	-	-	-	-
IC-TfR	0.0286	0.0286	X	-	-	-	-	-	-
ICD-CPT	0.0286	0.0286	0.0286	X	-	-	-	-	-
ICD-Non	0.0857	0.1714	0.0286	0.0286	X	-	-	-	-
ICD-TfR	0.0286	0.0286	0.4857	0.0286	0.0286	X	-	-	-
IV-CPT	0.8286	1.000	0.0286	0.0571	0.2857	0.0286	X	-	-
IV-Non	0.2000	0.4857	0.0286	0.0286	0.4857	0.0286	0.5714	X	-
IV-TfR	0.0286	0.0286	0.9714	0.0286	0.0286	0.8857	0.0286	0.0286	X

Table 3.7. *P* values for pairwise comparisons of uptake of therapeutics in healthy brain tissue. Values were calculated using the Wilcoxon-Mann-Whitney test. *CPT, IC model; †Non-targeted MAP-CPT nanoparticles, IC model; ‡TfR-targeted MAP-CPT nanoparticles, IC model; §CPT, ICD model; ¶Non-targeted MAP-CPT nanoparticles, ICD model; #TfR-targeted MAP-CPT nanoparticles, ICD model; ‖CPT, IV model; **Non-targeted MAP-CPT nanoparticles, IV model; ††TfR-targeted MAP-CPT nanoparticles, IV model.

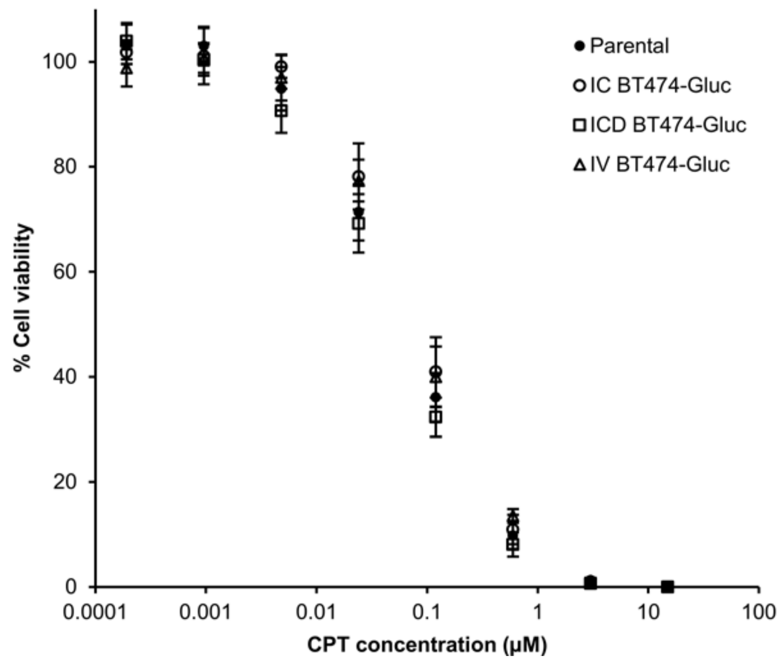

Fig. 3.12. BT474-Gluc cells isolated from brain tumors following IC- (circle), ICD- (square), and IV-establishment (triangle) as well as parental cells (solid circle) are similarly sensitive to CPT. Data shown are the average of 4 dose-response curves for each cell line. Error bars indicate SE.

3.3 Discussion

Here, we focused on understanding whether two types of breast cancer brain metastasis mouse models from the literature as well as a third, new model created in this study provide impaired drug delivery to brain metastases like what is observed for patients with HER2-positive, metastatic breast cancer. In patients, non-BBB-permeable agents are unable to accumulate in brain metastases in pharmacologically active amounts. However, we did not observe this same delivery limitation in the IC model. Our results show that a non-BBB-penetrant small molecule (CPT) and a non-targeted nanoparticle therapeutic (ca. 30-40 nm diameter) can elicit a significant antitumor response as well as accumulate in high amounts in IC-established brain tumors. Although this model may be useful for studying basic biological mechanisms, our findings suggest this model must be used with caution for translational research with diseases where a non-permissive BBB is clinically relevant.

In contrast to the IC model, both the ICD and IV models provide for a more intact BBB/BTB. Our results indicate that the ICD model may allow for a slightly increased permeability to small molecule drugs, but not to larger nanoparticle entities when compared to the IV model. Consistent with a modest uptake in healthy brain tissue, it is possible that the high number of microscopic tumor foci commonly observed throughout the brain following ICD injection may contribute to a slight net increase in parenchymal penetration as a whole. Nevertheless, this effect was minimal. Most importantly, our data show that the method of establishing brain tumors can dramatically affect the efficacy of therapeutics and their brain penetration. Thus, if the experimenter is interested in transport properties of a given therapeutic, then the use of the IC model is questionable.

Additionally, we show that TfR-targeted nanoparticles are capable of delivering a small molecule chemotherapeutic, CPT, to HER2-positive breast cancer brain metastases. We observed that TfR-targeted MAP-CPT nanoparticles significantly slowed tumor growth in the brain and demonstrated increased accumulation in brain metastases relative to free drug and non-targeted nanoparticles. The specific example of assembling a TfR-targeted nanoparticle system for CPT was selected to test the delivery strategy. CPT is not a particularly good drug for use with BT474 cells (relative to other breast cancer cell lines (16)). Thus, it is encouraging to observe tumor growth delay when delivering CPT via targeted nanoparticles to the BT474-Gluc brain metastases. It is expected that TfR-targeted nanoparticles delivering therapeutic agents with greater potency will reveal even more significant tumor size reductions.

Further, it is important to note that TfR-targeted nanoparticles accumulated in significant amounts in healthy brain tissue when compared to free drug and non-targeted nanoparticles in all three models. This observed whole-brain penetration has implications for the selection of therapeutics that should be incorporated into this delivery system and of target diseases. In the case of brain cancers, the ability to penetrate not only tumor tissue, but also healthy tissue could be advantageous in accessing micrometastases or fingers of glioma tumors that are frequently the reason for treatment failure. At the same time, the broad nanoparticle accumulation in the brain will require careful thought as to which drugs are used in this application, due to potential toxicity issues. For other brain diseases where whole-brain therapeutic exposure is highly desired, such as neurodegenerative diseases, this targeted nanoparticle system may offer a compelling approach to delivering therapeutics across an intact BBB.

3.4 Conclusions

Here, we show that the method used to establish breast cancer brain metastases can affect efficacy and brain uptake of therapeutic agents. We observed a significant antitumor response as well as brain tumor accumulation of a non-BBB-penetrant small molecule and a non-targeted nanoparticle therapeutic in tumors that were formed by IC injection of human breast cancer cells. In contrast, both ICD and IV injection of the cancer cells provided for a more clinically relevant, impermeable BBB/BTB to non-penetrant agents. Additionally, we show that TfR-targeted MAP-CPT nanoparticles can accumulate in brain metastases in greater amounts and lead to improved antitumor activity compared to free drug and non-targeted MAP-CPT nanoparticles. Furthermore, TfR-targeted nanoparticles showed an increased ability to cross an intact BBB, resulting in whole-brain therapeutic accumulation.

3.5 Materials and methods

Synthesis of MAP-CPT Conjugate. ^{1}H NMR spectra were acquired on a Varian 600 MHz spectrometer (Inova). Electrospray ionization (ESI) masses of small molecules were acquired on a Finnigan LCQ ion trap mass spectrometer. Matrix-assisted laser desorption/ionization-time-of-flight (MALDI-TOF) mass spectra for polymers were acquired on an Applied Biosystems Voyager DE-PRO.

Synthesis of Mucic Acid Dimethyl Ester. Methanol (360 mL) was added to mucic acid (15 g, 1 equiv, Alfa Aesar) in a 500 mL round-bottomed flask. To this was added concentrated sulfuric acid (1.2 mL, 0.3 equiv). The suspension was stirred and refluxed at 85 ºC overnight. The mixture was cooled to room temperature and filtered through a Buchner funnel using Whatman Grade 5 filter paper. The solid was washed with methanol (600 mL), and recrystallized with a mixture of methanol (240 mL) and triethylamine (1.5 mL) at 85 ºC for 1 h. The mixture was again cooled to room temperature and filtered. The solid was washed with methanol (600 mL), and dried under vacuum at 75 ºC overnight to yield mucic acid dimethyl ester (14.2 g) as a white solid. ^{1}H NMR (600 MHz, DMSO-d_6): 4.91 (d, 2H), 4.80 (q, 2H), 4.28 (d, 2H), 3.78 (q, 2H), 3.63 (s, 6H). ESI/MS: 261.0 $[M+Na]^+$.

Synthesis of N-Boc-Protected Mucic Acid Ethylenediamine. Methanol (225 mL) was added to mucic acid dimethyl ester (14.2 g, 1 equiv) in a 500 mL round-bottomed flask. To this was added triethylamine (21.7 mL, 2.6 equiv), and the mixture was stirred and refluxed at 85 ºC for 30 min, forming a yellow suspension. N-Boc-ethylenediamine (24.6 mL, 2.6 equiv, AK Scientific) in methanol (55 mL) was added, and the reaction was stirred and refluxed at 85 ºC overnight. The mixture was cooled to room temperature, and filtered through a Buchner funnel using Whatman Grade 5 filter paper. The solid was washed with methanol (750 mL), and recrystallized with methanol (350 mL) at 85 ºC for 1.5 h. The mixture was again cooled to room temperature and filtered. The solid was washed with methanol (750 mL), and dried under vacuum at 75 ºC overnight to yield N-Boc-protected mucic acid ethylenediamine (19.2 g) as a white solid. ^{1}H NMR (600 MHz, DMSO-d_6): 7.71 (t, 2H), 6.81 (t, 2H), 5.13 (d, 2H), 4.35 (q, 2H), 4.09 (d, 2H), 3.77 (q, 2H), 3.12 (m, 4H), 2.98 (m, 4H), 1.36 (s, 18). ESI/MS: 517.1 $[M+Na]^+$.

Synthesis of Mucic Acid Ethylenediamine. N N-Boc-protected mucic acid ethylenediamine (19.2 g) in a 500 mL round-bottomed flask was placed in a water bath. 3 N hydrochloric acid in methanol (325 mL) was added, and the reaction flask was sealed and vented with a needle. The suspension was stirred at 25 ºC for 8 h. The slurry was filtered through a glass frit with a fine grain, and washed with methanol (900 mL) until the filtrate pH was close to neutral. The solid was dried under vacuum at 80 ºC overnight to yield mucic acid ethylenediamine (11.5 g) as a white solid. ^{1}H NMR (600 MHz, DMSO-d_6): 7.97–7.84 (m, 8H), 5.30 (d, 2H), 4.58 (d, 2H), 4.16 (d, 2H), 3.82 (m, 2H), 3.39–3.32 (m, 4H), 2.85 (m, 4H). ESI/MS: 295.0 $[M+H]^+$.

Synthesis of Mucic Acid Di(Asp(OBzl)-Boc). Mucic acid ethylenediamine (3 g, 1 equiv) was dissolved in 30 mL DMSO in a 250 mL round-bottomed flask. To this was added Boc-Asp(OBzl)-OSu (10.3 g, 3 equiv, Bachem) in acetonitrile (80 mL) and pyridine (3.2 mL, 5 equiv). The reaction was stirred and refluxed at 60 ºC overnight. The mixture was cooled to room temperature, and acetonitrile was removed by rotary evaporation. The solution was precipitated by addition of nanopure water, and the precipitate was recrystallized with nanopure water (100 mL) at 85 ºC for 1 h. The mixture was cooled to room temperature, filtered through a glass frit with a fine grain, and washed with nanopure water (200 mL). The recrystallization procedure was repeated with acetonitrile. The solid was dried under vacuum at 50 ºC overnight to yield mucic acid di(Asp(OBzl)-Boc) (2.1 g) as a white solid. ^{1}H NMR (600 MHz, DMSO-d_6): 7.94 (t, 2H), 7.76 (t, 2H), 7.37–7.31 (m, 10H), 7.06 (d, 2H), 5.13–5.08 (m, 6H), 4.37–4.32 (d, 2H), 4.30–4.28 (d, 2H), 4.14–4.12 (d, 2H), 3.81–3.79 (d, 2H), 3.18–3.09 (m, 8H), 2.79–2.57 (m, 4H), 1.38 (s, 18H). ESI/MS: 905.0 $[M+H]^+$.

Synthesis of Mucic Acid Di(Asp(OBzl)-amine). Dichloromethane (18 mL) was added to mucic acid di(Asp(OBzl)-Boc) (2.1 g, 1 equiv) in a 50 mL round-bottomed flask vented with argon. The flask was cooled to 0 ºC in an ice bath, and trifluoroacetic acid (6 mL, 36 equiv) was added dropwise. The reaction was stirred for 8 h under argon, slowly equilibrating to room temperature. Solvent was removed by rotary evaporation. The solid was dissolved in dichloromethane (30 mL) and dried by rotary evaporation twice more, and then recrystallized with tetrahydrofuran (30 mL) at 55 ºC for 1 h. The mixture was cooled to room temperature and filtered through a glass frit with a fine grain. The solid was washed with tetrahydrofuran (100 mL), and dried under vacuum at 50 ºC overnight to yield mucic acid di(Asp(OBzl)-amine) (1.4 g) as a white solid. ^{1}H NMR (600 MHz, DMSO-d_6): 8.46 (t, 2H), 8.21 (s, 6H), 7.80 (t, 2H), 7.39–7.35 (m, 10H), 5.19–5.16 (t, 2H), 5.13 (s, 4H), 4.41 (s, 2H), 4.15–4.13 (d, 2H), 4.06–4.04 (d, 2H), 3.83 (s, 2H), 3.22–3.16 (m, 8H), 3.02–2.83 (m, 4H). ESI/MS: 705.3 $[M+H]^+$.

Synthesis of Mucic Acid Di(Asp-amine). Methanol (50 mL) was added to mucic acid di(Asp(OBzl)-amine) (1.4 g, 1 equiv) and 20% (w) palladium hydroxide on carbon (568 mg, 10 equiv) in a 100 mL round-bottomed flask. The reaction flask was sealed and vented with argon for 30 min. Hydrogen gas was added by a double-layered balloon, and the reaction was stirred for 24 h at room temperature. Catalyst was separated by centrifugation at 3220 g for 15 min, and the solvent removed by rotary evaporation. The solid was reconstituted in nanopure water, and the solution was filtered through a 0.2 µm Supor membrane Acrodisc syringe filter (Pall) and lyophilized to yield mucic acid di(Asp-amine) (1.1 g) as a white solid. ^{1}H NMR (600 MHz, DMSO-d_6): 8.39 (t, 2H), 8.18 (broad, 6H), 7.77 (t, 2H), 5.18 (t, 2H), 4.46 (s, 2H), 4.12 (s, 2H), 3.96–3.94 (m, 2H), 3.79 (s, 2H), 3.21–3.11 (m, 8H), 2.84–2.65 (m, 4H). ESI/MS: 525.2 $[M+H]^+$. The product was stored under argon at -20 ºC.

Synthesis of Mucic Acid Polymer (MAP). Mucic acid di(Asp-amine) (220 mg, 1 equiv) and di(succinimidyl proprionate)-PEG (3.4 kDa, 1 g, 1 equiv, JenKem) were equilibrated to room temperature for 1 h, then added to an oven-dried 10 mL round-bottomed flask. The reaction flask was sealed, and the two solids were dried under vacuum for 4 h. Anhydrous dimethyl sulfoxide (7 mL) was added under argon to dissolve the two solids. To this was added anhydrous N,N-diisopropylethylamine (205 µL, 4 equiv) dried over molecular sieves, and the solution was stirred under argon at room temperature for 42 h. The solution was dialyzed against dimethyl sulfoxide and nanopure water using a 10 kDa MWCO Spectra/Por 7 membrane (Spectrum), filtered through a 0.2 µm Supor membrane Acrodisc syringe filter (Pall) and lyophilized to yield MAP (983 mg) as a white, sponge-like solid. ^{1}H NMR (600 MHz, DMSO-d_6): 8.11 (d, 1H), 8.08 (d, 1H), 7.83 (t, 1H), 7.79 (t, 1H), 7.73 (t, 2H), 4.49 (td, 2H), 4.14 (d, 2H), 3.69 (ddt, 2H), 3.59 (t, 4.3H), 3.53–3.43 (s - PEG), 3.18–3.07 (m, 8H), 2.61–2.43 (m, 4H), 2.38 (t, 4.3H).

Determination of MAP Molecular Weight. Polymer molecular weight was determined on a gel permeation chromatography (GPC) system equipped with an Agilent 1100 HPLC with binary pump and injector with 2 size exclusion columns in series (PL aquagel-OH 40 8 µm, Agilent) connected to Wyatt DAWN HELEOS light scattering and Wyatt Optilab rEX refractive index detectors. MAP was dissolved at six different concentrations in PBS, pH 7.4 and directly injected into the refractive index detector at 0.2 mL/min using a syringe pump to determine specific refractive increment, d*n*/dc. Absolute molecular weight was determined by injecting 100 µL of MAP dissolved at 4 mg/mL in PBS, pH 7.4 onto the column. PBS was used as the eluent at a flow rate of 0.7 mL/min, and the detected polymer peak was analyzed using ASTRA V Software.

Synthesis of MAP-CPT Conjugate. Anhydrous dimethyl sulfoxide (10 mL) was added under argon to dissolve MAP (200 mg, 1 equiv) in a 25 mL round-bottomed flask. To this was added EDC (83 mg, 4 equiv) and NHS (32 mg, 3 equiv) dissolved in anhydrous dimethyl sulfoxide (3 mL), followed by 20-O-Glycincamptothecin trifluoroacetic acid salt (CPT-gly.TFA, 170 mg, 3 equiv) dissolved in dimethyl sulfoxide (3 mL) and anhydrous N,N-diisopropylethylamine (56 µL) dried over molecular sieves. The reaction was stirred under argon at room temperature overnight. The solution was dialyzed against dimethyl sulfoxide 3 times and nanopure water 2 times using a 10 kDa MWCO Spectra/Por 7 membrane (Spectrum). Precipitate was removed by centrifugation at 3220 g for 15 min, and the supernatant was filtered through a 0.2 µm Supor membrane Acrodisc syringe filter (Pall) to yield MAP-CPT conjugate as self-assembled nanoparticles in solution. A portion of this clear yellow solution was lyophilized to determine percent CPT conjugation. The remaining product was formulated into 0.9% (w/v) saline and stored at -20 ºC.

Determination of CPT Content in MAP-CPT. Lyophilized MAP-CPT was dissolved in dimethyl sulfoxide at 10 mg/mL, diluted to 0.1 mg/mL with 1 N NaOH, and incubated overnight. Fluorescence was measured at 370/440 nm (ex/em) using a Safire 2 multi-mode plate reader (Tecan). A calibration curve of known concentrations of CPT was prepared and used to determine the CPT concentration in the mixture.

Synthesis of CO_2H-PEG-nitroPBA and OMe-PEG-nitroPBA.

Synthesis of 3-acyl chloride-5-nitrophenyl boronic acid. 3-carboxy-5-nitrophenyl boronic acid (nitroPBA, 100 mg, 1 equiv, Alfa Aesar) was added to an oven-dried 10 mL round-bottomed flask. The reaction flask was sealed and vented with argon. Anhydrous tetrahydrofuran with BHT inhibitor (4 mL) was added to dissolve the boronic acid, followed by anhydrous dimethylformamide (7 µL, 0.2 equiv). The flask was cooled to 0 ºC in an ice bath, and oxalyl chloride (98 µL, 2.4 equiv) was added dropwise. After addition of oxalyl chloride, the ice bath was removed and the reaction was stirred under argon for 2 hrs. Solvent was evaporated under vacuum to yield 3-acyl chloride-5-nitrophenyl boronic acid (108 mg) as a yellow solid.

Synthesis of CO_2H-PEG-nitroPBA and OMe-PEG-nitroPBA. 3-acyl chloride-5-nitrophenyl boronic acid (46 mg, 2 equiv) was added to an oven-dried 25 mL round-bottomed flask. The reaction flask was sealed, vented with argon, and cooled to 0 ºC in an ice bath. Anhydrous DCM (5 mL) was added to dissolve the boronic acid. Acetic acid-PEG-amine (5 kDa, 500 mg, 1 equiv, JenKem) was added to a separate oven-dried 10 mL round-bottomed flask. The flask was sealed, and vented with argon. To this was added anhydrous N,N-diisopropylethylamine (35 µL, 2 equiv) dried over molecular sieves, and anhydrous DCM (5 mL) to dissolve the PEG. The PEG solution was added dropwise to the boronic acid solution. The reaction flask was left in the ice bath to slowly warm to room temperature, and stirred under argon overnight protected from light. Solvent was removed under vacuum, and the solid reconstituted in 0.5 N HCl (5 mL) and stirred for 15 min. The solution was filtered through a 0.2 µm Supor membrane Acrodisc syringe filter (Pall) and dialyzed against nanopure water until constant pH using a 15 mL Amicon Ultra 3 kDa spin filter (EMD Millipore), and lyophilized to yield CO_2H-PEG-nitroPBA (465 mg) as a white solid. ^1H NMR (600 MHz, DMSO-d_6): 12.52 (s - COOH, 1H), 8.90 (t, 1H), 8.73 (m, 1H), 8.69 (m, 1H), 8.65 (m, 1H), 8.61 (s, 2H), 4.00 (s, 2H), 3.53–3.46 (s - PEG). MALDI: 5496.0.

A similar procedure was followed using methoxy-PEG-amine (5 kDa, 500 mg, 1 equiv, JenKem) to synthesize OMe-PEG-nitroPBA. ^1H NMR (600 MHz, DMSO-d_6): 8.90 (t, 1H), 8.72 (m, 1H), 8.69 (m, 1H), 8.64 (m, 1H), 8.60 (s, 2H), 3.54–3.48 (s - PEG), 3.23 (s, 2H). MALDI: 5825.4.

Synthesis of Tf-PEG-nitroPBA. CO_2H-PEG-nitroPBA (16 mg, 25 equiv), EDC-HCl (6.1 mg, 250 equiv), and NHS (5.5 mg, 375 equiv) were dissolved in 0.1 M MES buffer, pH 6.0 (0.33 mL), and stirred for 15 min at room temperature. The reaction mixture was then added to a 0.5 mL Amicon Ultra 3 kDa spin filter (EMD Millipore), and centrifuged to isolate the activated nitroPBA-PEG-NHS ester. The ester was added to human holo-Tf (10 mg, 1 equiv, Sigma) dissolved in 0.1 M PBS, 0.15 M NaCl, pH 7.4 (1 mL). The reaction was lightly agitated for 2 h at room temperature, and then dialyzed against 0.1 M PBS, 0.15 M NaCl, pH 7.4 using 0.5 mL Amicon Ultra 50 kDa spin filters (EMD Millipore) to remove excess PEG. A portion of this solution was dialyzed into 10 mM PB, pH 7.4, and conjugation was verified by MALDI-TOF (autoflex speed TOF/TOF, Bruker) using a sinapinic acid matrix. MALDI-TOF: 85295.4. The amount of iron loaded to the Tf was verified by UV-VIS on a NanoDrop system (Thermo Scientific) using the ratio of A_{465}/A_{280}. This ratio was compared to that of the unreacted human holo-Tf, and a value ≥ 80% of the unreacted ratio confirmed adequate iron retention following synthesis steps. The remaining Tf-PEG-nitroPBA was formulated into PBS, pH 7.4, and stored at 4 ºC.

Preparation of Nanoparticles. Either OMe-PEG-nitroPBA or Tf-PEG-nitroPBA conjugates in PBS, pH 7.4 were added at 20x molar excess to MAP-CPT nanoparticles to form non-targeted and TfR-targeted MAP-CPT nanoparticles, respectively (20 OMe or Tf per particle). The solution was gently mixed by pipette, and allowed to equilibrate for 10 min. Nanoparticle formulations were filtered using a 0.45 µm PTFE membrane Millex-LH syringe filter (EMD Millipore).

Nanoparticle Characterization. Nanoparticles were characterized using a Brookhaven Instruments Corporation (BIC) ZetaPALS. Nanoparticles were diluted in PBS, pH 7.4 or PB, pH 5.5, and hydrodynamic diameter was measured by dynamic light scattering (DLS) using BIC Particle Sizing Software. Measurements were performed in solutions of different pH to allow for characterization under conditions where OMe-PEG-nitroPBA and Tf-PEG-nitroPBA conjugates would be bound to the vicinal diols on MAP (pH 7.4) and where nitroPBA conjugates would dissociate from the diols on MAP (pH 5.5). Particle formulations were diluted in 10 mM PB, pH 7.4 or 1 mM KCl, pH 5.5, and zeta potential was measured using BIC PALS Zeta Potential Analyzer software with a target residual of 0.02. Five runs were performed for both the nanoparticle diameter and zeta potential measurements.

Nanoparticle Transwell Assay. bEnd.3 cells were obtained from ATCC and maintained in Dulbecco's modified Eagle's medium (DMEM) supplemented with 10% (v/v) FBS and 1% penicillin/streptomycin in a humidified oven at 37 °C with 5% CO_2. Media was added to apical and basal wells of 12 mm polyester-coated Transwell supports (Corning), and allowed to equilibrate overnight at 37 ºC. Cells were added to the apical well at 82,500 cells/well. Media was replaced in the apical and basal wells every 2 days. Transepithelial electrical resistance (TEER) was measured in an Endohm chamber using an EVOM resistance meter (World Precision Instruments). Once TEER reached ≥ 30 Ohm·cm^2, transcytosis experiments were performed. Prior to introduction, both compartments of the Transwell were washed with serum-free DMEM, and allowed to equilibrate for 1 h. Nanoparticles were added at 1 µg of CPT/well to the apical well. After 8 h, the entire volume was removed from the basal well, and immediately frozen at -80 ºC until time for analysis. For the Tf-competition assay, the experiment was performed as described above using DMEM + 2.5 mg/mL Tf as the media in both apical and basal wells. For the high affinity anti-TfR coincubation assay, the nanoparticles were formulated with an equimolar (Tf:Ab) amount of R17217 anti-TfR Ab (Biolegend) in serum-free DMEM and added to the apical chamber.

The amount of CPT in the basal well was determined on an Agilent 1100 HPLC system with a reverse phase column (Synergi 4 µm Hydro-RP 80 Å, Phenomenex) connected to a fluorescence detector set to 370/440 nm (ex/em). 50% acetonitrile/50% potassium phosphate buffer (10 mM, pH 4) was used as the eluent at a flow rate of 0.5 mL/min. To cleave CPT from the MAP polymer, 13 µL of 0.1 N NaOH was added to 20 µL sample and incubated for 1 h. Then, 20 µL of 0.2 N HCl was added to convert the carboxylate CPT to the lactone form, followed by 30 min incubation. Subsequently, 147 µL methanol was added, and the mixture incubated for 2 h at room temperature for protein precipitation. The sample was centrifuged at 14000 g for 15 min and supernatant filtered using a 0.45 µm PTFE membrane Millex-LH syringe filter (EMD Millipore). CPT content was determined by injecting 100 µL of the filtered solution onto the column compared to a calibration curve of known concentrations of CPT. Reported values are the average of four wells per group. The error shown is standard error of the mean. Pairwise group comparisons testing for statistically significant differences were performed using the Wilcoxon-Mann-Whitney test in MATLAB.

Antitumor Efficacy in IC, ICD, and IV Brain Metastasis Models.

IC, ICD and IV Tumor Models. All animals were treated according to the NIH guidelines for animal care and use as approved by the Caltech Institutional Animal Care and Use Committee. BT474-Gluc cells, transduced with an expression cassette encoding Gluc and CFP separated by an internal ribosomal entry site using a lentiviral vector, were obtained from Dr. Jain at Harvard University. BT474-Gluc cells were maintained in RPMI 1640 supplemented with 10% (v/v) FBS in a humidified oven at 37 °C with 5% CO_2. For the IC model, 50,000 BT474-Gluc cells in 2 µL RPMI were intracranially injected into the right cerebral hemisphere of female $Rag2^{-/-}$;$Il2rg^{-/-}$ mice (Jackson Laboratory) using a stereotaxic apparatus at a rate of 0.1 µL/min. The coordinates for injection were 2 mm posterior, 1.5 mm lateral to bregma, and 2.5 mm depth from bregma. For the ICD model, 100,000 BT474-Gluc cells were suspended in 100 µL of RPMI and slowly injected into the left ventricle of female $Rag2^{-/-}$;$Il2rg^{-/-}$ mice. Injections were performed blind, midway between the sternal notch and top of xyphoid process, and 13% anatomical left of sternum. Successful insertion into the left cardiac ventricle was confirmed by a bright red pulse of blood in the syringe. For the IV model, 2 M cells were suspended in 150 µL RPMI and slowly injected into the lateral tail vein of restrained female Rag2$^{-/-}$;Il2rg$^{-/-}$ mice.

Tumor Size Monitoring. For ICD and IV models, formation of BT474-Gluc brain metastatic tumors was monitored by MRI on a 11.7-T magnet every third week until macroscopic tumors were visible (~0.2 mm^3 in volume). Tumor growth was then monitored weekly by MRI, as for the IC model. Mice were anaesthetized with 1.5–2% (v/v) isoflurane in O_2 at a flow rate of 1–1.5 mL/min. T2-weighted 3D RARE images were acquired to assess the tumor volume. The image acquisition parameters were as follows: echo time: 6.1 ms; repetition time: 250 ms; rapid acquisition relaxation enhanced (RARE) factor: 4; number of averages: 4; field of view: 2.0 cm x 1.2 cm x 0.8 cm; matrix: 200 x 120 x 80 (100 µm isotropic resolution). Tumor volume was determined manually from the T2 hyperintense tumor regions of the brain using Fiji software. For the IC model, tumor size was also monitored by measuring the activity of secreted Gluc in the blood. 20 µL of blood was collected weekly from the saphenous vein, mixed with 5 µL of 50 mM EDTA, and immediately frozen at -20 ºC until time for analysis. Blood was transferred to an opaque 96-well plate (Nunc), and Gluc activity measured using the Pierce Gaussia Luciferase Flash Assay Kit, according to the manufacturer's protocol. Photon counts were acquired for 5 s following addition of coelenterazine using a Safire 2 multi-mode plate reader (Tecan). Pairwise group comparisons testing for statistically significant differences were performed using the Wilcoxon-Mann-Whitney test in MATLAB.

Treatments. Treatment began when brain metastatic tumors reached ~2 mm^3, as measured by MRI. Mice in each model were randomized into four groups of six mice per group. CPT, non-targeted MAP-CPT nanoparticles, and TfR-targeted MAP-CPT nanoparticles were freshly prepared. The different formulations were systemically administered by lateral tail vein injection once per week for 4 weeks at a dose of 4 mg/kg (CPT basis). Injections were standardized to 150 µL per 20 g body weight. CPT is highly insoluble in aqueous solutions; therefore, it was dissolved in a solution containing 20% DMSO, 20% PEG 400, 30% ethanol, and 30% 10 mM pH 3.5 phosphoric acid. Nanoparticle treatments were prepared and administered in PBS, pH 7.4 as previously described. The control treatment was 0.9% (w/v) saline.

No gross signs of toxicity were observed from either the non-targeted or the targeted nanoparticles in our study, while animals did have reactions to dosing with the CPT alone. These reactions are common and documented in the literature for CPT (23,24).

Measurement of CPT Concentration in Brain. Eight weeks after the beginning of the treatment, four of six mice per treatment group were systemically administered by lateral tail vein injection one additional dose at 4 mg/kg (CPT basis). After 24 h, the mice were anaesthetized and transcardially perfused with PBS, pH 7.4. Brain tumors were collected and sectioned into two approximately equal sized pieces. An equally sized piece of healthy brain tissue was collected from the brain region contralateral to the tumor location. One piece of the tumor and the healthy tissue were weighed and placed in separate Lysing Matrix A tubes containing ¼ inch ceramic spheres (MP Biomedicals) in RIPA buffer (Cell Signaling Technologies) at a fixed ratio (w/v). Tissues were homogenized using a

FastPrep-24 homogenizer (MP Biomedicals) at a rate of 6 m/s for 30 s. A total of three homogenization steps occurred with a 1 min rest on ice between steps. After the final homogenization step, samples were rotated for 30 min, then centrifuged at 14000 g for 15 min at 4 ºC. The supernatant was collected, and immediately frozen at -80 ºC until time for analysis. CPT uptake into tumor and healthy brain tissue for each formulation was determined by HPLC, as described above. Pairwise group comparisons testing for statistically significant differences were performed using the Wilcoxon-Mann-Whitney test in MATLAB.

Brain Metastatic Tumor Cell Isolation and Cytotoxicity Assay. The second piece of brain tumor tissue was immediately minced ice cold RPMI, and incubated in RPMI supplemented with 10% (v/v) FBS, 1% penicillin/streptomycin and 1 mg/mL collagenase/dispase enzyme mix (Roche) at 37 °C for 1 h with shaking. The tissue was then centrifuged at 300 g for 5 min, and supernatant removed. The pellet was resuspended in RPMI supplemented with 10% (v/v) FBS and 1% penicillin/streptomycin, and the cells cultured in a humidified oven at 37 °C with 5% CO_2. Media was refreshed after 24 h, and every 2 days thereafter. After 1 week, the majority of the cells were BT474-Gluc tumor cells, as identified by CFP.

BT474-Gluc cells dissociated from the brain parenchyma, as well as parental cells, were seeded at a density of 3,000 cells/well in 96-well plates. After 24 h, media was removed and replaced with fresh media containing different concentrations of CPT. After 72 h, BT474-Gluc cell viability was measured using the CellTiter 96 Aqueous One Solution cell proliferation assay (Promega) on an Infinite M200 microplate reader (Tecan), according to the manufacturer’s protocol.

3.6 References

1. Chen Y, Liu L (2012) Modern methods for delivery of drugs across the blood-brain barrier. *Advanced Drug Delivery Reviews* 64(7):640-665.

2. Pardridge WM (2017) Delivery of biologics across the blood-brain barrier with molecular trojan horse technology. *BioDrugs* 31(6):503-519.

3. Uchida Y, et al. (2011) Quantitative targeted absolute proteomics of human blood-brain barrier transporters and receptors. *Journal of Neurochemistry* 117(2):333–345.

4. Widera A, Norouziyan F, Shen WC (2003) Mechanisms of TfR-mediated transcytosis and sorting in epithelial cells and applications toward drug delivery. *Advanced Drug Delivery Reviews* 55(11):1439–1466.

5. Lajoie JM, Shusta EV (2015) Targeting receptor-mediated transport for delivery of biologics across the blood-brain barrier. *Annual Review of Pharmacology and Toxicology* 55:613-631.

6. Yu YJ, et al. (2011) Boosting brain uptake of a therapeutic antibody by reducing its affinity for a transcytosis target. *Science Translational Medicine* 3(84):84ra44.

7. Bien-Ly N, et al. (2014) Transferrin receptor (TfR) trafficking determines brain uptake of TfR antibody affinity variants. *Journal of Experimental Medicine* 211(2):233-244.

8. Niewoehner J, et al. (2014) Increased brain penetration and potency of a therapeutic antibody using a monovalent molecular shuttle. *Neuron* 81(1):49–60.

9. Sade H, et al. (2014) A human blood-brain barrier transcytosis assay reveals antibody transcytosis influenced by pH-dependent receptor binding. *PLoS One* 9(4):e96340.

10. Couch JA, et al. (2013) Addressing safety liabilities of TfR bispecific antibodies that cross the blood-brain barrier. *Science Translational Medicine* 5(183):183ra57.

11. Yu YJ, et al. (2014) Therapeutic bispecific antibodies cross the blood-brain barrier in nonhuman primates. *Science Translational Medicine* 6(261):261ra154.

12. Wiley DT, Webster P, Gale A, Davis ME (2013) Transcytosis and brain uptake of transferrin-containing nanoparticles by tuning avidity to transferrin receptor. *Proceedings of the National Academy of Sciences USA* 110(21):8662-8667.

13. Kamaly N, Xiao Z, Valencia PM, Radovic-Moreno AF, Farokhzad OC (2012) Targeted polymeric therapeutic nanoparticles: design, development and clinical translation. *Chemical Society Reviews* 41(7):2971-3010.

14. Clark AJ, Davis ME (2015) Increased brain uptake of targeted nanoparticles by adding an acid-cleavable linkage between transferrin and the nanoparticle core. *Proceedings of the National Academy of Sciences USA* 112(40):12486-12491.

15. Mellman I (1996) Endocytosis and molecular sorting. *Annu Rev Cell Dev Biol* 12:575-625.

16. Han H, Davis ME (2013) Targeted nanoparticles assembled via complexation of boronic-acid-containing targeting moieties to diol-containing polymers. *Bioconjugate Chemistry* 24(4):669-677.

17. Han H, Davis ME (2013) Single-antibody, targeted nanoparticle delivery of camptothecin. *Molecular Pharmaceutics* 10(7):2558-2567.

18. Nance EA, et al. (2012) A dense poly(ethylene glycol) coating improves penetration of large polymeric nanoparticles within brain tissue. *Science Translational Medicine* 4(149):149ra119.

19. Brown RC, Morris AP, O'Neil RG (2007) Tight junction protein expression and barrier properties of immortalized mouse brain microvessel endothelial cells. *Brain Research* 1130(1):17-30.

20. Chung E, et al. (2009) Secreted Gaussia luciferase as a biomarker for monitoring tumor progression and treatment response of systemic metastases. *PLoS One* 4(12):e8316.

21. Nanni P, et al. (2012) Multiorgan metastasis of human HER-2^{+} breast cancer in Rag2$^{-/-}$;Il2rg$^{-/-}$ mice and treatment with PI3K inhibitor. *PLoS ONE* 7(6):e39626.

22. Committee on care and use of laboratory animals (1996) *Guide for the care and use of laboratory animals* (Natl Inst Health, Bethesda), DHHS Publ No (NIH) 85-23.

23. Moertel CG, Schutt AJ, Reitemeier RJ, Hahn RG (1972) Phase II study of camptothecin (NSC-100880) in the treatment of advanced gastrointestinal cancer. *Cancer Chemotherapy Reports* 56(1):95–101.

24. Muggia FM, Creaven PJ, Hansen HH, Cohen MH, Selawry OS (1972) Phase I clinical trial of weekly and daily treatment with camptothecin (NSC-100880): correlation with preclinical studies. *Cancer Chemotherapy Reports* 56(4):515–521.

Chapter IV

OVERALL SUMMARY AND CONCLUSIONS

HER2 overexpression is observed in about 25% of human breast cancers, and is associated with increased aggressiveness of the tumor as well as poor patient prognosis (1). Treatment with HER2-targeted therapeutics such as trastuzumab has improved clinical outcomes in these patients, but also unveiled a new challenge to their long term survival – brain metastases (2,3). As many as half of patients with HER2-positive, metastatic disease will develop brain metastases over the course of their disease (4). Like most brain diseases, brain metastases are largely untreatable due to the inability of most therapeutics to cross the BBB/BTB from circulation and enter the brain (4,5). Approaches to overcome limited drug delivery to the brain have the potential to elicit more durable responses in these patients and offer a much needed glimmer of hope for many others suffering from a range of brain diseases.

One promising strategy to increase brain uptake of therapeutics in circulation is to exploit endogenous transport systems at the BBB to shuttle drugs into the brain. Of the transport mechanisms at the BBB, only the transcytosis pathway is compatible with delivery of a wide variety of therapeutics, including small molecules, macromolecules, and nanoparticles (6). The “Trojan-horse” approach of attaching therapeutic agents to ligands that bind a transyctosing receptor was proposed decades ago (5), and has been actively explored for TfR at the BBB (7,8). Despite several decades of investigation of Abs targeted to TfR (9-19), no viable clinical candidates have emerged. Two main limiting factors have hindered their successful translation to the clinic: (i) lysosomal sequestration of high-affinity anti-TfR Abs (14) and (ii) the need for very high systemic doses of lower-affinity variants to achieve sufficient brain accumulation (12).

Using AuNPs as a model system, our group investigated whether TfR-targeted nanoparticles were similarly restricted at the BBB and found that brain uptake of high-avidity AuNPs was limited in a similar way to high-affinity Abs (20). Follow-up work showed that high-avidity, TfR-targeted AuNPs could be made capable of accumulating in the brain in high numbers using acid-cleavable targeting ligands (21). Nanoparticles were chosen for their ability to be loaded with large quantities of drug that can be released at a tunable rate (22). The primary goal of this work was to determine whether therapeutic-containing polymeric nanoparticles targeted to TfR using this methodology could be prepared to deliver a pharmacologically active amount of drug across the BBB/BTB. Initially focusing on drug delivery to HER2-positive breast cancer brain metastases, we addressed two important aspects of developing and translating new therapies.

First, we addressed the pressing ‘mouse-to-human’ translational challenge facing the drug development community (23,24). We developed a new murine model of HER2-positive breast cancer brain metastasis that involves IV injection of human breast cancer cells in an attempt to create a clinically representative, impermeable BBB/BTB to standard therapeutics. We compared this new model to two types of models from the literature that involve IC or ICD injection of the cancer cells, and demonstrated that the method – IC, ICD, or IV administration of HER2-positive breast cancer cells – used for creating brain metastases can have an impact not only on the evolution of the brain tumor, but also on its uptake of and response to therapeutics. Our results show that IC-formed brain tumors permit significant penetration of non-BBB-permeable therapeutics, whereas ICD- and IV-formed brain tumors maintain a more intact BBB/BTB. These findings suggest that the IC model must be used with caution for translational research where a non-permissive BBB is clinically relevant, particularly if the experimenter is interested in understanding therapeutic brain penetration (25).

Second, we demonstrated a methodology for delivery of a small molecule drug across the BBB/BTB to breast cancer brain metastases in mice. We prepared TfR-targeted, single-agent therapeutic nanoparticles with acid-cleavable targeting ligands, and observed that treatment with these targeted nanoparticles led to a marked delay in tumor progression as well as high accumulation in brain tumors across all three murine models. Furthermore, TfR-targeted nanoparticles showed significant penetration in healthy brain tissue that resulted in whole-brain penetration, validating the therapeutic potential of the delivery system (25).

In summary, this work details the development of a new mouse model of HER2-positive breast cancer brain metastasis with high clinical relevance, enabling more meaningful translational studies of therapeutic brain penetration. It also presents the design, development and investigation of TfR-targeted, therapeutic nanoparticles capable of crossing the BBB/BTB using acid-cleavable targeting ligands. These TfR-targeted, polymeric nanoparticles can effectively deliver a small molecule therapeutic to the brain, and have tremendous potential in treating brain metastases as well as other brain diseases.

4.1 References

1. Slamon DJ, Clark GM, Wong SG, Levin WJ, Ullrich A, McGuire WL (1987) Human breast cancer: Correlation of relapse and survival with amplification of the HER-2/*neu* oncogene. *Science* 235(4785):177–182.

2. Lin NU, Winer EP (2007) Brain metastases: The HER2 paradigm. *Clinical Cancer Research* 13(6):1648–1655.

3. Chien AJ, Rugo HS (2013) Emerging treatment options for the management of brain metastases in patients with HER2-positive metastatic breast cancer. *Breast Cancer Research and Treatment* 137(1):1–12.

4. Ramakrishna N, et al. (2014) Recommendations on disease management for patients with advanced human epidermal growth factor receptor 2-positive breast cancer and brain metastases: American Society of Clinical Oncology clinical practice guideline. *Journal of Clinical Oncology* 32(19):2100–2108.

5. Pardridge WM (2004). The blood-brain barrier: bottleneck in brain drug development. *NeuroRx* 2(1):3–14.

6. Abbott NJ, Patabendige AAK, Dolman DEM, Yusof SR, Begley DJ (2010) Structure and function of the blood–brain barrier. *Neurobiology of Disease* 37(1):13–25.

7. Freskgård P-O, Urich E (2017) Antibody therapies in CNS diseases. *Neuropharacology* 120:38–55.

8. Widera A, Norouziyan F, Shen WC (2003) Mechanisms of TfR-mediated transcytosis and sorting in epithelial cells and applications toward drug delivery. *Advanced Drug Delivery Reviews* 55(11):1439–1466.

9. Friden PM, Walus LR, Musso GF, Taylor MA, Malfroy B, Starzyk RM (1991) Anti-transferrin receptor antibody and antibody-drug conjugates cross the blood-brain barrier. *Proceedings of the National Academy of Sciences USA* 88(11):4771–4775.

10. Pardridge WM, Buciak JL, Friden PM (1991) Selective transport of an anti-transferrin receptor antibody through the blood–brain barrier in vivo. *Journal of Pharmacology and Experimental Therapeutics* 259(1):66–70.

11. Moos T, Morgan EH (2001) Restricted transport of anti-transferrin receptor antibody (OX26) through the blood–brain barrier in the rat. *Journal of Neurochemistry* 79(1):119–129.

12. Yu YJ, Zhang Y, Kenrick M, Hoyte K, Luk W, et al. (2011) Boosting brain uptake of a therapeutic antibody by reducing its affinity for a transcytosis target. *Science Translational Medicine* 3(84):84ra44.

13. Couch JA, et al. (2013) Addressing safety liabilities of TfR bispecific antibodies that cross the blood-brain barrier. Sci Transl Med 5(183):183ra57.

14. Bien-Ly N, Yu YJ, Bumbaca D, Elstrott J, Boswell CA, et al. (2014) Transferrin receptor (TfR) trafficking determines brain uptake of TfR antibody affinity variants. *The Journal of Experimental Medicine* 211(2):233–244.

15. Niewoehner J, Bohrmann B, Collin L, Urich E, Sade H, et al. (2014) Increased brain penetration and potency of a therapeutic antibody using a monovalent molecular shuttle. *Neuron* 81(1):49–60.

16. Sade H, Baumgartner C, Hugenmatter A, Moessner E, Freskgård P-O, Niewoehner J (2014) A human blood-brain barrier transcytosis assay reveals antibody transcytosis influenced by pH-dependent receptor binding. *PLoS One* 9(4):e96340.

17. Yu YJ, et al. (2014) Therapeutic bispecific antibodies cross the blood-brain barrier in nonhuman primates. *Sci Transl Med* 6(261):261ra154.

18. Lajoie JM, Shusta EV (2015) Targeting receptor-mediated transport for delivery of biologics across the blood-brain barrier. *Annual Review of Pharmacology and Toxicology* 55:613–631.

19. Villaseñor R, Schilling M, Sundaresan J, Lutz Y, Collin L (2017) Sorting tubules regulate blood-brain barrier transcytosis. *Cell Reports* 21(11):3256–3270.

20. Wiley DT, Webster P, Gale A, Davis ME (2013) Transcytosis and brain uptake of transferrin-containing nanoparticles by tuning avidity to transferrin receptor. *Proceedings of the National Academy of Sciences USA* 110(21):8662–8667.

21. Clark AJ, Davis ME (2015) Increased brain uptake of targeted nanoparticles by adding an acid-cleavable linkage between transferrin and the nanoparticle core. *Proceedings of the National Academy of Sciences USA* 112(40):12486–12491.

22. Kamaly N, Xiao Z, Valencia PM, Radovic-Moreno AF, Farokhzad OC (2012) Targeted polymeric therapeutic nanoparticles: design, development and clinical translation. *Chemical Society Reviews* 41(7):2971–3010.

23. McGonigle P, Ruggeri B (2014) Animal models of human disease: challenges in enabling translation. *Biochemical Pharmacology* 87(1):162–171.

24. Mak IW, Evaniew N, Ghert M (2014) Lost in translation: animal models and clinical trials in cancer research. *American Journal of Translational Research* 6(2):114–118.

25. Wyatt EA, Davis ME (2018) Method of establishing breast cancer brain metastases affects brain uptake and efficacy of targeted, therapeutic nanoparticles. *Bioengineering and Translational Medicine* 1–8.

Appendix A

DEVELOPMENT OF LAPATINIB-LOADED MUCIC ACID POLYMER NANOPARTICLES FOR DELIVERY TO BREAST CANCER BRAIN METASTASES

A.1 Preamble

The ultimate goal of our work is to develop targeted nanoparticles that are able to cross the BBB/BTB and effectively deliver combinations of therapeutic agents to intracranial cancers. As previously mentioned, we believe that TfR-targeted nanoparticles delivering therapeutic agents with greater potency may elicit a stronger antitumor response than was observed for the MAP-CPT nanoparticles. To this end, we investigated the incorporation of a more potent HER2-targeted small molecule agent, lapatinib, into the MAP polymer delivery system. As a targeted cancer therapy, lapatinib may enable more significant tumor knockdown, while maintaining a safer toxicity profile following whole-brain distribution relative to a standard chemotherapeutic. The following is development work completed towards this objective, performed in parallel with the investigation of MAP nanoparticles as shuttles for macromolecular therapeutic agents detailed in Chapter III.

A.2 Introduction

HER2-positive, metastatic breast cancer eventually becomes resistant to trastuzumab (1,2), and in some patients the cancer recurs after adjuvant therapy (3,4), often with the development of brain metastases (5-7). Poor penetration of HER2-targeted agents through the BBB and BTB limits improvement of clinical outcomes. For these reasons, there is a need for alternative treatment strategies to increase the brain uptake of therapeutics that block the HER2 signaling pathway.

Lapatinib is an orally active small molecule that inhibits the tyrosine kinases of HER2 and epidermal growth factor receptor type 1 (EGFR) (8). Lapatinib was approved for use in combination with capecitabine by the FDA in 2007 for the treatment of metastatic, HER2-positive breast cancer that has progressed with standard treatment (9). The approval followed the results of a pivotal trial comparing combination lapatinib and capecitabine versus capecitabine alone in HER2-positive, metastatic breast cancer patients previously treated with anthracycline, taxane, and trastuzumab treatment (10,11). Patients in the combination group, when compared to those on capecitabine alone, showed an improvement in response rate and progression-free survival (PFS) by 4 months (8.4 vs. 4.4 months) (10).

In addition to combination with cytotoxic agents, there is interest in lapatinib combination therapy with trastuzumab for patients with advanced HER2-positive breast cancer. Dual targeting of HER2-positive breast cancer tumors with lapatinib and trastuzumab has garnered interest for several reasons, including their: (i) non-overlapping mechanisms of action, and (ii) potential synergistic effects, as demonstrated in preclinical breast cancer models (12-14). In a clinical setting, trastuzumab inhibits ligand-independent HER2 signaling, but also induces apoptosis though antibody-dependent cellular cytotoxicity (ADCC) (15,16). In contrast, lapatinib inhibits ligand-dependent signaling and blocks downstream MAPK and PI3K signaling to prevent cell proliferation and survival (17). Additionally, lapatinib can induce accumulation of HER2 on the cell surface, potentiating trastuzumab-dependent ADCC (14). Furthermore, a clinical study comparing combination lapatinib and trastuzumab versus lapatinib alone in metastatic, HER2-positive breast cancer patients with trastuzumab-refractory disease showed improved PFS when compared to lapatinib alone (12.0 vs. 8.1 weeks) (18).

Because of its low molecular weight and lipophilic nature, it has been suggested that, in contrast to trastuzumab, lapatinib may cross the BBB. However, a positron emission tomography (PET) study performed using carbon-11 radiolabeled lapatinib ([^{11}C]lapatinib) showed a consistent lack of uptake in healthy brain tissue in patients with and without brain metastases (19). Furthermore, brain metastases in this PET study showed a modest, but highly variable uptake of [^{11}C]lapatinib. These results are consistent with clinical data that showed a 60-fold variability in lapatinib uptake in brain metastases resected from patients after oral lapatinib treatment and preclinical studies in mice (20,21). Additionally, brain metastases at their earliest stages, where one may expect to have the greatest change of effective treatment, are hidden behind an intact BBB. By the time that these tumors grow to sufficient size to begin to demonstrate some partial BBB permeability (19,20), it likely may be too late to achieve effective therapy.

The goal of this work was to prepare TfR-targeted, lapatinib-loaded nanoparticles for future use as a single-agent therapeutic or in combination with trastuzumab assembled on the nanoparticle surface (Fig. A.1). Here, we synthesize two modified MAP polymer scaffolds that are used to prepare urea- and carbamate-based lapatinib polymer-drug conjugates that allow for the assembly of TfR-targeted, lapatinib-loaded nanoparticles. Ureas and carbamates are commonly used in medicinal chemistry, particularly in many prodrugs – chemically modified forms of a pharmacologically active agent that undergo *in vivo* modification to release the native drug molecule (22-24). The prodrug strategy helps to mitigate a number of challenges in achieving suitable physiochemical or pharmacokinetic drug properties, such as poor aqueous solubility, rapid clearance, and toxicity (25). Typically, release of the active drug molecule requires a triggering condition, such as a change in pH or presence of an enzyme. Most pharmacologically relevant urea and carbamate prodrugs have been designed as substrates of particular enzymes, including the previously mentioned small molecule capecitabine, a carbamate prodrug of 5-fluororacil that requires three enzymes for conversion to the active drug (26,27). Whether these types of linkages can be used to release lapatinib under physiologic conditions in the brain remains to be determined.

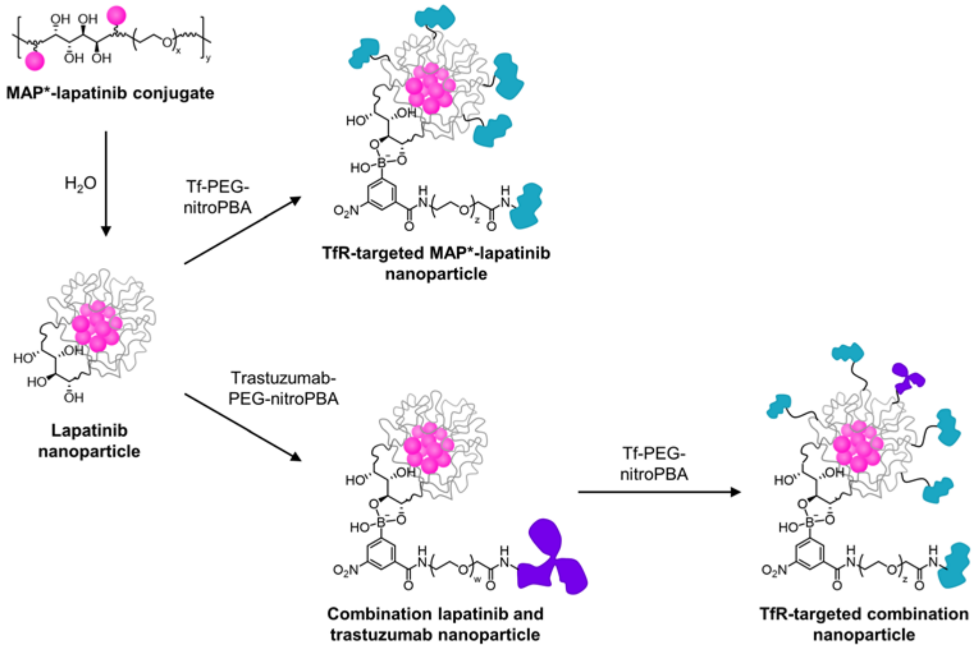

Fig. A.1. Preparation of TfR-targeted, MAP*-lapatinib or combination lapatinib and trastuzumab nanoparticles. x ~ 82 for 3.4kDa PEG; y ~ 20 for material used in this study; z ~ 120 for 5kDa PEG; w ~ 84 for 3.5 kDa PEG. MAP* denotes MAP derivative.

A.3 Results and discussion

A.3.1 Lapatinib displays increased *in vitro* cytotoxicity in HER2-positive BT474-Gluc cells when compared to CPT

An *in vitro* cytotoxicity assay was performed using the HER2-positive BT474-Gluc human breast cancer cell line to determine the sensitivity of the tumor cells to lapatinib. Cells were incubated with media containing increasing concentrations of lapatinib or CPT. After 72 h of incubation, sensitivity of the BT474-Gluc cells to the small molecule agents was determined using a commonly used cell proliferation assay (28). Untreated cells were used as controls.

Lapatinib showed significantly higher cytotoxicity against BT474-Gluc cells when compared to CPT, consistent with its greater expected potency (Fig. A.2). The IC_{50} value for lapatinib was nearly 3-fold lower than that for CPT (ca. 120 µM and 45 µM, respectively). These data suggest that TfR-targeted MAP nanoparticle delivery of lapatinib to brain metastatic BT474-Gluc tumors may give rise to greater antitumor activity *in vivo* than was observed for CPT.

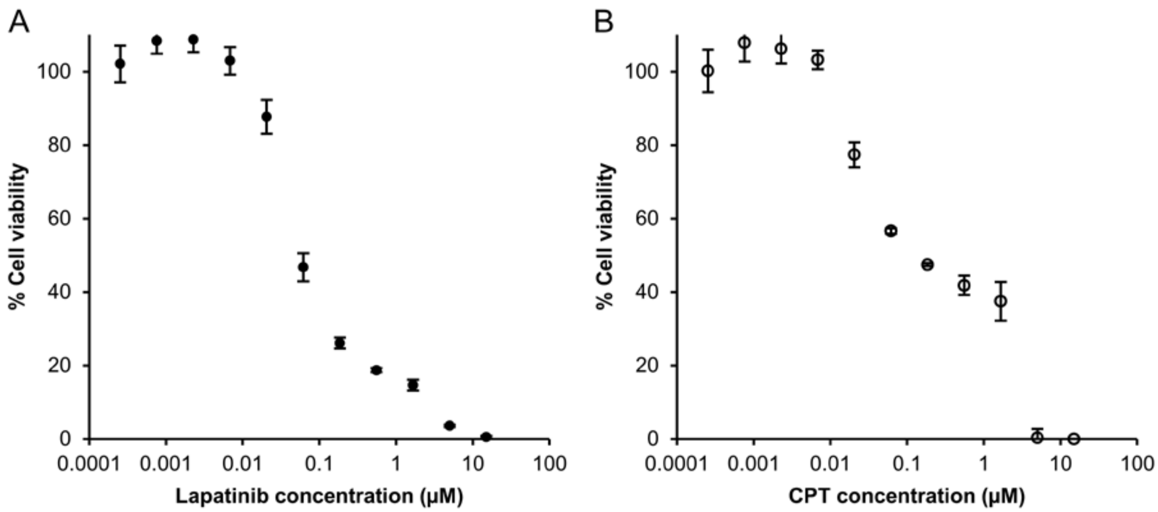

Fig. A.2. Lapatinib shows greater cytotoxicity against BT474-Gluc cells relative to CPT. Data shown are the average of 4 dose-response curves for lapatinib (**A**) and CPT (**B**). Error bars indicate SE.

A.3.2 Synthesis of MAP-amidoethanamine and MAP-amidoethanol polymer scaffolds for lapatinib conjugation

A number of conjugation strategies can be applied to synthesize polymer-drug conjugates (Fig. A.3). However, the chemical linkage must allow lapatinib to release from the polymer backbone under extracellular conditions within the brain once the nanoparticle has transcytosed the BBB/BTB. For this reason, highly stable amides are not compatible for this application. Additionally, lapatinib has limited functional groups available for conjugation to the polymer, containing only secondary amines in its native state that can potentially be used to couple the drug to the MAP polymer (Fig. A.4). Thus, esters that require the presence of a hydroxyl group – as was used in the synthesis of the MAP-CPT conjugate (1) – and imines that require the availability of a primary amine, were also ruled out. The most promising approaches remaining were the formation of either a urea or carbamate linkage between the secondary amine of lapatinib and the MAP polymer that is generally more susceptible to hydrolysis than amides (29). To achieve this, MAP needed to be modified to contain either a primary amine or hydroxyl functional handle, respectively (Fig. A.5).

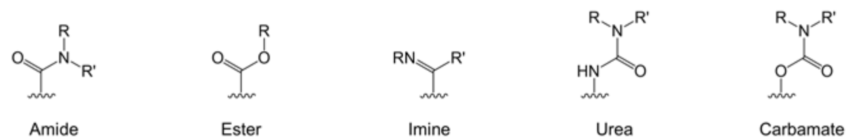

Fig. A.3. Common chemical linkages used in synthesis of conjugates.

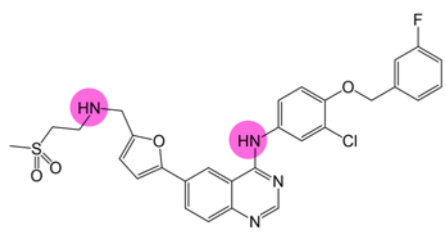

Fig. A.4. Structure of lapatinib. Lapatinib contains only secondary amine moieties (magenta) that can be used for conjugation to the polymer.

Fig. A.5. Urea and carbamate formation between lapatinib and modified MAP polymer. Secondary amines on lapatinib can be used to form a urea (**A**) or carbamate (**B**) bond with MAP that is modified to contain accessible amine or hydroxyl moieties. MAP* and MAP† denote these MAP derivatives.

N-Boc-ethylenediamine was added to MAP, followed by acid deprotection to yield MAP-amidoethanamine (Fig A.6A). Similarly, in a separate synthesis, 2-(benzyloxy)-ethan-1-amine was added to MAP, followed by deprotection using hydrogenation to yield MAP-amidoethanol (Fig. A.6B). *Tert*-butyloxycarbonyl (*tert*-Boc) and benzyl protecting groups were used to prevent crosslinking of the MAP polymer during the reaction. These modifications converted the carboxylic acid groups of MAP to amine or hydroxyl moieties to allow subsequent addition of lapatinib to the polymer through either a urea or carbamate bond, respectively. The MAP, *N*-Boc-ethylenediamine, 2-(benzyloxy)ethan-1-amine and intermediate reaction products leading to the preparation of MAP-amidoethanamine and MAP-amidoethanol were fully characterized by NMR (Fig. A.7 to A.13). The amine content in the MAP-amidoethanamine, as determined by a TNBSA assay, was 74%.

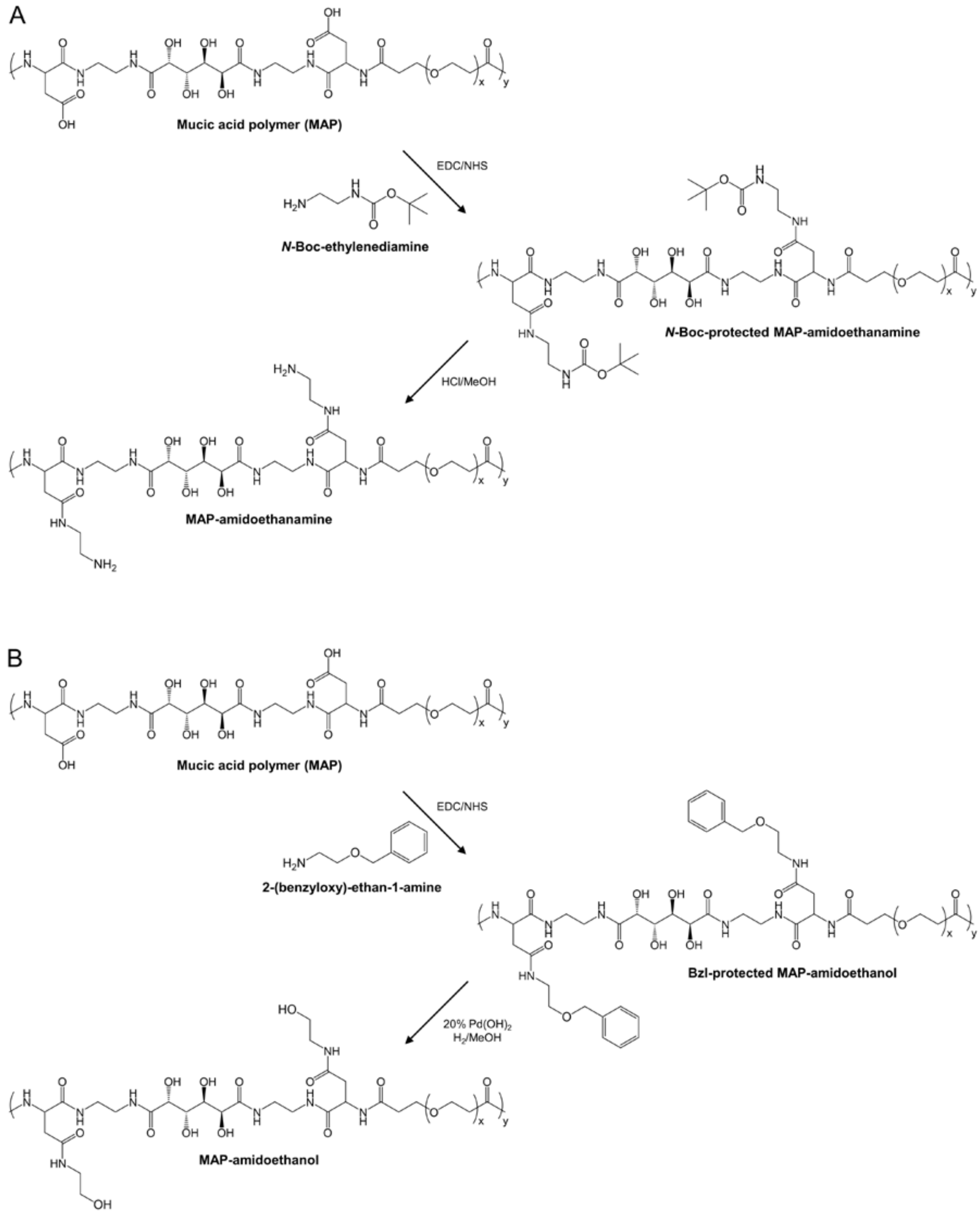

Fig. A.6. Synthesis of modified MAP polymer scaffolds to allow addition of lapatinib. (**A**) MAP-amidoethanamine. (**B**) MAP-amidoethanol. x ~ 82 for 3.4kDa PEG; y ~ 20 for material used in this study.

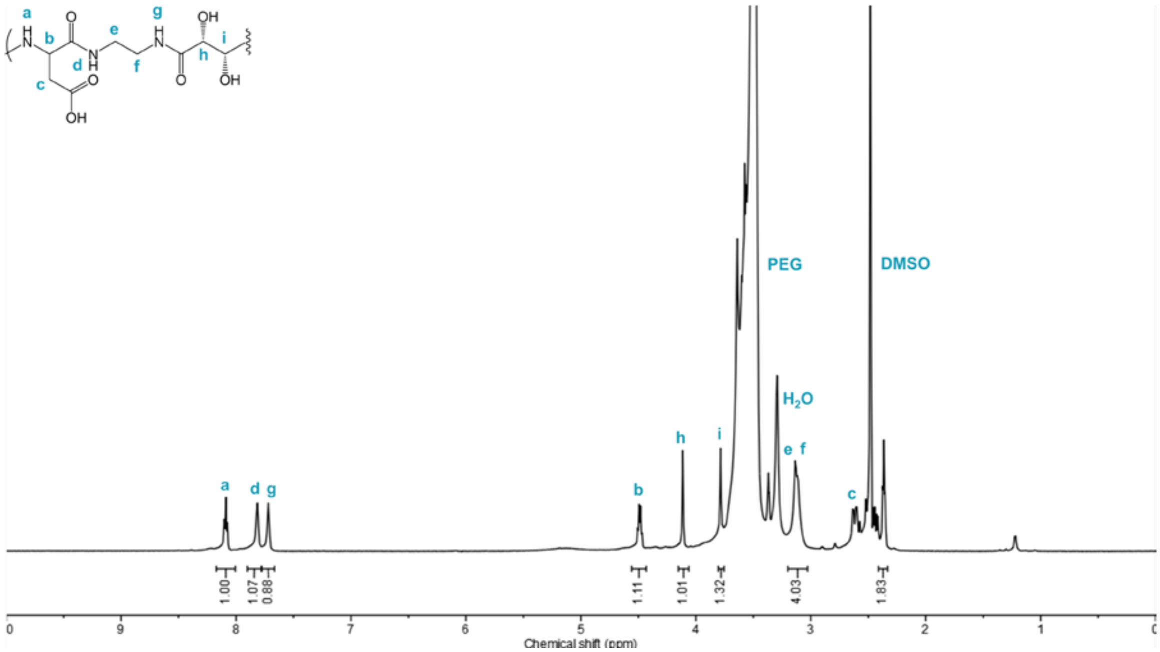

Fig. A.7. [1]H NMR of unmodified MAP. Lowercase letters (a–i) shown above peaks correspond to chemical shifts of protons indicated on the chemical structure.

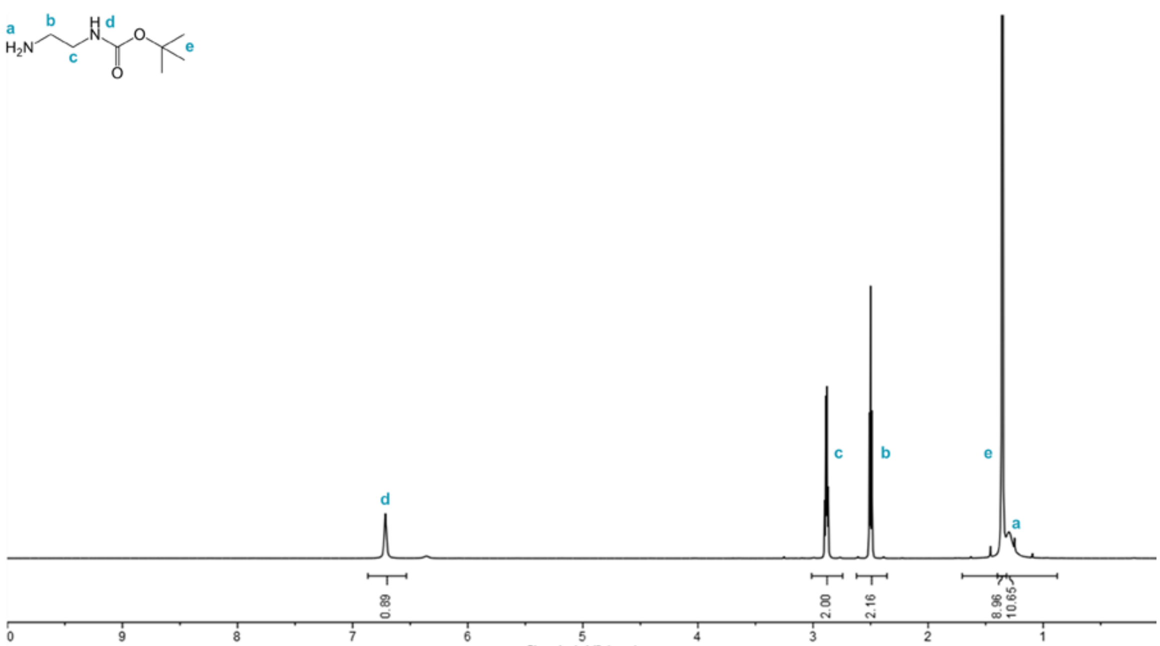

Fig. A.8. [1]H NMR of *N*-Boc-ethylenediamine. Lowercase letters (a–e) shown above peaks correspond to chemical shifts of protons indicated on the chemical structure.

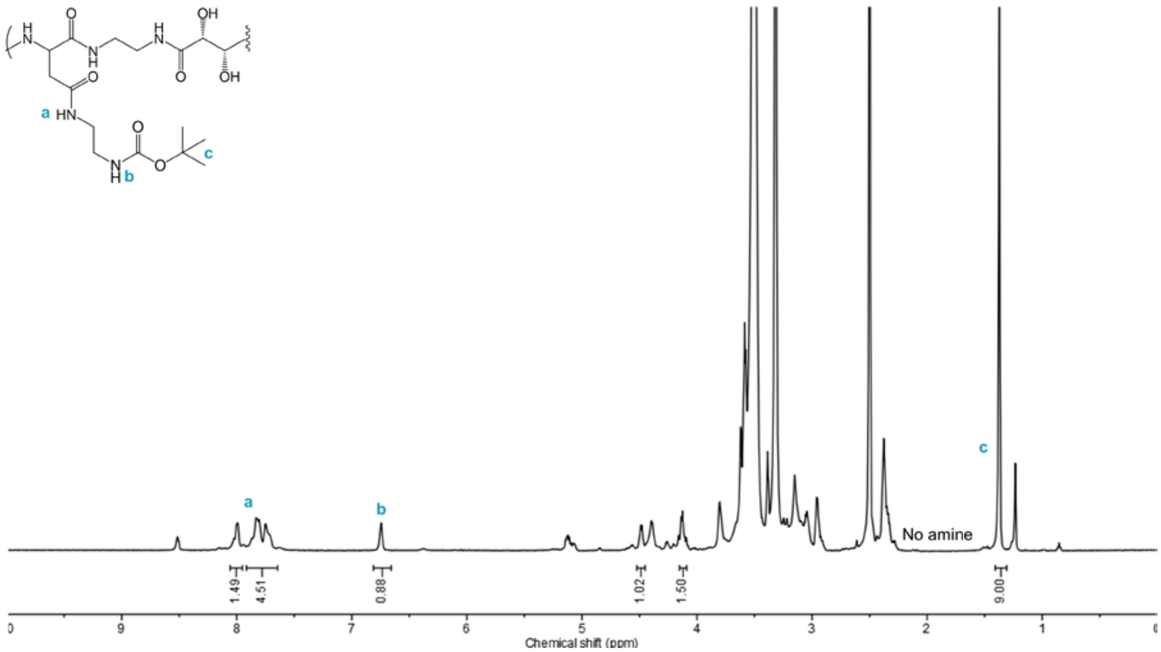

Fig. A.9. ^{1}H NMR of *N*-Boc-protected MAP-amidoethanamine. Peaks from amide adjacent to *tert*-Boc protecting group (b) and *tert*-Boc (c) are both present in the purified MAP-amidoethanamine intermediate, along with an additional amide (a) peak and no unreacted amine.

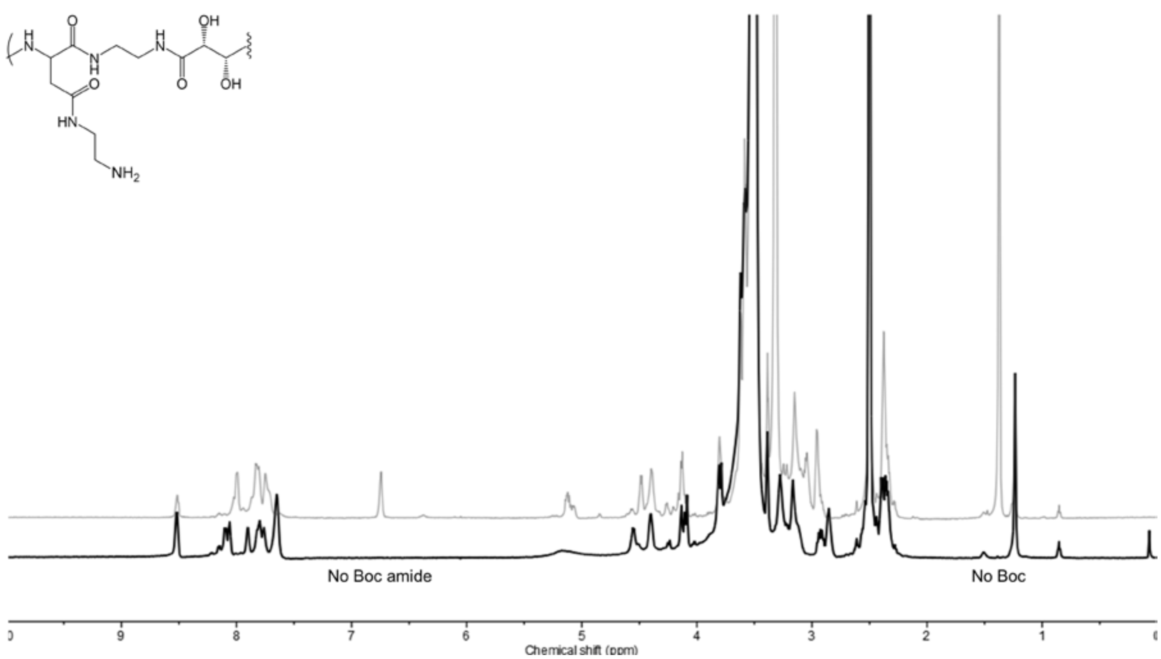

Fig. A.10. ^{1}H NMR of MAP-amidoethanamine (black trace) compared that before deprotection (gray trace). Peaks from *tert*-Boc protecting group and adjacent amide are no longer present.

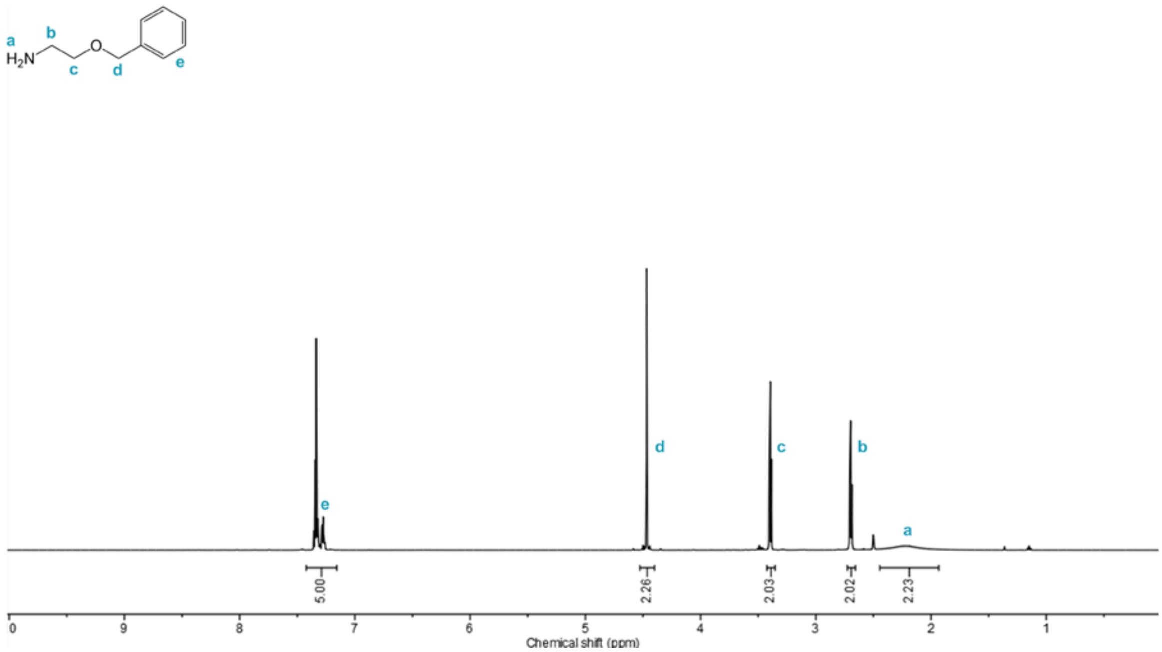

Fig. A.11. ^{1}H NMR of 2-(benzyloxy)ethan-1-amine. Lowercase letters (a–e) shown above peaks correspond to chemical shifts of protons indicated on the chemical structure.

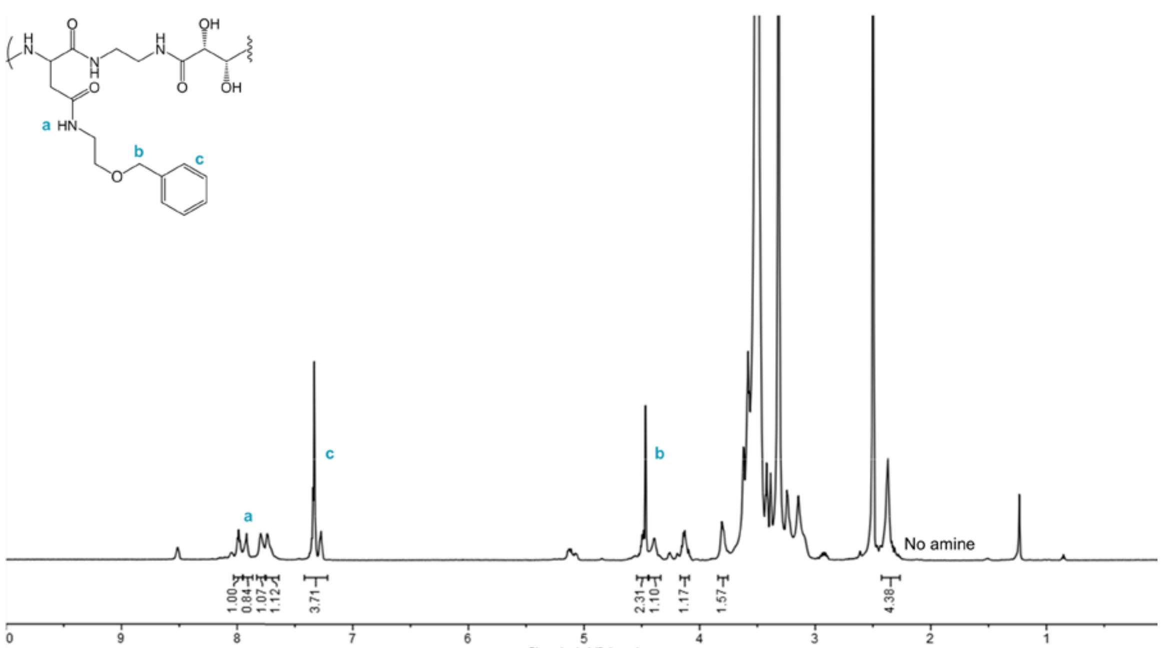

Fig. A.12. ^{1}H NMR of Bzl-protected MAP-amidoethanol. Aromatic (c) and alkane (b) peaks from benzyl protecting are both present in the purified MAP-amidoethanol intermediate, along with an additional amide (a) peak and no unreacted amine.

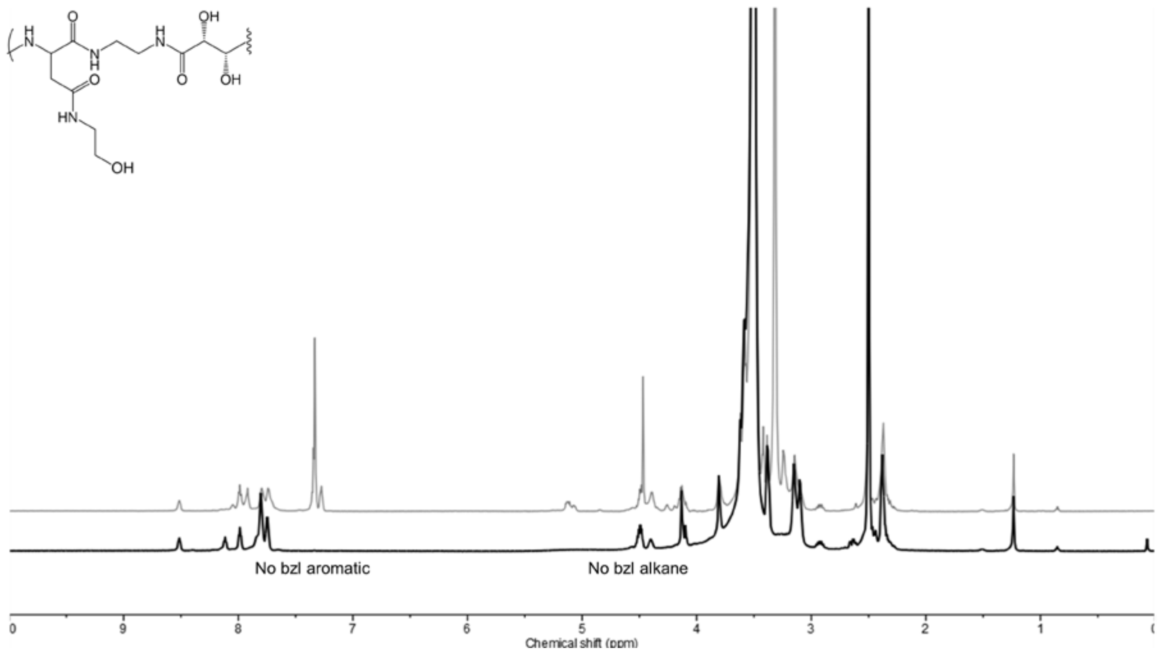

Fig. A.13. [1]H NMR of MAP-amidoethanol (black trace) compared that before deprotection (gray trace). Peaks from benzyl protecting group are no longer present.

A.3.3 Lapatinib forms single carbamate product under mild conjugation conditions

Reactivity of the lapatinib secondary amines was first investigated before adding the molecule to the MAP derivatives. The reaction of lapatinib with N,N'-disuccinimidyl carbonate (DSC) in deuterated DMSO was monitored by ESI and NMR (Fig. A.14). DSC was chosen because it is the smallest homobifunctional NHS ester coupling agent commercially available. Furthermore, it is significantly more stable and less toxic than similar crosslinking reagents, such as carbonyl diimidazole or triphosgene. In nonaqueous environments, DSC can react with two amine groups to form a substituted urea derivative or can be used to conjugate a hydroxylic compound with an amine-containing compound to form a carbamate linkage.

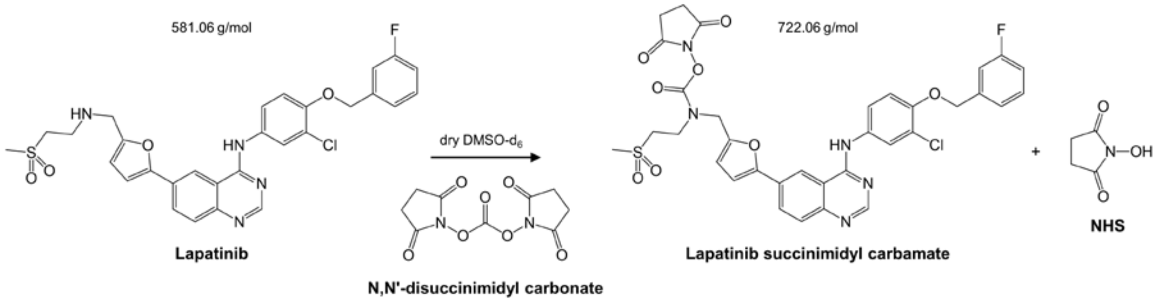

Fig. A.14. Reaction of lapatinib with N,N'-disuccinimidyl carbonate to form lapatinib succinimidyl carbamate. The molecular masses of lapatinib and lapatinib succinimidyl carbamate are shown above the corresponding chemical structures.

ESI analysis confirmed DSC reactivity with lapatinib. Within 4 h, most of the lapatinib was converted to lapatinib succinimidyl carbamate, as determined by the increased abundance of the mass spectrum peak at m/z of 722 (Fig. A.15). Interestingly, no higher m/z species were detected, suggesting that only one secondary amine is converted to a succinimidyl carbonate per lapatinib molecule.

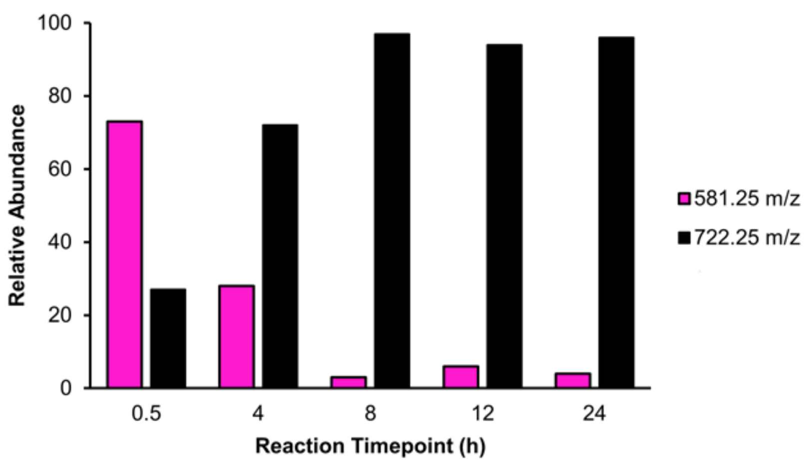

Fig. A.15. Lapatinib shows high reactivity of a single secondary amine with DSC. Relative intensities of mass spectrum peaks at m/z of 581 (magenta) and 722 (black) corresponding to lapatinib and lapatinib succinimidyl carbamate species, respectively, are provided for various timepoints. Full conversion was achieved within 8 h.

To determine whether a single carbamate product or a mixture was formed, the crude product was further analyzed by NMR. Integration of the crude product ^{1}H NMR at 12 h revealed that near full conversion was achieved using an equimolar ratio of lapatinib:DSC, consistent with the ESI results (Fig. A.16). ^{1}H NMR of native lapatinib is provided in Fig. A.17 for comparison. Interestingly, several peak pairs were observed for protons in proximity to the newly formed amide, indicating either the presence of rotamers or the formation of two different products. Furthermore, the peak associated with the more sterically hindered lapatinib amine was present, while the peak corresponding to the secondary amine between the furan and methanesulfonyl moieties was lost, suggesting that a single carbamate product was formed between DSC and the less sterically hindered amine. Additionally, a 2D ^{1}H NOESY experiment was performed on the crude product at 12 h. Crosspeaks for all peak pairs in the 1D spectrum were present and in phase with diagonal response, indicating rotational conformations in slow exchange (NOE correlations would be negative) (Fig A.18). These data further suggest the formation of a single lapatinib succinimidyl carbonate product with cis/trans rotamers.

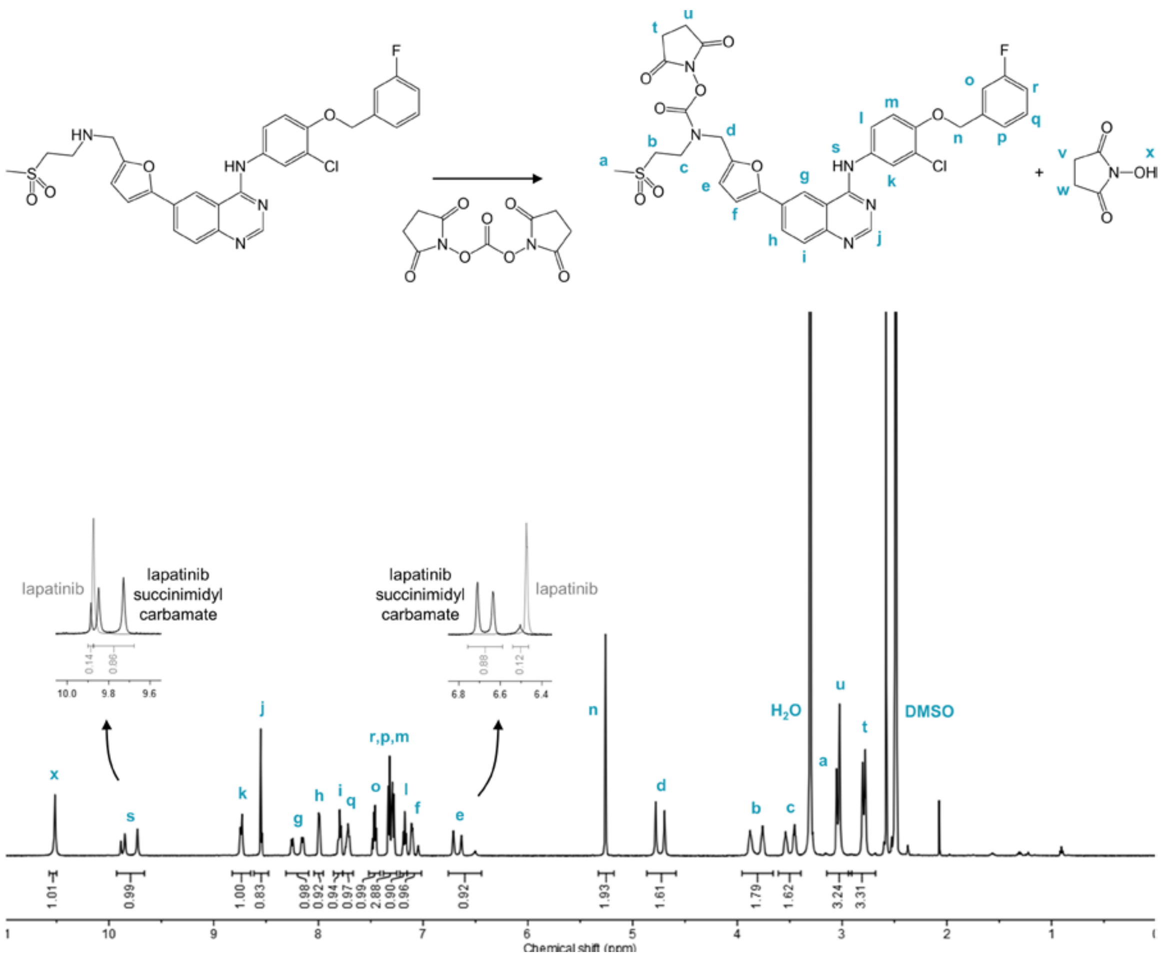

Fig. A.16. [1]H NMR of crude product at 12 h. Lowercase letters (a–x) shown above peaks correspond to chemical shifts of protons indicated on the chemical structures. Peak from secondary amine between furan and methanesulfonyl moieties is no longer present, but peak from more hindered secondary amine (s) is present. Several peak pairs (s,g,e,d,b,c) in proximity to formed amide are observed. Magnified regions of 1H NMR of lapatinib (gray) and crude product (black) for peaks s and e are provided (inset).

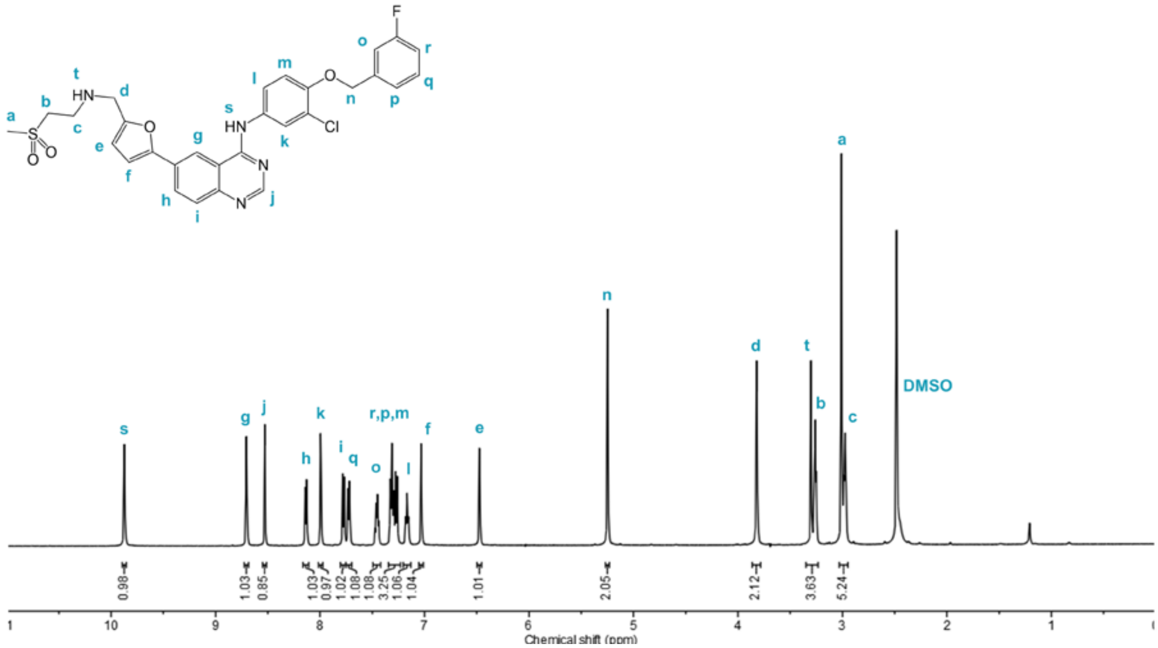

Fig. A.17. ^1H NMR of unreacted lapatinib. Lowercase letters (a–t) shown above peaks correspond to chemical shifts of protons indicated on the chemical structures. Peaks were identified by expected chemical shifts and addition of D_2O to locate exchangeable amine protons.

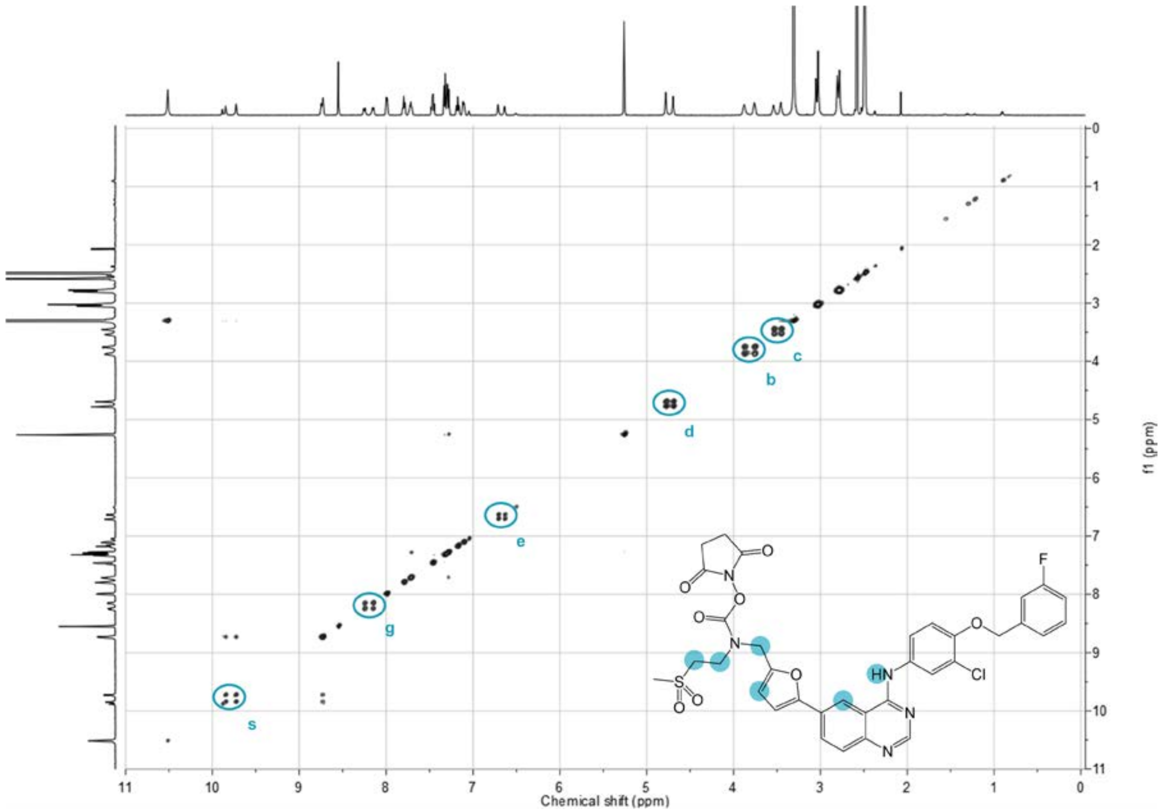

Fig. A.18. 2D ^{1}H NOESY of crude product at 12 h. Crosspeaks are present and in phase for all peak pairs in 1D ^{1}H NMR (circled). Locations of protons showing cis/trans rotamers are highlighted on inset chemical structure (blue).

A.3.4 Addition of lapatinib to MAP-amidoethanamine and MAP-amidoethanol polymers through urea and carbamate bonds

After verifying that lapatinib could be conjugated through one of its secondary amines, lapatinib was activated with DSC, followed by conjugation of the drug to either MAP-amidoethanamine or MAP-amidoethanol (Fig. A.19A). This synthesis scheme was chosen over activation of the polymer derivatives with excess DSC, followed by addition of lapatinib (Fig. A.19B) because the latter resulted in higher than expected drug loading and material that did not form nanoparticles. This was likely due to DSC reacting with nucleophiles on the MAP backbone in addition to the intended primary amine and hydroxyl handles on MAP-amidoethanamine and MAP-amidoethanol, respectively. Additionally, we added equimolar activated lapatinib to the polymer instead of excess drug to prevent overloading of the MAP derivatives and limit conjugation to the sterically favored primary amine and hydroxyl moieties.

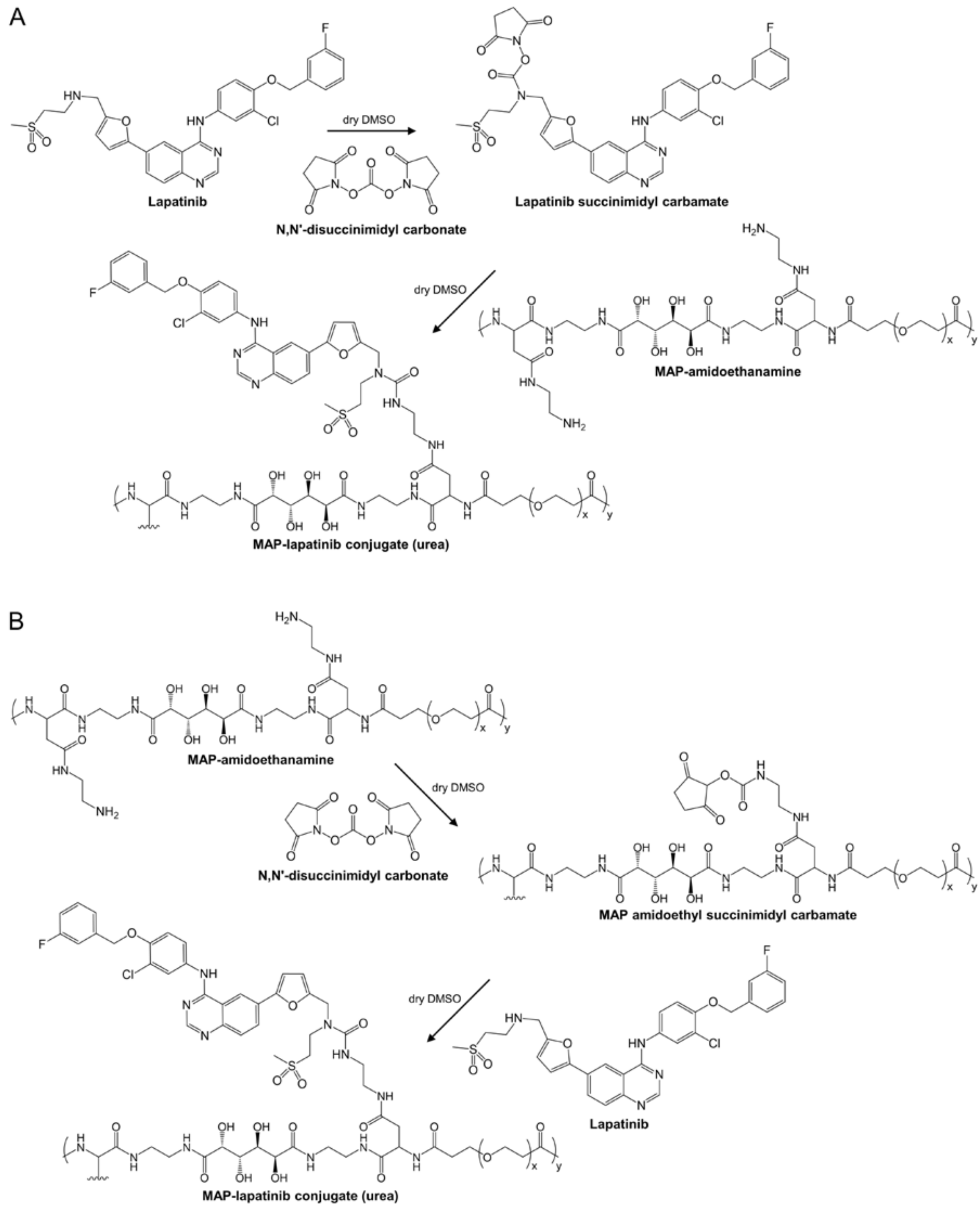

Fig. A.19. Synthesis of MAP-lapatinib polymer-drug conjugates. Schemes for urea-based coupling are provided as an example. Carbamate-based analogs were prepared using MAP-amidoethanol in place of MAP-amidoethanamine. (**A**) Activation of lapatinib with DSC, followed by addition of amidoethanamine derivative. (**B**) Activation of amidoethanamine derivative with DSC, followed by addition of lapatinib.

Following synthesis of the urea- and carbamate-based MAP-lapatinib conjugates, the quantity of lapatinib loaded onto the polymer was determined using absorbance detection and HPLC. The drug content for these conjugates was 11.2 and 10.7% (w/w lapatinib/MAP), respectively. These amounts are comparable to the drug loading achieved with CPT previously.

A.3.5 Preparation and characterization of lapatinib-loaded, TfR-targeted MAP nanoparticles

MAP-lapatinib conjugates were dialyzed against water to promote formation of nanoparticles with hydrophobic lapatinib molecules preferentially clustered in the core and vicinal diols on the surface. Both the urea and carbamate conjugate nanoparticle formulations had diameters near 50 nm without targeting agent, as measured by dynamic light scattering, and near-neutral zeta potentials when measured in pH 7.4 buffer (Table 3.2). To prepare TfR-targeted MAP-lapatinib nanoparticles, Tf-PEG-nitroPBA was prepared as previously described (Chapter III) and added to the nanoparticles at 20 molar excess. Addition of the targeting agent led to a moderate decrease in nanoparticle size, consistent with steric stabilization provided by the Tf-PEG groups upon complexation with the nanoparticle core. These data suggest that the mucic acid groups are not modified during the conjugate synthesis. Thus, it appears that conjugation was limited to the more accessible primary amine and hydroxyl moieties by first activating lapatinib with DSC followed by its equimolar addition to the MAP derivatives.

Formulation	Nanoparticle diameter, pH 7.4, nm	Zeta potential, pH 7.4, mV
MAP*-lapatinib nanoparticle (urea)	47.5 ± 2.1	-0.26 ± 0.48
MAP†-lapatinib nanoparticle (carbamate)	49.8 ± 1.9	-0.51 ± 0.64
TfR-targeted, MAP*-lapatinib nanoparticle (urea)	33.7 ± 1.3	-0.32 ± 0.55
TfR-targeted, MAP†-lapatinib nanoparticle (carbamate)	32.9 ± 1.4	-0.98 ± 0.86

Table A.1. Nanoparticle formulations and characteristics. MAP* and MAP† denote amine- and hydroxyl-containing MAP derivatives, respectively. Data shown for hydrodynamic diameter and zeta potential are the average of 5 measurements ±1 SD.

A.4 Conclusions

Here, we detail the synthesis of two modified MAP polymer scaffolds that contain primary amine and hydroxyl functional handles for drug conjugation. Urea- and carbamate-based lapatinib polymer-drug conjugate materials were prepared with high drug loading. Nanoparticles formed by these conjugate materials retained the optimal design parameters identified in our previous investigations, including a sub-100-nm diameter and near-neutral zeta potential. Before use in a brain metastasis model, the drug release kinetics would need to me measured to determine whether the urea and carbamate linkages can be used to release lapatinib under physiologic conditions in the brain. If these nanoparticles are capable of releasing native lapatinib at an acceptable rate ($t_{1/2}$ ~ days), they could potentially be more effective against HER2-positive breast cancer brain metastases compared to the MAP-CPT nanoparticles.

A.5 Materials and methods

Cytotoxicity Assay. BT474-Gluc cells were seeded at a density of 3,000 cells/well in 96-well plates. After 24 h, media was removed and replaced with fresh media containing different concentrations of lapatinib or CPT. After 72 h, BT474-Gluc cell viability was measured using the CellTiter 96 Aqueous One Solution cell proliferation assay (Promega) on an Infinite M200 microplate reader (Tecan), according to the manufacturer's protocol.

Synthesis of MAP-Amidoethanamine.

Synthesis of* N*-Boc-Protected MAP-Amidoethanamine. Anhydrous dimethyl sulfoxide (10 mL) was added under argon to dissolve MAP (200 mg, 1 equiv) in a 25 mL round-bottomed flask. To this was added EDC (111 mg, 5.3 equiv) and NHS (50 mg, 4 equiv) dissolved in anhydrous dimethyl sulfoxide (3 mL), followed by *N*-Boc-ethylenediamine (64 µL, 4 equiv) and anhydrous N,N-diisopropylethylamine (75 µL, 4 equiv) dried over molecular sieves. The reaction was stirred under argon at room temperature overnight. The solution was dialyzed against dimethyl sulfoxide 3 times and nanopure water 2 times using a 10 kDa MWCO Spectra/Por 7 membrane (Spectrum). The solution was dialyzed against dimethyl sulfoxide and nanopure water using a 10 kDa MWCO Spectra/Por 7 membrane (Spectrum), filtered through a 0.2 µm Supor membrane Acrodisc syringe filter (Pall), and lyophilized to yield *N*-Boc-protected MAP-amidoethanamine (182 mg) as a white, sponge-like solid.

Synthesis of MAP-Amidoethanamine. N-Boc-protected MAP-amidoethanamine (182 mg) in a 25 mL round-bottomed flask was placed in a water bath. 3 N hydrochloric acid in methanol (4 mL) was added, and the reaction flask was sealed and vented with a needle.

The reaction was stirred at 25 ºC for 8 h. Solvent was removed by rotary evaporation. The solid was dissolved in a 1:1 mixture of nanopure water and methanol (5 mL) and dried by rotary evaporation twice more. The solid was then reconstituted in nanopure water, dialyzed against water using a 10 kDa MWCO Spectra/Por 7 membrane (Spectrum), and then filtered through a 0.2 µm Supor membrane Acrodisc syringe filter (Pall) and lyophilized to yield MAP-amidoethanamine (160 mg) as a white, sponge-like solid. The product was stored under argon at -20 ºC.

Determination of Amine Content in MAP-Amidoethanamine. Amine content was measured using the TNBSA Solution assay (5% (w/v), Thermo Scientific), according to the manufacturers protocol with the below modifications. MAP-amidoethanamine was prepared at 300, 200, and 100 µg/mL in reaction buffer. A standard curve of L-glutamic acid was prepared over a concentration range of 20 to 2 µg/mL in reaction buffer. 50 µL TNBSA working solution was added to 100 µL sample in a 96-well plate (Nunc) and briefly mixed. Absorbance at 355 nm was measured in triplicate on an Infinite M200 microplate reader (Tecan) after 2 h incubation.

Synthesis of MAP-Amidoethanol.

Synthesis of Bzl-Protected MAP-Amidoethanol. Anhydrous dimethyl sulfoxide (10 mL) was added under argon to dissolve MAP (200 mg, 1 equiv) in a 25 mL round-bottomed flask. To this was added EDC (111 mg, 5.3 equiv) and NHS (50 mg, 4 equiv) dissolved in anhydrous dimethyl sulfoxide (3 mL), followed by 2-(benzyloxy)-ethan-1-amine (69 µL, 4 equiv) and anhydrous N,N-diisopropylethylamine (75 µL, 4 equiv) dried over molecular sieves. The reaction was stirred under argon at room temperature overnight. The solution was dialyzed against dimethyl sulfoxide 3 times and nanopure water 2 times using a 10 kDa MWCO Spectra/Por 7 membrane (Spectrum). The solution was dialyzed against dimethyl sulfoxide and nanopure water using a 10 kDa MWCO Spectra/Por 7 membrane (Spectrum), filtered through a 0.2 µm Supor membrane Acrodisc syringe filter (Pall), and lyophilized to yield Bzl-protected MAP-amidoethanamine (194 mg) as a white, sponge-like solid.

Synthesis of MAP-Amidoethanol. Methanol (15 mL) was added to mucic acid Bzl-protected MAP-amidoethanol (194 mg) and 20% (w) palladium hydroxide on carbon (200 mg) in a 25 mL round-bottomed flask. The reaction flask was sealed and vented with argon for 30 min. Hydrogen gas was added by a double-layered balloon, and the reaction was stirred for 24 h at room temperature. Catalyst was separated by centrifugation at 3220 g for 15 min, and the solvent removed by rotary evaporation. The solid was reconstituted in nanopure water, dialyzed against water using a 10 kDa MWCO Spectra/Por 7 membrane (Spectrum), and then filtered through a 0.2 µm Supor membrane Acrodisc syringe filter (Pall) and lyophilized to yield MAP-amidoethanol (179 mg) as a white, sponge-like solid. The product was stored under argon at -20 ºC.

Synthesis of Lapatinib Succinimidyl Carbamate. Deuterated dimethyl sulfoxide (0.5 mL) was added under argon to dissolve lapatinib (5 mg, 1 equiv, Sigma) in a 4 mL glass vial sealed with a septum. To this was added N,N'-disuccinimidyl carbonate (2.2 mg, 1 equiv) dissolved in deuterated dimethyl sulfoxide (0.5 mL). The reaction was stirred under argon at room temperature. Aliquots were removed over time and assayed by ESI using a 1:1 water:methanol solvent mixture. Electrospray ionization (ESI) masses of small molecules were acquired on a Finnigan LCQ ion trap mass spectrometer. ^{1}H NMR spectra were acquired on a Varian 600 MHz spectrometer (Inova) in deuterated dimethyl sulfoxide.

Synthesis of MAP-Lapatinib Conjugates.

Synthesis of Urea- and Carbamate-Based MAP-Lapatinib Conjugates. Anhydrous dimethyl sulfoxide (1 mL) was added under argon to dissolve lapatinib (7.6 mg, 1.2 equiv, Sigma) in a 10 mL round-bottomed flask. To this was added N,N'-disuccinimidyl carbonate (3.3 mg, 1.2 equiv) dissolved in anhydrous dimethyl sulfoxide (1 mL). The reaction was stirred under argon at room temperature for 6 h. MAP-amidoethanamine (20 mg, 1 equiv) was added to a separate oven-dried 10 mL round-bottomed flask. The flask was sealed, and vented with argon. To this was added anhydrous dimethyl sulfoxide (2 mL) to dissolve the polymer. The lapatinib solution was added dropwise to the polymer solution. The reaction was stirred under argon at room temperature overnight. The solution was dialyzed against dimethyl sulfoxide 3 times and nanopure water 2 times using a 10 kDa MWCO Spectra/Por 7 membrane (Spectrum). Precipitate was removed by centrifugation at 3220 g for 15 min, and the supernatant was filtered through a 0.2 µm Supor membrane Acrodisc syringe filter (Pall) to yield MAP-lapatinib urea-based conjugate as self-assembled nanoparticles in solution. A portion of this clear yellow solution was lyophilized to determine percent lapatinib conjugation. The remaining product was formulated into 0.9% (w/v) saline and stored at -20 ºC. A similar procedure was followed using MAP-amidoethanol (20 mg, 1 equiv) to synthesize MAP-lapatinib carbamate-based conjugate.

Determination of Lapatinib Content in MAP-Lapatinib Conjugates. The amount of polymer-bound lapatinib was determined on an Agilent 1100 HPLC system with a reverse phase column (Synergi 4 µm Hydro-RP 80 Å, Phenomenex) connected to a detector set to measure absorbance at 264 nm. 50% acetonitrile/50% potassium phosphate buffer (10 mM, pH 7.4) was used as the eluent at a flow rate of 0.5 mL/min. To cleave lapatinib from the polymer, 15 µL of 0.2 N NaOH was added to 20 µL sample and incubated for 3 h. Then, 15 µL of 0.2 N HCl was added to neutralize the solution, followed by 30 min incubation. Subsequently, 150 µL methanol was added. The sample was centrifuged at 14000 g for 15 min and supernatant filtered using a 0.45 µm PTFE membrane Millex-LH syringe filter (EMD Millipore). Lapatinib content was determined by injecting 100 µL of the filtered solution onto the column compared to a calibration curve of known concentrations of lapatinib.

Synthesis of CO_2H-PEG-nitroPBA.

Synthesis of 3-acyl chloride-5-nitrophenyl boronic acid. 3-carboxy-5-nitrophenyl boronic acid (nitroPBA, 100 mg, 1 equiv, Alfa Aesar) was added to an oven-dried 10 mL round-bottomed flask. The reaction flask was sealed and vented with argon. Anhydrous tetrahydrofuran with BHT inhibitor (4 mL) was added to dissolve the boronic acid, followed by anhydrous dimethylformamide (7 µL, 0.2 equiv). The flask was cooled to 0 ºC in an ice bath, and oxalyl chloride (98 µL, 2.4 equiv) was added dropwise. After addition of oxalyl chloride, the ice bath was removed and the reaction was stirred under argon for 2 hrs. Solvent was evaporated under vacuum to yield 3-acyl chloride-5-nitrophenyl boronic acid (97 mg) as a yellow solid.

Synthesis of CO_2H-PEG-nitroPBA. 3-acyl chloride-5-nitrophenyl boronic acid (46 mg, 2 equiv) was added to an oven-dried 25 mL round-bottomed flask. The reaction flask was sealed, vented with argon, and cooled to 0 ºC in an ice bath. Anhydrous DCM (5 mL) was added to dissolve the boronic acid. Acetic acid-PEG-amine (5 kDa, 500 mg, 1 equiv, JenKem) was added to a separate oven-dried 10 mL round-bottomed flask. The flask was sealed, and vented with argon. To this was added anhydrous N,N-diisopropylethylamine (35 µL, 2 equiv) dried over molecular sieves, and anhydrous DCM (5 mL) to dissolve the PEG. The PEG solution was added dropwise to the boronic acid solution. The reaction flask was left in the ice bath to slowly warm to room temperature, and stirred under argon overnight protected from light. Solvent was removed under vacuum, and the solid reconstituted in 0.5 N HCl (5 mL) and stirred for 15 min. The solution was filtered 0.2 µm Supor membrane Acrodisc syringe filter (Pall) and dialyzed against nanopure water until constant pH using a 15 mL Amicon Ultra 3 kDa spin filter (EMD Millipore), and lyophilized to yield CO_2H-PEG-nitroPBA (436 mg) as a white solid.

Synthesis of Tf-PEG-nitroPBA. CO_2H-PEG-nitroPBA (8 mg, 25 equiv), EDC-HCl (3.1 mg, 250 equiv), and NHS (2.8 mg, 375 equiv) were dissolved in 0.1 M MES buffer, pH 6.0 (0.33 mL), and stirred for 15 min at room temperature. The reaction mixture was then added to a 0.5 mL Amicon Ultra 3 kDa spin filter (EMD Millipore), and centrifuged to isolate the activated nitroPBA-PEG-NHS ester. The ester was added to human holo-Tf (5 mg, 1 equiv, Sigma) dissolved in 0.1 M PBS, 0.15 M NaCl, pH 7.4 (0.75 mL). The reaction was lightly agitated for 2 h at room temperature, and then dialyzed against 0.1 M PBS, 0.15 M NaCl, pH 7.4 using 0.5 mL Amicon Ultra 50 kDa spin filters (EMD Millipore) to remove excess PEG. A portion of this solution was dialyzed into 10 mM PB, pH 7.4, and conjugation was verified by MALDI-TOF (autoflex speed TOF/TOF, Bruker) using a sinapinic acid matrix.

Preparation of Nanoparticles. Tf-PEG-nitroPBA conjugates in PBS, pH 7.4 were added at 20x molar excess to MAP-lapatinib nanoparticles to form TfR-targeted MAP-lapatinib nanoparticles (20 Tf per particle). The solution was gently mixed by pipette, and allowed to equilibrate for 10 min. Nanoparticle formulations were filtered using a 0.45 µm PTFE membrane Millex-LH syringe filter (EMD Millipore).

Nanoparticle Characterization. Nanoparticles were characterized using a Brookhaven Instruments Corporation (BIC) ZetaPALS. Nanoparticles were diluted in PBS, pH 7.4 and hydrodynamic diameter was measured by dynamic light scattering (DLS) using BIC Particle Sizing Software. Particle formulations were diluted in 10 mM PB, pH 7.4 and zeta potential was measured using BIC PALS Zeta Potential Analyzer software with a target residual of 0.02. Five runs were performed for both the nanoparticle diameter and zeta potential measurements.

A.6 References

1. Tripathy D, Slamon DJ, Cobleigh M, Arnold A, Saleh M, et al. (2004) Safety of treatment of metastatic breast cancer with trastuzumab beyond disease progression. *Journal of Clinical* Oncology 22(6):1063–1070.

2. Montemurro F, Donadio M, Clavarezza M, Redana S, Jacomuzzi ME, et al. (2006) Outcome of patients with HER2-positive advanced breast cancer progressing during trastuzumab-based therapy. *The Oncologist* 11(4):318–324.

3. Romond EH, Perez EA, Bryant J, Suman VJ, Geyer CE Jr., et al. (2005) Trastuzumab plus adjuvant chemotherapy for operable HER2-positive breast cancer. *The New England Journal of Medicine* 353(16):1673–1684.

4. Piccart-Gebhart MJ, Procter M, Leyland-Jones B, Goldhirsch A, Untch M, et al. (2005) Trastuzumab after adjuvant chemotherapy in HER2-positive breast cancer. *The New England Journal of Medicine* 353(16):1659–1672.

5. Lin NU, Winer EP (2007) Brain metastases: The HER2 paradigm. *Clinical Cancer Research* 13(6):1648–1655.

6. Chien AJ, Rugo HS (2013) Emerging treatment options for the management of brain metastases in patients with HER2-positive metastatic breast cancer. *Breast Cancer Research and Treatment* 137(1):1–12.

7. Ramakrishna N, et al. (2014) Recommendations on disease management for patients with advanced human epidermal growth factor receptor 2-positive breast cancer and brain metastases: American Society of Clinical Oncology clinical practice guideline. *Journal of Clinical Oncology* 32(19):2100–2108.

8. Xia W, Mullin RJ, Keith BR, Liu LH, Ma H, et al. (2002) Anti-tumor activity of GW572016: a dual tyrosine kinase inhibitor blocks EGF activation of EGFR/erbB2 and downstream Erk1/2 and AKT pathways. *Oncogene* 21(41):6255–6263.

9. Burstein HJ, Storniolo AM, Franco S, Forster J, Stein S, et al. (2008) A phase II study of lapatinib monotherapy in chemotherapy-refractory HER2-positive and HER2-negative advanced or metastatic breast cancer. *Annals of Oncology* 19(6):1068–1074.

10. Geyer CE, Forster J, Lindquist D, Chan S, Romieu CG, et al. (2006) Lapatinib plus capecitabine for HER2-positive advanced breast cancer. *The New England Journal of Medicine* 355(26):2733–2743.

11. Cameron D, Casey M, Press M, Lindquist D, Pienkowski T, et al. (2008) A phase III randomized comparison of lapatinib plus capecitabine versus capecitabine alone in women with advanced breast cancer that has progressed on trastuzumab: updated efficacy and biomarker analyses. *Breast Cancer Research and Treatment* 112(3):533–543.

12. Konecny GE, Pegram MD, Venkatesan N, Finn R, Yang G, et al. (2006) Activity of the dual kinase inhibitor lapatinib (GW572016) against HER-2-overexpressing and trastuzumab-treated breast cancer cells. *Cancer Research* 66(3):1630–1609.

13. Xia W, Gerard CM, Liu L, Baudson NM, Ory TL, Spector NL (2005) Combining lapatinib (GW572016), a small molecule inhibitor of ErbB1 and ErbB2 tyrosine kinases, with therapeutic anti-ErbB2 antibodies enhances apoptosis of ErbB2-overexpressing breast cancer cells. *Oncogene* 24(41):6213–6221.

14. Scaltriti M, Verma C, Guzman M, Jimenez J, Parra JL, et al. (2009) Lapatinib, a HER2 tyrosine kinase inhibitor, induces stabilization and accumulation of HER2 and potentiates trastuzumab-dependent cell cytotoxicity. *Oncogene* 28(6):803–814.

15. Junttila TT, Akita RW, Parsons K, Fields C, Lewis Phillips GD, et al. (2009) Ligand-independent HER2/HER3/PI3K complex is disrupted by trastuzumab and is effectively inhibited by the PI3K inhibitor GDC-0941. *Cancer Cell* 15(5):429–440.

16. Hudis CA (2007) Trastuzumab--mechanism of action and use in clinical practice. *The New England Journal of Medicine* 357(1):39–51.

17. Tevaarwerk AJ, Kolesar JM (2009) Lapatinib: a small-molecule inhibitor of epidermal growth factor receptor and human epidermal growth factor receptor-2 tyrosine kinases used in the treatment of breast cancer. *Clinical Therapeutics* 31 Pt 2:2332–2348.

18. Blackwell KL, Burstein HJ, Storniolo AM, Rugo H, Sledge G, et al. (2010) Randomized study of Lapatinib alone or in combination with trastuzumab in women with ErbB2-positive, trastuzumab-refractory metastatic breast cancer. *Journal of Clinical Oncology* 28(7):1124–1130.

19. Saleem A, Searle GE, Kenny LM, Huiban M, Kozlowski K, et al. (2015) Lapatinib access into normal brain and brain metastases in patients with Her-2 overexpressing breast cancer. *European Journal of Nuclear Medicine and Molecular Imaging Research* 5:30.

20. Morikawa A, Peereboom DM, Thorsheim HR, Samala R, Balyan R, et al. (2015) Capecitabine and lapatinib uptake in surgically resected brain metastases from metastatic breast cancer patients: a prospective study. *Neuro-Oncology* 17(2):289–295.

21. Taskar KS, Rudaraju V, Mittapalli RK, Samala R, Thorsheim HR, et al. (2012) Lapatinib distribution in HER2 overexpressing experimental brain metastases of breast cancer. *Pharmaceutical Research* 29(3):770–781.

22. Jordan AM, Khan TH, Malkin H, Osborn HM (2002) Synthesis and analysis of urea and carbamate prodrugs as candidates for melanocyte-directed enzyme prodrug therapy (MDEPT). *Bioorganic & Medicinal Chemistry* 10(8):2625–2633.

23. Simplício AL, Clancy JM, Gilmer JF (2008) Prodrugs for amines. *Molecules* 13(3):519–547.

24. Ghosh AK, Brindisi M (2017) Organic carbamates in drug design and medicinal chemistry. *Journal of Medicinal Chemistry* 58(7):2895–2940.

25. Rautio J, Kumpulainen H, Heimbach T, Oliyai R, Oh D, et al. (2008) Prodrugs: design and clinical applications. *Nature Reviews Drug Discovery* 7(3):255–270.

26. Miwa M, Ura M, Nishida M, Sawada N, Ishikawa T, et al. (1998) Design of a novel oral fluoropyrimidine carbamate, capecitabine, which generates 5-fluorouracil selectively in tumours by enzymes concentrated in human liver and cancer tissue. *European Journal of Cancer* 34(8):1274–1281.

27. Quinney SK, Sanghani SP, Davis WI, Hurley TD, Sun Z, et al. (2005) Hydrolysis of capecitabine to 5'-deoxy-5-fluorocytidine by human carboxylesterases and inhibition by loperamide. *The Journal of Pharmacology and Experimental Therapeutics* 313(3):1011–1016.

28. Cory AH, Owen TC, Barltrop JA, Cory JG (1991) Use of an aqueous soluble tetrazolium/formazan assay for cell growth assays in culture. *Cancer communications* 3(7):207–212.

29. Dörwald FZ (2012) *Lead optimization for medicinal chemists: Pharmacokinetic properties of functional groups and organic compounds*, (Wiley-VCH, Weinheim).

30. Han H, Davis ME (2013) Targeted nanoparticles assembled via complexation of boronic-acid-containing targeting moieties to diol-containing polymers. *Bioconjug Chem* 24(4):669–677.

Appendix B

NCI CANCER CLOSE UP

B.1 Preamble

During my thesis work, I participated in the NCI Cancer Close Up project, an annual competition that gathers, shares, and exhibits visually compelling images (e.g., microscopy, *in vivo*, *in vitro*, etc.) that help illustrate the cancer research story. Because the focus of the 2017 NCI Cancer Close Up project was nanotechnology, I submitted two images from my NCI-supported research. One of the submissions, titled ‘Nanoparticles in Brain Metastases’, was selected and featured in NCI’s public image galleries (NCI Visuals Online and Instagram), shared via NCI’s Twitter and Facebook channels, as well as displayed on Cancer.gov. The submission was also selected as part of a smaller collection and prominently displayed at the NCI Exhibits at the 2017 AACR and ASCO annual meetings. The second submission was selected for the general image collection on NCI Visuals Online, titled ‘The Blood-Brain Barrier’. The following are the images selected by the reviewers.

B.2 Image selected for 2017 NCI Cancer Close Up

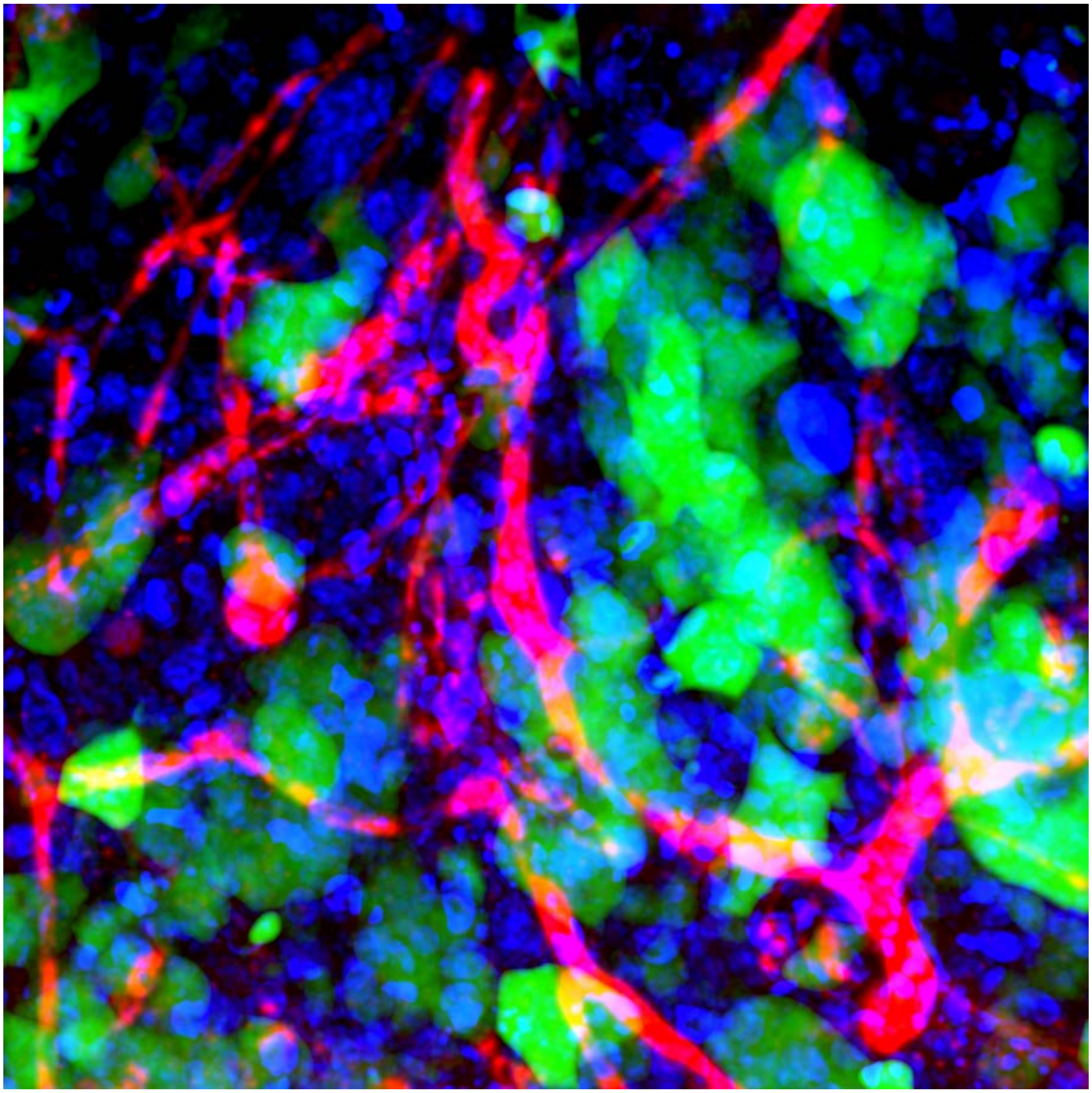

Fig. B.1. Nanoparticles in brain metastases. Cancer that has spread (metastasized) to the brain is normally untreatable because the protective blood-brain barrier blocks entry of most therapeutics. Nanoparticles capable of carrying drugs and "hitchhiking" across the barrier may allow the delivery of life-saving therapies to these tumors. This image shows blood vessels (red), cell nuclei (blue), and human metastatic breast cancer cells (green) in a mouse's brain, after intravenous administration of experimental nanoparticles that can cross the blood-brain barrier.

Link: https://visualsonline.cancer.gov/details.cfm?imageid=11170

B.3 Image selected for NCI Visuals Online

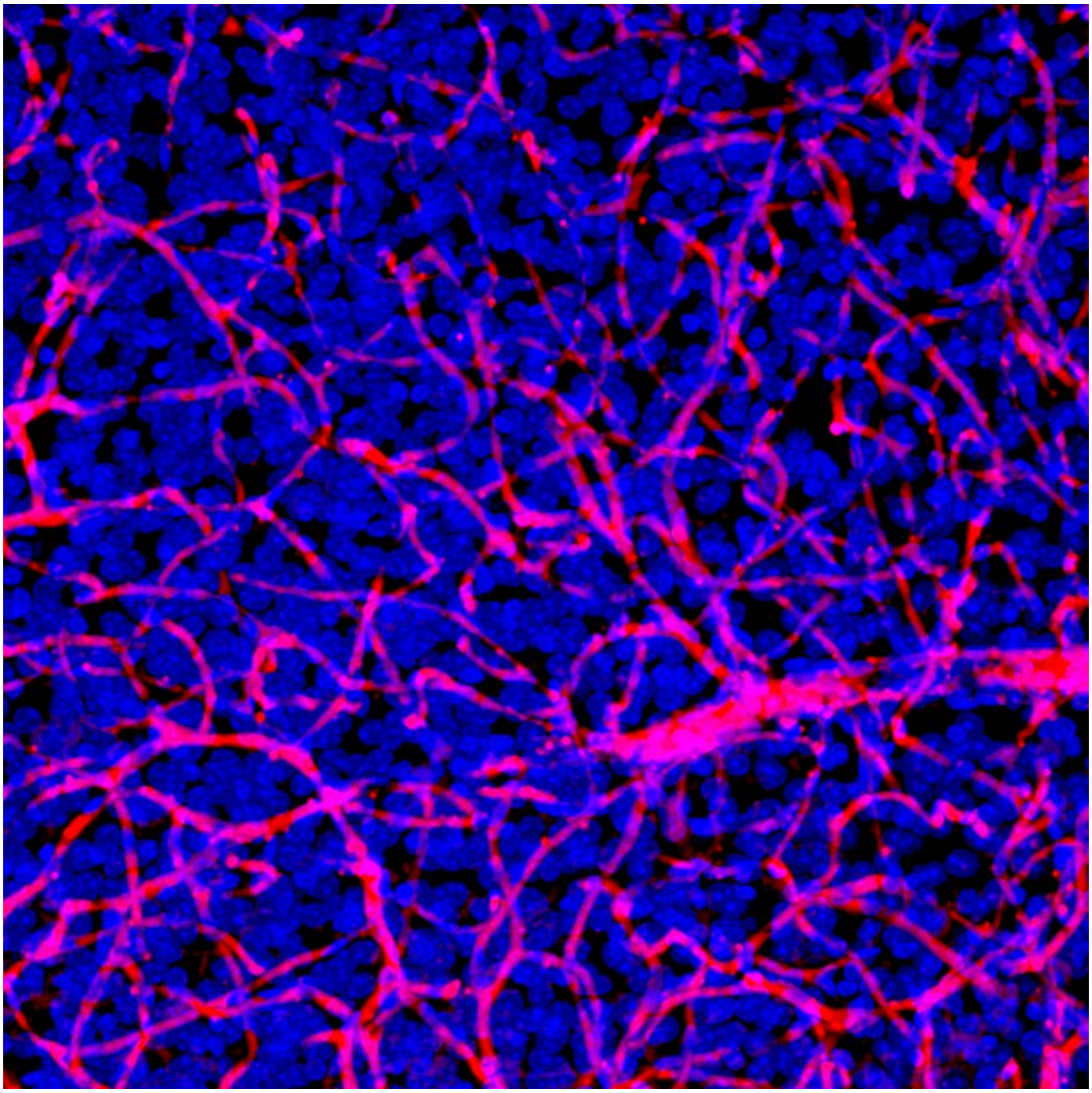

Fig. B.2. The blood-brain barrier. This image shows a dense network of blood vessels (red) and nuclei (blue) obtained from mouse brain tissue that was optically cleared to look deeper into the tissue than otherwise possible. The brain's blood vessels are nearly impermeable, allowing only the passage of key nutrients while blocking that of harmful substances. Unfortunately, this blood-brain barrier (BBB) also excludes most therapeutics. By designing drug-containing nanoparticles that can "hitchhike" across the BBB, researchers hope to finally penetrate the barrier, and deliver life-saving drugs to cancers in the brain.

Link: https://visualsonline.cancer.gov/details.cfm?imageid=11169

B.4 Materials and methods

IC Brain Metastasis Model. All animals were treated according to the NIH guidelines for animal care and use as approved by the Caltech Institutional Animal Care and Use Committee (1). BT474-Gluc cells, transduced with an expression cassette encoding Gluc and CFP separated by an internal ribosomal entry site using a lentiviral vector, were obtained from Dr. Jain at Harvard University. BT474-Gluc cells were maintained in RPMI 1640 supplemented with 10% (v/v) FBS in a humidified oven at 37°C with 5% CO_2. 50,000 BT474-Gluc cells in 2 μL RPMI were intracranially injected into the right cerebral hemisphere of female Rag2$^{-/-}$;Il2rg$^{-/-}$ mice (Jackson Laboratory) using a stereotaxic apparatus at a rate of 0.1 μL/min. The coordinates for injection were 2 mm posterior, 1.5 mm lateral to bregma, and 2.5 mm depth from bregma.

Tissue Processing. Mice were sacrificed following signs of prolonged distress or loss of >20% body weight. The mice were anaesthetized and transcardially perfused with a 10% sucrose solution, followed by a 4% (v/v) formaldehyde in PBS, pH 7.4. Excised brain tissue was post-fixed in 4% (v/v) formaldehyde in PBS, pH 7.4 overnight at 4 °C, then washed in PBS, pH 7.4 with 0.02% NaN_3 to remove excess fixative. 1 mm-thick tissue sections of brain tumor and healthy brain tissue were prepared using the CLARITY method for clearing large tissue volumes (2). In short, tumor and healthy brain tissue were sectioned on a vibratome to a thickness of 1 mm, and stored at 4 °C, protected from light until further processing. Tissues were incubated in A4P0 hydrogel monomer solution (4% acrylamide in PBS, pH 7.4) overnight with shaking (acrylamide solution, Bio-Rad; thermal initiator, Wako). Samples were degassed, then polymerized in a 37 °C incubator for 3 h. Following polymerization, samples were washed in PBS, pH 7.4 to remove residual hydrogel, then cleared at 37 °C with gentle agitation in 8% (w/v) SDS with 0.02% NaN_3 in PBS, pH 8.0 until optically transparent. Clearing times varied for tissue types. Samples were washed in PBS, pH 7.4 with 0.02% NaN_3 for 2 days with minimum of four exchanges.

For vasculature identification, brain samples were incubated with a 1:200 dilution of an anti-CD31 rabbit primary Ab (Abcam ab28364) and a 1:200 dilution of an AlexaFlor 594-conjugated anti-rabbit donkey secondary Ab (Jackson ImmunoResearch 711-585-152) with 0.02% NaN_3 in PBST for 7 days each with shaking to visualize vasculature. A 1:1000 dilution of Draq5 (Cell Signaling) nuclear stain was added to secondary Ab cocktail. Immunostains were replaced every one-two days with fresh cocktail, and tissues were washed for two days with a minimum of four exchanges in PBST with 0.02% NaN_3 between stains and after final stain. Samples were incubated in RIMS (prepared with Histodenz, Sigma-Aldrich, RI = 1.46) with gentle agitation for one day. Glass slides were prepared with 1 mm iSpacers (SunJin Lab Co.). Samples were placed inside the spacer, followed by slight overfill of fresh RIMS, and a coverslip.

Imaging. Z-stacks were acquired with a Zeiss LSM 710 confocal microscope using an Achroplan 20 / 0.5 NA water objective with ~40-50% overlap. Linear laser power z-correction was applied in Zen software (Zeiss) to ensure uniform signal intensity throughout the sample, as even cleared tissue will scatter at depth. For comparative analysis between samples, all laser and gain settings were set at the beginning of imaging and were unchanged. Image analysis was performed with Imaris (Bitplane).

B.5 References

1. Committee on care and use of laboratory animals (1996) *Guide for the care and use of laboratory animals* (Natl Inst Health, Bethesda), DHHS Publ No (NIH) 85-23.

2. Treweek JB, Chan KY, Flytzanis NC, Yang B, Deverman BE, et al. (2015) Whole-body tissue stabilization and selective extractions via tissue-hydrogel hybrids for high-resolution intact circuit mapping and phenotyping. *Nature Protocols* 10(11):1860–1896.